

#### **Absorbing Horizons**

#### A study on strongly absorbing luminescent thin films for luminescent solar concentrator applications

Derksen, M.

10.4233/uuid:afd45c56-e348-4ef0-aba8-2a02453e4543

**Publication date** 

2025

**Document Version** 

Final published version

Citation (APA)

Derksen, M. (2025). Absorbing Horizons: A study on strongly absorbing luminescent thin films for luminescent solar concentrator applications. [Dissertation (TU Delft), Delft University of Technology]. https://doi.org/10.4233/uuid:afd45c56-e348-4ef0-aba8-2a02453e4543

#### Important note

To cite this publication, please use the final published version (if applicable). Please check the document version above.

Copyright
Other than for strictly personal use, it is not permitted to download, forward or distribute the text or part of it, without the consent of the author(s) and/or copyright holder(s), unless the work is under an open content license such as Creative Commons.

Please contact us and provide details if you believe this document breaches copyrights. We will remove access to the work immediately and investigate your claim.

# ABSORBING HORIZONS

A study on strongly absorbing luminescent thin films for luminsecent solar concentrator applications

Max Derksen

### **Absorbing Horizons**

A study on strongly absorbing luminescent thin films for luminescent solar concentrator applications

#### **Absorbing Horizons**

# A study on strongly absorbing luminescent thin films for luminescent solar concentrator applications

#### Dissertation

For the purpose of obtaining the degree of doctor at Delft University of Technology, by the authority of the Rector Magnificus prof. dr. ir. T.H.J.J. van der Hagen, chair of the Board of Doctorates, to be defended publicly on Thursday 15th of May 2025 at 15:00 o'clock

by

#### Max DERKSEN

Master in Science in Physics with Astro-Physics University of Glasgow, Glasgow, Scotland, born in Den Helder, The Netherlands. This dissertation has been approved by the promotors.

#### Composition of the doctoral committee:

Rector Magnificus, chairperson

Dr. E. van der Kolk, Delft University of Technology, promotor Prof. dr. P. Dorenbos, Delft University of Technology, promotor

Independent members:

Prof. dr. E.H. Brück, Delft University of Technology Prof. dr. A.J. Houtepen, Delft University of Technology

Prof, dr. P.F. Smet, Ghent University Dr. J. Ueda, Kyoto University

Dr. G.B.F. Bosco, Fotoniq by, The Netherlands

Dr. E. Kelder, Delft University of Technology, reserve member





Keywords: Luminescent solar concentrators, reactive magnetron sputtering,

luminescent thin film charactization, lanthanide spectroscopy

Printed by: Ipskamp Printing

Cover Design: A photo of a CuGaS<sub>2</sub>:Yb<sup>3+</sup> thin film, partial topic of this thesis.

Designed by Bas Derksen

Copyright © 2025 by M. Derksen

ISBN 978-94-6473-800-1

An electronic version of this dissertation is available at http://repository.tudelft.nl/.

## **Contents**

Preface.		xi
Too Lor	ng; Didn't Read (TL;DR)	xiii
1 Intr	roduction	1
1.1	Agreements, Agreements	2
1.2	The Electricity Generating Window	3
1.3	LSC Efficiency	4
1.4	Fabrication of LSCs	6
1.5	Absorption in Thin Film LSCs	8
1.6	Thesis Goal and Outline	9
1.7	References	10
2 Fab	oricating and Analysing Luminescent Thin Films	11
2.1	(Reactive) Magnetron Sputtering	12
2.1.1	The Basics of Operation	12
2.1.2	Calibration Comes First	13
2.1.3	Thin Film Synthesis Work Flow	21
2.1.4	Troubleshooting	23
2.1.5	Cleaning Procedure	25
2.2	Gradient Composition Thin Film Characterization	26
2.2.1	Composition - EDX/EDS	28
2.2.2	The XY Set-Up	33
2.3	Closing Remarks	38
2.4	References	39
3 Sm <sup>2</sup>	<sup>2+</sup> in Glass	41
3.1	Introduction on Sm <sup>2+</sup> and Sm <sup>3+</sup> luminescence	42
3.2	Experimental Methods	46
3.3	Results and Discussion	47
3.4	Summary and Concluding Remarks	54

3.5	References	55
4 Cr	3+ and Nd3+ in the Al <sub>2</sub> O <sub>3</sub> -Y <sub>2</sub> O <sub>3</sub> System	57
4.1	Abstract	57
4.2	Introduction:	58
4.3	Experimental details	60
4.4	Results & Discussion	63
4.5	Conclusion	79
4.6	References	81
5 Cu	GaS <sub>2</sub> :Yb <sup>3+</sup>	83
5.1	Abstract	83
5.2	Introduction:	84
5.3	Experimental details	88
5.4	Results & Discussion	90
5.5	Conclusion	104
5.6	References	106
6 Su	mmary, Concluding Remarks and Recommendations	109
6.1	The XY Method	110
6.2	Findings on the Thin Films of this Thesis	111
6.3	Future Research Directions	117
6.4	Final Thoughts on the Electricity Generating Window	120
6.5	References	121
Summa	ry	123
Sameny	vatting	127
Acknov	vledgements	129
About t	he Author	135
'List' of	Publications	137

This thesis is dedicated to those brave souls who, upon being asked what they would like to do with their lives, shrugged, thought about it for a minute, and then, with a quiet but determined sigh, decided that a PhD would be as good a choice as any.

They didn't take this path because they were burning with passion for research, nor were they motivated by some grand vision of discovery. No, they chose it because it seemed like the thing to do when faced with a world full of decisions, all equally impossible to make.

They may never become the legendary professors or pioneers of tomorrow, but they'll make it through somehow, skirting the edge of academia, occasionally glancing at the door leading to their 'real life' without quite opening it. They may not know it, but they're like unnoticed gears in a machine—quietly turning away, and without them, science would come to a halt.

Here's to you, the Path-of-Least-Resistance PhD candidates: you're in the game now, whether you wanted to be or not.

#### **Preface**

The date is 19th of March 2025, and I have by now started a new job at the Dutch Aerospace Centre (Nederlandse Lucht- en Ruimtevaartcentrum – NLR). The first final draft of this thesis was handed to the doctoral committee sometime in November 2024. A mere 3 to 4 months have gone by and I find myself having forgotten many details of my PhD research. Luckily the feedback of committee members that I received this week forced me to think about what I have written down. Going through my thesis one last time is a bittersweet feeling. I am reminded of all the great moments I shared with my colleagues yet also the seemingly endless struggles to get experiments to work. What I am most pleased about is that I believe my thesis quite accurately describes my experience as a PhD student and reflects, in someway, my personality. The goal of any PhD student is to become an autonomous researcher, and I feel I can comfortably say that I have achieved this goal. I truly hope that this thesis can aid those who will continue research on luminescent solar concentrators, sputtering and the characterization of luminescent thin films.

"Why waste time say lot word when few word do trick" - Kevin Malone.

What: My research revolved around 'luminescent thin films':

- Luminescent: glow or emit light.
- Thin Film: a coating  $(1/1000^{th})$  of a millimetre thick) on top of a material.

Why: Add a luminescent thin film to a window and you can make a 'luminescent solar concentrator' (LSC). An LSC is a (luminescent) material that absorbs light (i.e. energy) from the sun (solar) after which the material lights up. The light that is emitted by the LSC gets trapped inside the LSC and is guided towards the edge which is how it acts as a 'concentrator'. Add some small solar panels along the edges of an LSC and you have yourself an 'electricity generating window'. Buildings with electricity generating windows? Yes please. Also, there is the 'European Green Deal', which aims to have net zero greenhouse gas emissions by 2050. Buildings are responsible for some 35% of all emissions in Europe.

How: Put some luminescent ions like 'rare earth metals' in a host material. The electrons in the ions get excited (absorb light) and they relax again (emit light). Thin films are made using an industry-friendly technique called (reactive magnetron) sputtering.

**Challenge:** For an electricity generating window to be efficient, i.e. that it produces a good amount of power, requires that you absorb an adequate amount, roughly 50 % of UV and visible part of the solar spectrum. The use of thin films creates a challenge as you only have very limited thickness to absorb the sunlight. So, we need 'strongly absorbing luminescent thin films' (see subtitle of this thesis). To make it even more challenging, the rare earth metals aren't known for their strong absorption properties.

**Approach:** Think of novel materials that could meet the absorption requirement and could show rare-earth luminescence. Make said films and study their **composition**, **crystal structure** and luminescence behaviour such as **excitation/emission** properties, **radiative lifetime** and **quantum efficiency**. Use a unique methodology to study a wide range of materials within a single film called the **'XY Method'**. Comment, based on the results, on their candidacy for LSC applications.

**Result:** Three different types of thin films were made based on three different rare earths: samarium, neodymium and ytterbium. Either the film does not absorb enough, but the luminescence is quite efficient, or the film absorbs a lot but the luminescence is very inefficient. The most important result? Having a relatively good time during all this!

#### 1 Introduction

The introduction to a piece of scientific work often dives headfirst in the deep end with latest advances found in a certain field. Should the general public read an introduction to a scientific paper regarding luminescent solar concentrators (LSCs) then they shall likely be lost after the first sentence. On the other hand, someone who is familiar with the field of LSCs can often skip the introduction, as they are, more often than not, extremely similar to other scientific introductions about LSCs. Of course there are exceptions when reading an introduction is key to understanding some concepts or motivations behind the research presented in the paper. Still the introduction is, after the methodology, the least read section of a scientific article. In an attempt to prevent losing the likely majority of my readers (the general audience to whom I gift this thesis) I have chosen to dedicate my introduction to a general, non-academic, reader. Though I am considerate of the general reader, it is difficult to steer clear of the use of jargon. What's more is that some scientific literacy is assumed along with a firm grasp on the English language.

I start with a quick overview of some agreements made by the European Union to combat climate change. Part of the agreements aims to reduce the energy consumption of buildings. One innovative technology that could aid in achieving this aim is an electricity generating window. The operating principles behind an electricity generating window is then presented. I continue with a discussion on the challenges in realizing this window. The subject of this thesis is addressing one of these challenges: light absorption. Finally, an outline of this thesis is given.

This introduction serves as an invitation to friends and family to put on their dusty lab coats and learn about *luminescent solar concentrators*. Of course, you could also just stick to the TL;DR, I wouldn't blame you.

#### 1.1 Agreements, Agreements, Agreements...

The first report of the impact of elevated greenhouse gas emissions on our planets temperature dates back to 1896 [1]. At that time the words climate change or global warming were not uttered in everyday households. Fast forward today and the words are repeated at nearly every political debate in any country. A number of agreements, such as the infamous 'Paris Agreement', have been made amongst countries to combat climate change [2]. The EU has fallen behind on reaching the goals set out in the Paris agreement and have solved this with another agreement: The European Green Deal [3]. The European Green Deal aims to be climate neutral by 2050. Part of the agreement is the 'Renovation Wave Initiative' which aims to renovate buildings in order to decrease the emissions from poorly insulated buildings [4]. The European Environment Agency estimates that buildings contribute roughly 35% of the energy-related European Union (EU) emissions and that buildings are the single largest energy consumer in Europe [5]. However the idea behind improving the energy performance of buildings is not by any means a new idea. In 2002 the 'Energy Performance of Buildings Directive' (EPBD) was introduced by the EU and revised in 2010. This form of legislation outlines new standards for buildings to be nearly zero-emission buildings (NZEBs). A new proposal had been submitted in 2021 to amend the goals set in the 2010 version. One of those amendments was to ensure that buildings can accommodate solar energy installations on buildings and move from NZEBs to zero-emission buildings (ZEBs) by 2030 [6]. A common concern in The Netherlands is the current capabilities to accommodate and store renewable electrical energy produced by commercial wind turbines and solar panels. The Net-Zero Industry Act (NZIA) was signed on the 16th of March 2023 to guarantee that Europe can manufacture and scale up the net-zero technology required to meet the European Green Deal [7]. All these agreements will ideally provide a path towards limiting the impact of climate change. Though all this legislation may not always seem to be very efficient, they have proven to work in the past. The Montreal Protocol of 1987 is a treaty that aimed to combat the depleting ozone layer [8]. The treaty is the first to be universally ratified by all countries in the world. Fears of a depleting ozone have dissipated due to the combined successful efforts conducted by each country.

To realise the goals of the agreements mentioned above, actions must be undertaken. One of these actions is developing innovative technology to reduce emissions. In the case of having ZEBs in 2030 there are several ideas that have come forward to reduce the emission of buildings and ways for buildings to generate their own energy. One of these ideas is called "building-integrated photovoltaics" (BIPV), where solar cells are installed as part of the building's architecture. For example, Tesla's Solar Roof are roof tiles that can be installed on commercial homes and act as solar panels. Another type of BIPV is an electricity generating window, which is the application that is kept in mind during my four years of research.

#### 1.2 The Electricity Generating Window

An electricity generating window can be made by combining solar panels with a luminescent solar concentrator (LSC). The former is well known, however, the same cannot be said of the latter. An LSC, as the name suggests, concentrates solar radiation through a luminescent process. The operating principles are relatively simple:

- (i) Solar radiation, or photons, enter a medium (glass, for example) doped with luminescent centres
- (ii) Said photons are absorbed and thereby activate or excite luminescent centres within the medium
- (iii) The excited luminescent centres relax and result in the emission of light (i.e. photons)
- (iv) The emitted light is trapped within the medium and is totally internally reflected towards the edge

Placing solar cells at the edge of the medium (or window in our case) can then harvest the concentrated emitted light from the luminescent centres. In **Fig. 1.1** a schematic of such an electricity window is shown whereby the element Tm<sup>2+</sup> is the luminescent centre, or ion.

The conceptualization of an LSC dates back to 1976 [9]. However, there is yet to be a commercialized electricity generating window introduced to the market. The reasons for this is quite simple; there hasn't been a luminescent material efficient and cost effective enough at large scale for mass production. As of 2019, the most efficient, large-scale (> 0.5 m²) LSC has a power conversion efficiency of a measly 1.75 % [10, 11]. Assuming 1000 W/m² of solar radiation incident on Earth and this particular LSC scaled to 1x1 m² we can get about 18 W from this electricity generating window, enough to power a couple of LEDs. Efficient loss mechanisms present in LSCs such as self-absorption, scattering losses and non-radiative recombination are detrimental to the performance of an LSC. A deeper dive into the efficiency of an LSC is discussed in the next sub section. What's more is that this most efficient LSC of 1.75 % is based on a luminescent dye named Lumogen F Red-305, which as the name suggest, has a red colour. Rose tinted glasses can be nice for a sunny day on a terrace, but for office building windows it is simply unsuitable.

I have already mentioned two flavours of luminescent centres typically used to make an LSC. Rare-earth metals (such as Tm<sup>2+</sup>) and organic dyes (such as Lumogen F Red 305). To make that list complete there is also the increasingly popular (at least in the luminescence community), quantum dot. A quantum dot can be simply thought of as a tiny cluster (order of 10-100 nm) of semiconductor material. It is not the first time that these three luminescent centres battle it out for a certain application. TV's, and their emitting light, also have used rare-earths, quantum dots and organic dye. The old-school cathode-ray tube TV used the rare earth ion Eu<sup>3+</sup> to create a red colour. Whereas current

organic LEDs (OLED) and quantum dot LEDs (QLED) based TV's use organic dyes and quantum dots to elevate colours beyond the capabilities of standard LEDs. Similar to the TV industry, current LSC research is mainly focused on organic dyes and quantum dots. However, rare-earth's ought not to be crossed out just yet. Their high achievable quantum yields, narrow and predictive line emission, tune-able absorption properties and photo stability make rare-earth's valid contenders in the LSC race. This thesis therefore concerns itself with the less popular rare-earth based LSC.

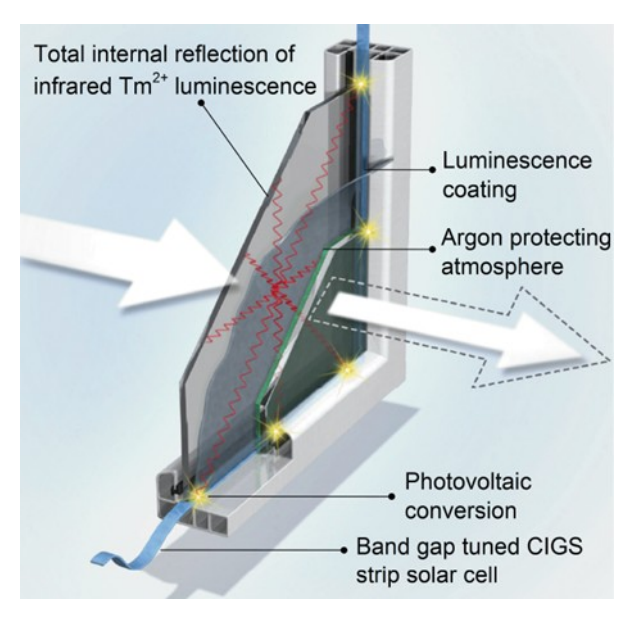


**Fig. 1.1** Schematic of the electricity generating window. The large white arrow represents incident sunlight, of which most is transmitted. The absorbed light activates Tm<sup>2+</sup> which subsequently emits infrared light that is collected at the edge of the window.

#### 1.3 LSC Efficiency

As mentioned above, the most efficient electricity generating window can currently produce about 18 W per square meter [11]. The efficiency of such a window is typically called the power conversion efficiency, i.e. how much power can we convert from the Sun into useful electrical energy. This number can be split up into the efficiency of the LSC and the solar cell at the edge. To describe the efficiency of an LSC the so-called optical efficiency is often used, described simply as:

$$\eta_{opt} = \frac{\text{\# photons emitted at the edge}}{\text{\# photons incident on the face}}$$
(1.1)

The denominator (# photons incident on the face) is straight forward, it's the photons coming from the sun incident on our LSC. The numerator (#photons emitted at the edge) is vastly more complex. It depends on the behaviour of our luminescent centres (how many photons do they absorb and emit) and on the behaviour of the glass (how many photons get transported, or wave-guided, to the edge). Starting with the luminescence of the centres, we can define the external quantum efficiency (EQE) as:

$$EQE = \frac{\#emitted\ photons}{\#incident\ photons} \tag{1.2}$$

We can split up the emitted photons and incident photons by adding a crucial step, absorption:

$$EQE = \frac{\#absorbed\ photons}{\#incident\ photons} \frac{\#emitted\ photons}{\#absorbed\ photons}$$
(1.3)

What we are then left with what are called the absorption efficiency ( $\eta_{abs}$ ) and the internal quantum efficiency ( $\eta_{IOE}$ ), or:

$$EQE = \eta_{abs}\eta_{IOE} \tag{1.4}$$

Note that in literature the term internal quantum efficiency and quantum yield are used interchangeably. This covered the efficiency of the luminescence, but we also need to look at the 'concentration efficiency' of the window itself. Light that is emitted inside a glass can be transported to the edge by a process dubbed total internal reflection. It is similar to how an optical fibre transmits a signal or how a diamond traps light and results in a sparkling effect. One condition for the photons to be trapped is that the incoming angle of the photon on the glass-air interface is shallow enough (this is called the 'critical angle'). This leads us to our first concentration efficiency which is the *trapping efficiency*,  $\eta_{trap}$ . The trapping efficiency tells us how much of our emitted photons are transported to the edge. But, as the emitted light is travelling through our glass it might get absorbed by the luminescent centres themselves. To take this effect into account we have a 'selfabsorption' efficiency,  $\eta_{sa}$ . Finally, there is the chance that the emitted light can be absorbed by the glass itself, for example iron impurities in glass give it a green hue along the edge. The emitted light can also scatter off other atoms in the glass and result in the photon still escaping out of the glass. These effects are incorporated in the wave-guiding efficiency,  $\eta_{wg}$ . Last but not least, we should consider the fact that some light on our window can be reflected away, thereby never entering the LSC. Glass used for windows typically reflect (R) about 4% of the incoming light on each glass-air interface which is why you can sometimes catch a glimpse of your reflection in a seemingly transparent window. If we take this all together we can give a more detailed definition to the optical efficiency of an LSC.

$$\eta_{opt} = (1 - R)\eta_{abs}\eta_{IQY}\eta_{trap}\eta_{SA}\eta_{WG}$$
 (1.5)

This new definition of the optical efficiency is just dipping our toes in the water of LSC characterization. It does allow us to focus on certain parameters to increase our LSC efficiency.

Combining the optical efficiency of an LSC along with the efficiency of a solar cell to get the total efficiency of the electricity generating window is not trivial. For example the solar cell will be receiving the emitted luminescence from the LSC rather than the sun which can alter the output of the solar cell. The in coupling of the luminescence to the solar cell at the edge can lead to significant losses. At the same time, it has been shown that concentrating light onto a solar cell, or increasing the intensity of light, improves the efficiency of the solar cell [12]. Even though there are a lot of extra factors that creep up in order to determine the final efficiency of our window, we can still crudely estimate an upper limit. We simply assume that the LSC behaves optically the same as a typical Si based solar cell. Our LSC absorbs the same as an Si solar cell, but rather than generate a current (electrons/second) it produces luminescence with an equivalent power (photons/second). We assume that the concentration efficiency is lossless, i.e.  $\eta_{trap} = \eta_{SA} = \eta_{WG} = 1$ . However, a key property of a window is that you can look through a window, whereas a solar panel is completely opaque. Thus we should typically absorb half of what a regular solar cell absorbs so that we can still look through it. The window will be tinted, not unlike the windows found in cars or office buildings. With this we can simply cut the efficiency of a solar cell (using the Shockley-Queisser limit of 32%) in half and use that as our upper limit for our window: 160 W/m<sup>2</sup>. For those interested in a more in depth consideration of the efficiency of an LSC I would recommend reading the introductory chapter of the thesis of my predecessor, Evert Merkx [13].

#### 1.4 Fabrication of LSCs

After finding the perfect LSC material, the next step would be to fabricate the material on a large scale. This is where certain synthesis techniques can make or break the mass adoption of this technology. Conventional LSCs have the luminescent center incorporated directly in the glass or polymer matrix, which often has a thickness of several millimeters. The most common technique for making an LSC is a four-step process:

- (i) Mixing the luminescent material with some polymer or monomer (typically PMMA, also known more commonly as Plexiglas)
- (ii) Casting or molding the mixture in the right size
- (iii) Polymerizing (or hardening) is often done through some chemical reaction with heat and/or UV radiation.
- (iv) Cutting and polishing

Another technique is to create an LSC is through lamination, where a material is manufactured in multiple layers. Alternatively, there is the thin film based LSC, where only a thin luminescent coating is applied to the glass. There are a number of benefits of a thin film based LSC. For example, less (expensive) material is used in a thin film than in the conventional LSC making it significantly more cost-effective. Selfabsorption losses are reduced as the emitted light travels mainly through the glass rather than the luminescent coating. Finally, applying a thin film is nothing new for the glass industry, thus adding another thin film layer in the window production pipeline has a minimum effect on manufacturing and can therefore be easily adopted by industry. There are various methods to make a thin film LSC such as sol-gel, melt processing, chemical vapor deposition and more. Certain synthesis techniques are more up-scalable than others. For instance, applying a sol-gel solution via spin-coating is unfeasible on a large scale. Whereas other methods such as dip or blade coating are suitable for large scale. Reactive magnetron sputtering is another type of synthesis technique used by the glass industry to coat windows with anti-reflective or anti-corrosive thin films. In fact, as magnetron sputtering is adopted by the glass industry it serves as the only technique that allows rapid implementation of LSCs and can thereby have a real impact reducing the emissions of buildings. In the LSC community however, reactive magnetron sputtering is not often employed. For the reasons listed above, reactive magnetron sputtering is used to fabricate the thin film based LSCs in this thesis.

To summarize thus far, the electricity generating window operates with the assistance of a luminescent solar concentrator or LSC. There are different flavors of LSC: quantum dots, organic dyes and rare-earths. The efficiency of an LSC is determined by several factors such as the absorption and internal quantum efficiencies. Thin film based LSCs offer a cost-effective path to rapid adoption by the glass industry if a good LSC contender is found. Reactive magnetron sputtering is a fabrication technique that is upscalable and already an established industry practice. From a practical perspective, industry sputtering deposition times limit thin film thickness to under a micron. The rest of this thesis focuses on one core issue that haunts the rare-earth thin film based LSC: absorption.

#### 1.5 Absorption in Thin Film LSCs

To convert solar radiation into electricity requires the absorption of photons. The more photons we absorb the more electricity we can produce. This is why solar panels are black. Window applications require that we do not absorb all the photons, as we would still like to be able to see through them. Absorbing only part of the visible spectrum can result in unwanted colorization of the window. Meanwhile avoiding any absorption of the visible spectrum limits the maximum efficiency immensely as a significant part of the solar energy arriving at Earth, some 43%, is in the form of visible photons. Thus in terms of absorption it would be ideal to absorb all of the UV part and roughly 50% of the visible part of the solar spectrum. The resulting window would be tinted grey, but that is still acceptable for office and residential environments. Now add the fact that we are using weak and narrow absorbing trivalent rare earth in thin films of just 1 micron thick and we run into the issue of poor absorption.

#### Lanthanides

Rare-earths, or lanthanides, with an electron configuration of  $[Xe]6s^25d^14f^n$  (n = 1, 2...14 = Ce, Pr...Yb), can all have an oxidation state of 3+ when put in a compound, where they lose the 6s and 5d electrons. 2+ and 4+ oxidation states are stable for a select number of lanthanides. Trivalent lanthanides are well known for their shielded intra-shell 4f-4f electronic transitions that result in narrow line emission. The narrow emission can be useful to tune a solar cell to spectrally match the highest efficiency of the solar cell with the emission. However, the nature of the 4f-4f transition is forbidden according to parity selection rules, or Laporte's rules. These 4f-4f transitions therefore have weak and narrow absorption which is the opposite of what we need in a thin film LSC that needs to absorb 50% across the entire visible spectrum within a thickness of less than a micron. The possible solutions to this are the main topic of this thesis. To improve the absorption properties of trivalent lanthanides the following three options are explored: Reduce the trivalent lanthanide to a divalent lanthanide where 4f-5d, rather than 4f-4f, transitions result in strong and broad absorption. Use a sensitizer ion which acts as the 'absorber' that transfers the absorbed energy to the trivalent lanthanide. Use absorption properties of the host material that can transfer the energy to the trivalent lanthanide. These three options form the basis for Chapters 3, Chapter 4 and Chapter 5 and are discussed in more detail there.

#### 1.6 Thesis Goal and Outline

The overarching goal of this research is quite obvious: make the electricity generating window closer to reality. However that's a tall order for a single PhD student to single handily undertake. Like any PhD project, the key is to focus onto a smaller specific set of problems, or concepts, and try to understand them and to finally offer a new perspective to concepts to the scientific body. In the case of this research the focus was put onto fabricating LSCs with a high absorption efficiency while using industry compatible techniques. The emphasis on using industry compatible techniques is an important one. Once a contender for an LSC is found, the next step would be to produce it on a large scale. If we use certain synthesis methods that are not feasible on large scale then it might not even be possible to fabricate the LSC at all. By complying with industry practices in the lab we can ensure a faster transition to mass adoption. For this reason, the materials for LSC considerations studied in this thesis are based on thin films made by (reactive) magnetron sputtering. The goal of this thesis can now be summarized as follows:

# Fabricate strong and broad absorbing thin films made via (reactive) magnetron sputtering and study their optical and luminescent properties for LSC considerations.

The outline of the thesis is as follows. **Chapter 2** considers an important part of the goal of this thesis, which is the actual fabrication of the thin films along with the studying of their optical and luminescent properties. A quite unique approach to conducting this research, dubbed the 'gradient XY method' is presented. Chapter 2 can be seen as somewhat of a practical guide for those who are to continue this type of research. The following three chapters, 3, 4 and 5 consider the three options presented earlier to improve trivalent lanthanide absorption. In **Chapter 3** an attempt is made to increase divalent samarium content in aluminium silicate thin films via co-doping. **Chapter 4** explores yttrium-aluminate thin films with a high sensitizer ion content, trivalent chromium, to excite trivalent neodymium. In **Chapter 5** the last option is explored where copper gallium sulphide thin films, with their narrow band-gap, are studied to see if they can efficiently sensitize trivalent ytterbium. Lastly, in **Chapter 6**, the three types of thin films discussed in Chapters 3, 4 and 5 are summarized and a side-by-side comparison is made between the thin films. Final thoughts are given on future general LSC research directions and for each material discussed in thesis.

#### 1.7 References

- [1] S. Arrhenius, "XXXI. On the influence of carbonic acid in the air upon the temperature of the ground," *The London, Edinburgh, and Dublin Philosophical Magazine and Journal of Science,* vol. 41, no. 251, pp. 237-276, 1896/04/01 1896, doi: 10.1080/14786449608620846.
- [2] UNFCCC, "The Paris Agreement," in Paris Climate Change Conference, Paris, 2015.
- [3] C. Fetting, "The European Green Deal," ESDN Office, Vienna, 2020.
- [4] (2020). Renovation Wave. [Online] Available: <a href="https://energy.ec.europa.eu/topics/energy-efficiency/energy-efficient-buildings/renovation-wave-en">https://energy.ec.europa.eu/topics/energy-efficiency/energy-efficient-buildings/renovation-wave-en</a>
- [5] E. E. Agency. "Greenhouse gas emissions from energy use in buildings in Europe." https://www.eea.europa.eu/en/analysis/indicators/greenhouse-gas-emissions-from-energy (accessed 2/11/2023.
- [6] (2021). 52021PC0802, Proposal for a DIRECTIVE OF THE EUROPEAN PARLIAMENT AND OF THE COUNCIL on the energy performance of buildings (recast). [Online] Available: https://eur-lex.europa.eu/legal-content/EN/ALL/?uri=celex:52021PC0802
- [7] (2023). COM(2023) 161, SWD(2023) 68, Net Zero Industry Act. [Online] Available: <a href="https://single-market-economy.ec.europa.eu/publications/net-zero-industry-act\_en">https://single-market-economy.ec.europa.eu/publications/net-zero-industry-act\_en</a>
- [8] M. Protocol, "Montreal Protocol on substances that deplete the ozone layer," Montreal, 1987.
- [9] W. H. Weber and J. Lambe, "Luminescent greenhouse collector for solar radiation," *Appl. Opt.*, vol. 15, no. 10, pp. 2299-2300, 1976/10/01 1976, doi: 10.1364/AO.15.002299.
- [10] J. Zhang et al., "Optimization of large-size glass laminated luminescent solar concentrators," Solar Energy, vol. 117, pp. 260-267, 2015.
- [11] M. Rafiee, S. Chandra, H. Ahmed, and S. J. McCormack, "An overview of various configurations of Luminescent Solar Concentrators for photovoltaic applications," *Optical Materials*, vol. 91, pp. 212-227, 2019, doi: 10.1016/j.optmat.2019.01.007.
- [12] J. Day, S. Senthilarasu, and T. K. Mallick, "Improving spectral modification for applications in solar cells: A review," *Renewable Energy*, vol. 132, pp. 186-205, 2019/03/01/2019, doi: https://doi.org/10.1016/j.renene.2018.07.101.
- [13] E. P. J. Merkx, "Luminous Glass: A Study on the Optics Governing Luminescent Solar Concentrators and Optimization of Luminescent Materials through Combinatorial Gradient Sputter Deposition," TU Delft, 2020.

### 2 Fabricating and Analysing Luminescent Thin Films

As the introduction was dedicated to a specific group (the general audience) so is this chapter. This chapter is dedicated to those that will follow my path of research on luminescent thin films, particularly within the luminescent materials group at TU Delft. Science ought to be reproducible, not only in the observed behaviour of nature, but also in the execution of the experiments conducted by the observer. To accomplish reproducibility, in particular with the samples made by reactive magnetron sputtering, requires a meticulous record of conditions and input parameters. In this chapter I aim to thoroughly describe the systematic research method, dubbed the gradient sputtering and xy-scanning methodology, which is used throughout this thesis. I hope to prevent wasted time by sharing some troubleshooting tips and tricks on how to sputter and characterize luminescent thin films.

#### 2.1 (Reactive) Magnetron Sputtering

As mentioned, the synthesis or fabrication method of choice to make the thin films presented in this thesis is (reactive) magnetron sputtering. Sputtering is a type of physical vapour deposition (PVD). I will not go into detail behind the physics of sputtering, but rather give a brief explanation on how it works and then dive deeper into the practicalities when making thin films. For a in depth explanation on the working principles, theory and modelling of sputtering there is a plethora of literature in the form of books available [1-5].

#### 2.1.1 The Basics of Operation

The sputtering process is relatively simple. A chamber is evacuated using a pump to pressures in the order of micro pascal's or torr (1 Pascal = 0.008 Torr = 0.01 mbar). Argon, known as the working gas, is introduced to the chamber and ionized by applying a voltage using electrodes. The cathode is situated underneath a target material that is going to be sputtered. Positive argon ions are then accelerated towards the cathode. The impact of the argon ions causes the target material to eject atoms which then travel in all directions. To improve the plasma stability it is common to have a magnetic field that traps electrons near the target surface which in turn results in a more localized plasma. This puts the magnetron in magnetron sputtering. The sputtered atoms are deposited on all the surfaces inside the chamber. A substrate, on which a thin film is grown, is often placed directly across from the target material.

All the samples presented in this thesis are made using a commercial AJA Orion 5 sputter coater. It allows to sputter four targets material simultaneously using either a pulsed direct current (DC) or a radio frequency (RF) power supply. The choice of power supply is based on the type of target material. If one is attempting to sputter an insulating material like aluminium oxide (Al<sub>2</sub>O<sub>3</sub>) it will be impossible to do so with a DC power supply. Remember that the cathode is situated underneath the target. If there is an insulating material on top of the cathode than the potential on the surface of the target material is dropped and positive ions can build up on the surface. The build-up of positive charge halts acceleration of other Ar ions towards the target/cathode and the process comes to a halt. In order to sputter insulating targets the RF power supply is used which provides an alternating electric field in order to prevent the build-up of charge on the target. The use of a RF power supply however comes at the cost of a lower sputter rate, as you are effectively only sputtering half the time.

The last term that needs explaining to cover the basics is 'reactive'. All this simply means introducing not only a working gas like argon, but a reactive gas too. This is most often oxygen or nitrogen. The reactive gas reacts with the target material to form a thin

compound layer which is then sputtered off by the working gas (argon), allowing us to sputter oxides and nitrides with a metallic target.

With this we have covered the absolute basics of sputtering. In the next sub-section I will cover some initial calibrations of sputter targets that give a feel for how to sputter.

#### 2.1.2 Calibration Comes First

The numerous parameters that can be tweaked during a reactive magnetron sputtering process is a blessing and a curse. It gives the sputter 'artist' freedom to create a large variety of thin films yet at the same time it can be difficult to fabricate one specific type of film. Unfortunately it is unfeasible to address the impact of each and every parameter on the sputtering process. Therefor I have chosen to focus on two input parameters that are crucial to have a feel for when doing reactive magnetron sputtering: the applied power (W) on the target material and the reactive gas flow (sccm - 'standard (atmospheric pressure) cubic centimetre per minute'). In order to have a feel for these two input parameters we can monitor two output parameters, the deposition rate measured by a quartz crystal monitor (QCM) and the plasma discharge voltage between the target material and the sputter chamber. The other input parameters are mentioned in less detail in the troubleshooting and glossary section.

#### **Power**

A universal experience for all sputter artists is opening the sputter chamber and finding a broken target. The most common reason for breaking a target is due to a too high power density on the target. The ion bombardment of Ar on the target causes the surface of the target to heat up and introduces thermal stress within the target. With insufficient water cooling and poor thermal conductivity the target material can reach temperatures well above 1500 °C which will melt numerous metals [6]. The targets used in this research were circular planar targets with a diameter of 2 inches and thickness between 1/8 and 1/4 inch. The surface area of a 2 inch diameter circle is about 20 cm<sup>2</sup>. Kurt J. Lesker, a provider of vacuum related products and systems, provides a table with appropriate power densities (W/cm<sup>2</sup>) for various types of materials which is summarized in **Table 2.1**. I would generally suggest to not go over the powers listed in **Table 2.1**. However should one wish to do so, there is a method to find the maximum power described by Kurt J. Lesker in their now archived newsletter 'Lesker Tech', volume 7 issue 1.

Table 2.1: Appropriate power levels for variations	ious sputter target materials given by Kurt J.
Lesi	ker.

Material	Power Density	2" Target Power
Highly Conductive (e.g. Al, Cu)	$15  \mathrm{W/cm^2}$	305 W
Moderately conductive (e.g. Ti)	9 W/cm <sup>2</sup>	180 W
Conductive Oxide (e.g. ITO, AZO)	$3  \mathrm{W/cm^2}$	60 W
Ceramic Insulator (e.g. HfO <sub>2</sub> )	3 W/cm <sup>2</sup>	60 W
Low Melting Metal (e.g. In, Sn)	2 W/cm <sup>2</sup>	40 W

The deposition rate of your sputtered atoms can be measured by a quartz crystal monitor (QCM). There is generally a linear relationship between the applied power and deposition rate. Double the power, double the deposition rate. When one is doing combinatorial sputtering, i.e. sputtering multiple targets at once, it is important to first establish the individual deposition rates of each element in order to obtain a desired stoichiometry. It is also important to remember that a 1 nm thick film of say Al<sub>2</sub>O<sub>3</sub> has a different number of atoms than a 1 nm thick film of say Cr<sub>2</sub>O<sub>3</sub>. To accommodate for this the molar volume of each element should be taken into consideration. For example, if we want make a Al<sub>1.8</sub>O<sub>3</sub>:Cr<sub>0.2</sub> thin film by sputtering from a Al<sub>2</sub>O<sub>3</sub> and Cr<sub>2</sub>O<sub>3</sub> target, then what should our deposition rate of Cr<sub>2</sub>O<sub>3</sub> be compared to Al<sub>2</sub>O<sub>3</sub> to achieve the right Cr doping concentration of 10%? My approach is the following. First establish a deposition rate of the host material (Al<sub>2</sub>O<sub>3</sub>) at a certain power, ideally as high as possible. Then if we want to have 90% Al<sub>2</sub>O<sub>3</sub> and 10% Cr<sub>2</sub>O<sub>3</sub> we reduce the power until the deposition rate is 90% of the initial Al<sub>2</sub>O<sub>3</sub> deposition rate. The Cr<sub>2</sub>O<sub>3</sub> deposition rate should be then 10% of the initial Al<sub>2</sub>O<sub>3</sub> deposition rate, but also account for the difference in molar volume. The molar volume of Al<sub>2</sub>O<sub>3</sub> is 25.72 cm<sup>3</sup>/mol and for  $Cr_2O_3$  it is 29.12 cm<sup>3</sup>/mol. 25.72/29.12 = 0.88, giving us that the  $Cr_2O_3$  deposition rate should be equal to the initial  $Al_2O_3$  deposition rate \* 0.1 \* 0.88.

A typical QCM will have difficulty to determine a deposition rate of less than 0.01 Å/s. Should your deposition rate be lower than 0.01 Å/s then it is easiest to deposit for a known amount of time until a thickness is measured by the QCM and simply divide the final thickness by the time. It should be noted that achieving exact stoichiometry's using sputtering is challenging and that other techniques such as chemical vapour deposition or solid state synthesis can be more appropriate. However it is nonetheless beneficial to think of the relative deposition rates of each individual target beforehand. In the end the true composition of your material will be checked via energy dispersive x-ray spectroscopy (EDX), but more on that later.

#### Reactive Gas Flow

Introducing a reactive gas such as oxygen allows us to sputter oxides with a metallic target. Understanding the condition of the target is crucial for getting a feel for how to reactively sputter. If we want to sputter  $Al_2O_3$  from a metallic Al target in a mixed argonoxygen atmosphere then the question is: how much oxygen should we add to the chamber? If we don't add enough we will end up with an oxygen-deficient, substoichiometric  $Al_2O_3$  film. However adding too much oxygen can lead to a 'poisoned' target and can have adverse effects on the plasma stability shown by arcing which often ultimately leads to the dreadful message from the software: "Process aborted". What's more is that the deposition rate of a poisoned target is often very low requiring a long deposition time. Luckily with a simple calibration we can get a feel for the targets condition by monitoring the plasma discharge voltage as a function of reactive gas flow.

The plasma discharge voltage is influenced by the so-called ion induced secondary electron emission (ISEE) of the target material [7]. Going from a pure metallic target, such as Al, to an Al target with a thin layer of oxygen will alter the ISEE. If we are sputtering with a power supply that is keeping a constant plasma discharge power and the number of electron's released by the target increases (or in other words the plasma discharge current increases) then in order to compensate the power supply will alter its output so that the plasma discharge voltage will drop. (Ohm's Law: P = IV).

To get a feel for how a target behaves in a mixed argon-oxygen atmosphere we can conduct a simple, yet effective calibration often called the *hysteresis experiment*. The execution of such an experiment is quite straightforward. Measure the discharge voltage of your target for some time while stepwise increasing the O:Ar ratio. Once the final O:Ar ratio is reached go back in the same steps. The results for a typical hysteresis experiment done for Al at a power of 100 W is shown in Fig. 2.1. The argon + oxygen flow is a constant 15 sccm. We can see that increasing the O<sub>2</sub> flow from 0 up until 2 sccm had little impact on the discharge voltage, indicating that the ISEE has not changed and that we are sputtering in so-called metallic mode. 2 sccm is a critical point where there is a sharp drop in the voltage. Going beyond 2 sccm we are sputtering in so-called 'poisoned mode'. The critical point at 2 sccm in Fig. 2.1 is the result of a too low getter capacity by the metallic target (Al in our case). Once the sputter rate of Al is lower than the rate at which Al is being oxidized then the target will quickly get fully oxidized, or in sputter terminology, poisoned. The drop in voltage of the target is simultaneous with an increase in the partial pressure of oxygen in the chamber [8]. Quite often the plasma will change color too at this point. For example, when sputtering metallic chromium the plasma is typically blue, whereas when chromium is poisoned the plasma color is purple (due to argon) [9]. Note that when we go back from 5 sccm to 0 we get back to the metallic mode around 1 sccm. This hysteresis behavior shows that the starting condition of the target is important to keep in mind. For this reason I

like to have a standard pre-sputter step before depositing any thin film to ensure that the target is not oxidized.

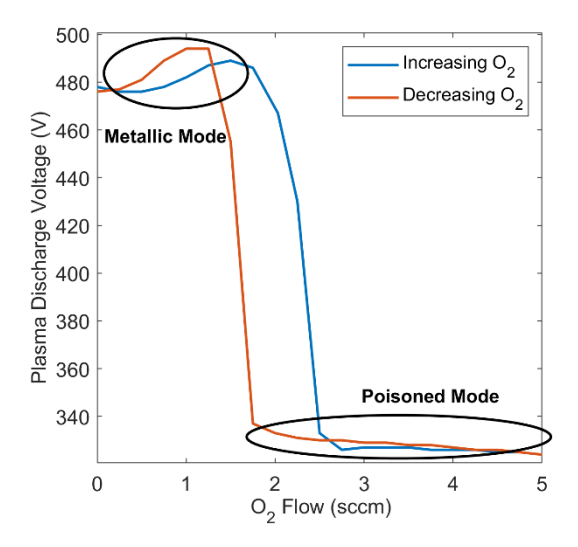


**Fig. 2.1.** Typical hysteresis curve of Al at sputtered at 100 W. Two regions are identified, the 'metallic' and 'poisoned' mode which can be identified by the plasma discharge voltage.

Generally, it is ideal to reactively sputter our oxides or nitrides right at the first critical point, before entering the transition region. This allows us to have a high deposition rate whilst depositing a stoichiometric oxide/nitride thin film.

The power and reactive gas flow along with the deposition rate and plasma discharge voltage are the 4 key parameters to understand from a material when starting to synthesize a series of films. However there are more parameters that can be tweaked which I will briefly discuss.

#### The Rest of The Sputter Parameters

There are a few other sputter parameters that are accessible which we can play with in order to influence our final film.

#### Substrate Bias

During deposition we can activate a cathode under our substrate and accelerate Ar ions towards it. This can result in more dense and crystalline thin films with fewer defects and improved adhesion [10]. **Fig. 2.2** shows XRD measurements of 3 samples that were made by sputtering Cu in an oxygen/argon atmosphere. An overall increase in peak

intensity is observed at higher substrate bias power, however it should be noted that there can also be a shift in crystalline phase as indicated by the dotted lines.

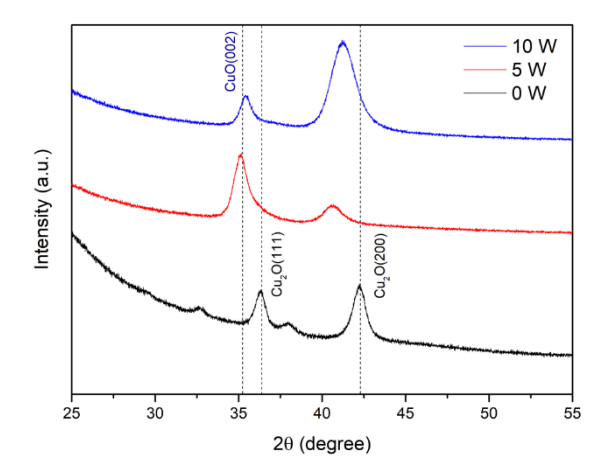


Fig. 2.2. XRD measurements showing the influence of applying a substrate bias on the crystallography of copper oxide films made by sputtering copper in an Ar/O environment.

The deposition rate can also be influenced, often reduced, unequally for different elements. Sputtering the substrate can also be used as a form of cleaning the substrate prior to deposition. Note that in the AJA Orion 5 system the power on the substrate should never exceed 50 W.

#### **Working Gas Pressure**

The argon pressure is typically 3 mTorr whilst depositing a thin film. This pressure is empirically found to be a good balance between having enough argon to maintain a steady plasma yet not too much argon which can result in thermalized sputtered atoms (i.e. reduced deposition rates) due to scatter events with the argon ions. However it can be of interest to increase this pressure to improve plasma stability, especially when sputtering at low powers. The reduced deposition rate will effect lighter atoms more than heavier atoms, which can also be used as a tool to control the composition of the film.

#### Working/Throw Distance

The distance between the target and substrate is called the working or throw distance. Decreasing this distance will enhance the deposition rate, but can decrease the

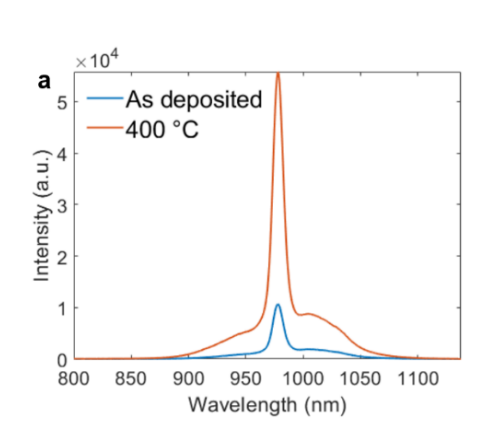
uniformity of your film. A smaller working distance will also result in your sputtered atoms having a higher energy when arriving at the substrate which can influence the adhesion, density and crystallinity. When sputtering from a single target such as CuGaSe<sub>2</sub>, it is found that the throw distance influences stoichiometry of the thin film [11]. Towards the end of this section **Table 2.3** is presented where the obtained CuGaS<sub>2</sub> stoichiometry of a sputtered thin film from a single target as function of working/throw distance is investigated.

#### Substrate Temperature

During deposition it is possible to heat the substrate up to 850 degrees Celsius with the AJA Orion 5 sputter coater. Generally, substrate heating results in improved crystallinity, uniformity and less defects. The increased energy of sputtered atoms upon arriving at the substrate allows the atoms to find their preferred sites more easily. In some cases, like the Cr<sub>2</sub>O<sub>3</sub> samples discussed in **Chapter 4**, it is crucial to deposit at elevated temperatures to get the right crystallinity. For Cr<sub>2</sub>O<sub>3</sub>, depositing at room temperature resulted in transparent and amorphous thin films, while at temperature of 400 °C and higher the samples showed crystalline structure and had a green colour related to characteristic Cr3+ absorption. In the work by my master student, Sem, it is shown that for sputtered CuGaS<sub>2</sub>:Yb<sup>3+</sup> thin films the substrate temperature greatly impacts the Yb3+ emission intensity [12]. Two films were fabricated where one was deposited with a substrate at room temperature (CGS10) while the other had a substrate temperature of 400 °C (CGS14), the remainder of the sputter parameters were kept the same. In Fig. 2.3b we can see in the XRD diffractogram that CGS10 showed no signs of crystallinity, whereas for CGS14 there are, albeit low intensity, peaks visible related to the chalcopyrite structure of CuGaS<sub>2</sub> (ICCD:04-005-2909). Note that presented CGS17 sample is also a CuGaS2 thin film deposited at 400 °C but with double the deposition time, leading to a thicker film and more intense peak intensities. Table 2.2 summarizes the relevant sputter parameters of samples CGS10, CGS14 and CGS17. In Fig. 2.3a the Yb<sup>3+</sup> emission intensity is shown for CGS10 (labelled 'As deposited') and CGS14 (labelled 400 °C). The Yb3+ emission intensity is increased by over a factor of 5, which has been attributed to the improved crystallinity due to the elevated temperature of the substrate during deposition.

**Table 2.2.** Substrate temperature and deposition time deposition parameters during sputtering of samples CGS10, CGS14 and CGS17

Sample code	Substrate temperature (°C)	Deposition time (s)
CGS10	20	5.000
CGS14	400	5.000
CGS17	400	10.000



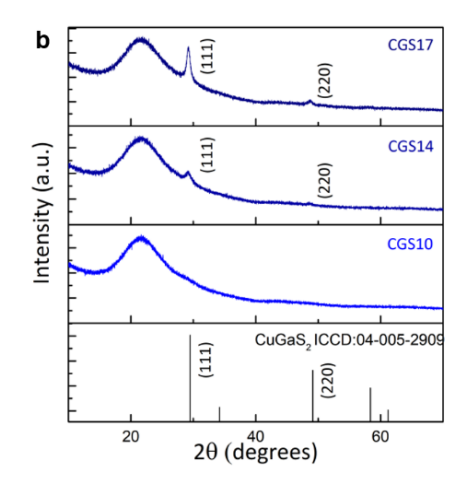


**Fig. 2.3. a)** Yb<sup>3+</sup> emission intensity for sputtered CuGaS<sub>2</sub>:Yb<sup>3+</sup> thin films deposited at room temp (As deposited, CGS10) and 400 °C (CGS14). **b)** XRD diffractograms of samples CGS10, CGS14 and CGS17. Taken from the master thesis of Sem Bergkamp [12]

#### **Pump Speed**

The pump speed is particularly interesting to play with when having trouble with hysteresis behaviour shown in **Fig. 2.4**. The pump itself is always turning full speed, however there is a valve in front of the pump that determines the effective pump speed. Thus by opening the valve wider we can increase the pump speed. The default settings of gas flow (working + reactive gas) and pressure are 15 sccm and 3 mTorr respectively. With these two numbers we can find an effective pump speed of 65 L/s. These values are found to be a nice balance between using not too much gas whilst having good effective pump speed. However, by increasing the pump speed we can 'pump out' the hysteresis. This allows the sputter artist to have more fine tune control over the target condition. To understand this behaviour it is worthwhile to perform multiple hysteresis curves at the same power but at different pumping speeds. In **Fig. 2.4** a quick simulation of the voltage discharge behaviour of an Al target as function of O<sub>2</sub> flow is performed using the RSD software package [13, 14]. We can see that a higher pump speed reduces

the width of the hysteresis. It also delays the onset of the first critical point from 2 to roughly 2.5 O<sub>2</sub> sccm. If oxidation states of the film are an issue, it could be of interest to study the film when sputtering just before the first critical point at each pumping speed. Note that I have personally not attempted to reproduce these results in the lab and that the simulations not modelled to our specific sputter coater, but being aware of the relationship between the pump speed and hysteresis behaviour might be of use.

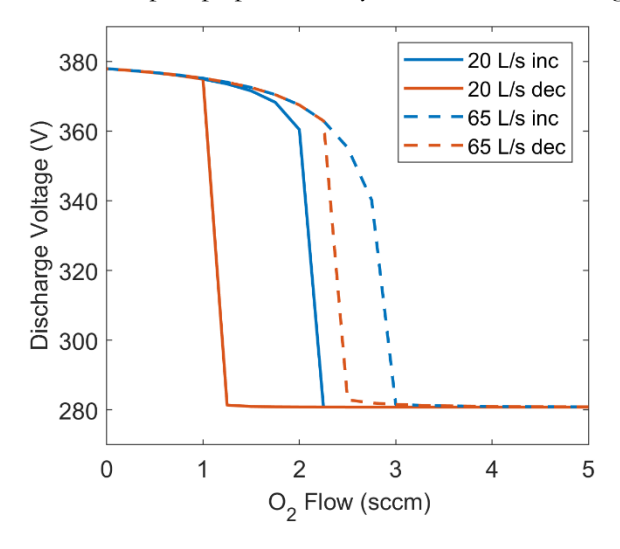


Fig. 2.4. Simulated hysteresis curves using RSD software. Increasing the pump speed results in a less wide hysteresis curve which is referred to 'pumping out' the hysteresis.

#### Magnetic Field Strength

Underneath the target (inside the cathode) there are a series of magnets that trap electrons near the targets to improve plasma stability and increase sputter rates. By tweaking the magnetic field strength we can alter the deposition rate. In the AJA Orion 5 sputter coater the magnets are arranged to have a perimeter of 13 columns of 3 magnets with their south pole facing up and a single column of 3 magnets in the middle with the north pole facing up. This configuration leads to the well-known 'racetrack' that can be seen on a target after some time it's been sputtered. Decreasing the number of magnets (i.e. reducing the magnetic field strength) by, for example, having columns of two or one magnets rather than three, can be helpful to obtain low deposition rates and achieve low doping concentrations in your thin film when power cannot be lowered any further because of plasma stability issues. Note that lowering the magnetic field strength impacts the plasma stability and can make ignition more troublesome.

#### 2.1.3 Thin Film Synthesis Work Flow

After spending four years conducting research on luminescent thin films there is one thing in particular that I wish I had put a larger focus on: the synthesis of the thin films. When sputtering a thin film there most likely is an idea or concept that motivates the making of the film. Before doing any luminescence characterization, it should be a priority to ensure that the film you sputtered is actually what you wish to sputter. In the case of LSCs we often want to have a host material and dope it with some luminescent centres (rare earths are used in this thesis). I would recommend to start by attempting to sputter the host material first and then adding the dopants to be able to compare a dopant free host with the host with dopants. There are a number of ways to verify if what you sputtered is what you actually intended to sputter. What is most accessible at the luminescent materials group at TU Delft is doing energy dispersive x-ray spectroscopy (EDS) to check the stoichiometry, x-ray diffraction (XRD) to check the crystal structure and transmission measurements to check the band-gap and refractive index. The band-gap can be estimated with transmission measurements as there should be a strong absorption edge around the value of the band-gap. The refractive index can be estimated by fitting the thin film interference pattern obtained in a standard transmission measurement (see XY-setup section for more detail). Only after the EDS, XRD and transmission results all indicate that your host material is what you expect, would I continue with adding dopants. Close attention should be paid to the desired doping concentration, therefor EDS measurements can be used to ensure that this is the case. Once the ideal film is made with the right stoichiometry then it can be interesting to make a film with a compositional gradient which is obtained by simply not rotating the substrate. More on this gradient film in the next section. My recommended work flow diagram would look like in Fig. 2.5.

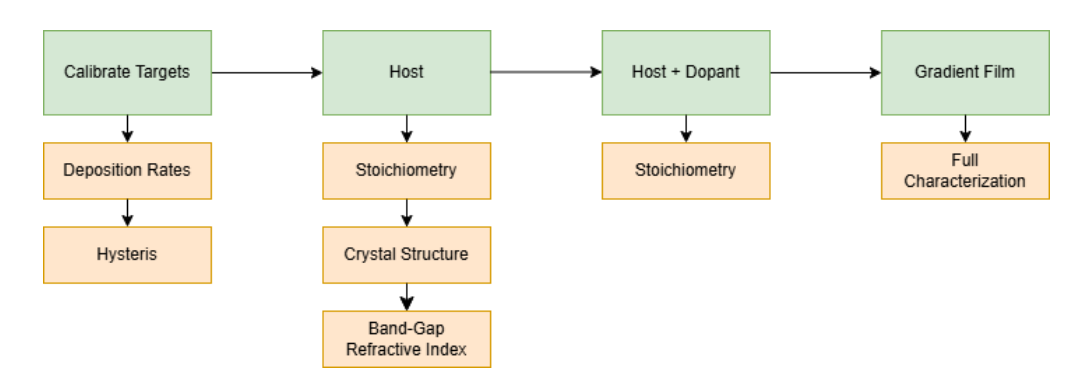


Fig. 2.5. Flowchart depicting the process of making a thin film.

## **Design of Experiments**

It can be tricky to find the specific sputter parameter-set that needs to be tweaked in order to get the desired film. One of my master student, Olivia Kohnstamm, found that attempting to make a CuGaS2 thin film using a single CuGaS2 target was not trivial. The ratio between Cu:Ga:S was never quite 1:1:2 as it should be. In order to obtain the correct stoichiometry she set up a *design of experiments* where she varied several sputter parameters in a systematic way. She chose to vary the working distance, power, substrate temperature and substrate bias. First a set of default parameters were chosen and then they were systematically varied. The results are shown in **Table 2.3**. An experiment like this provides valuable information in order to deposit stoichiometric CuGaS2 in the future. We can see that a lower substrate temperature provides a higher S content and bias voltage can greatly influence the Cu:Ga ratio. This type of experiment generally allows one to become familiar with how certain parameters effect the final films composition.

**Table 2.3.** Atomic percentages (%) of deposited CuGaS<sub>2</sub> films made with varying sputter input parameters. Height (proportional to the working/throw distance), substrate temperature, bias voltage and power were varied. Taken from Olivia Kohnstamm's master thesis [15]

		Cu (%)	Ga (%)	S (%)	Cu/Ga	S/(Cu+Ga)
Height (mm)	30	13.98	38.35	47.68	0.36	0.91
	20	13.43	36.79	49.77	0.37	0.99
	10	12.27	41.34	46.4	0.30	0.87
Substrate T (°C)	500	12.27	41.34	46.4	0.30	0.87
	250	10.85	34.89	54.26	0.31	1.19
	20	9.98	33.3	56.72	0.3	1.31
Bias (Watt)	40	35.74	45.36	18.9	0.79	0.23
	20	41.15	32.51	26.34	1.27	0.36
	0	12.27	41.34	46.4	0.30	0.87
Power (Watt)	75	12.27	41.34	46.4	0.30	0.87
	40	18.85	32.28	48.86	0.58	0.96
	20	19.63	29.41	50.69	0.67	1.04

# Default Sputter Recipe

Once we have fully calibrated our targets and found the input parameters needed to make the film we wish to make, and only then, do we start a process of making a thin film. My default 'recipe' that I use when making a film is shown in **Table 2.4**. The recipe consists of 5 steps. First, we ignite our targets for 10 s with 20 W power and at an elevated pressure of 30 mTorr in an argon environment (the same as we would when starting a hysteresis experiment). Next, we lower the pressure to the working pressure

(typically 3 mTorr) and ramp up the power of the targets to the value we used when calibrating our targets. Ramping is done at a maximum rate of 1 W/s, slower can be done if one thinks a target is particularly fragile. Once at the desired power levels some 180 s are used to ensure a steady, self-sustaining plasma is formed. The third step is introducing the oxygen to the chamber and allowing again some time for the plasma to stabilize. Deposition is the fourth step which just involves moving the substrate shutter away from the substrate. After deposition we cover the targets and substrate and ramp down to 20 W. Note that when not doing reactive sputtering the 3<sup>rd</sup> layer would be omitted. Should substrate heating be done then this should happen at the ignition stage.

**Table 2.4.** Default sputter recipe when depositing a thin film. The power for each target during deposition ( $P_{Dep}$ ) and reactive gas flow ( $O_{sccm}$ ) is found during the calibration phase. Ramp<sub>t</sub> is the time it takes to ramp up to a certain power level, generally done at 1 W/s.

Layer	Name	Press. (mTorr)	Power (W)	Ar/O <sub>2</sub> Flow (sccm)	Time (s)
1	Ignition	30	20	15/0	10
2	Ramp + Presputter	3	$P_{Dep}$	15/0	Ramp <sub>t</sub> + 180
3	O <sub>2</sub> + Presputter	3	$P_{Dep}$	$15-O_{sccm}/O_{sccm}$	180 s
4	Deposition	3	$P_{Dep}$	15-O <sub>sccm</sub> /O <sub>sccm</sub>	Time <sub>Dep</sub>
5	Ramp Down	3	20	15/0	Rampt

If the default recipe results in the desired film with the correct stoichiometry, crystallinity and thickness then it is interesting to simply turn off the rotation of the substrate and create a composition gradient in the film. A single, high quality, gradient film can generate a lot of data. It is worth exhausting the data available from the gradient film first, before making subsequent films.

# 2.1.4 Troubleshooting

The final sputtering related information I would like to share are some common practical issues that arise when sputtering. I have divided this section in the two main problems I have most often encountered in my four years. The key to troubleshooting is having a firm understanding of how each input parameter effects the sputtering process.

# Plasma fails to ignite/Plasma stability

A dull or non-existing plasma when attempting to ignite is probably one of the most common issue and can have a number of different causes. The first attempt at fixing this is the classic: "Have you tried turning it off and on again?". In this, I would include changing the power cable and using a different power supply to eliminate the possibility that it's a power supply issue. More often than not this will not fix the issue, in which case I would try the following. If using a DC supply, try it with the RF supply. If the RF supply is used, ensure that the load and tune value of the matching network is set to 50 for both. Monitor the load and tune value along with any reflected power (reflected power should be (). Having the substrate bias or another target on can aid in the ignition of a troublesome target. The aiding plasma is sometimes referred to as the 'helper plasma'. Plasma stability can generally be improved by increasing the pressure, note however that that the deposition rate will fall as a result. Ensure that the target shutters are open when igniting. In fact I would always have the target shutter open when sputtering and use the substrate shutter, rather than the target shutter, to prevent deposition. The target shutter strongly influences the local geometry of the plasma, whereas the substrate shutter will not. If possible, increase the magnetic field strength by adding more magnets. Make sure that there is no short circuit between the cathode and anode by measuring the resistance between the centre pin and the outside of the connector on the bottom of the sputter gun. This should be somewhere in the order of mega ohms. Last but not least, inspect the target by opening the chamber. Flaking, which chiefly occurs inside the chimney of the sputter gun, can result in arcing (which is often accompanied by a flickering of the plasma). If there are signs of flaking then clean the sputter components.

# Thin Film Composition

Getting the right stoichiometry for your thin film can be tricky. Each sputtered ion interacts with the plasma differently and can lead to different deposition rates. Things like the sticking coefficient, mean free path, mass, surface binding energy and more all influence the deposition rate and are either out of our control, or impossible to independently influence. Reducing the deposition rate of a specific target without altering all the other targets can be done in the following way. Lower the power (10 W is around the minimum required power). Switch from DC to RF (sputter rate is roughly halved). Reduce the magnetic field strength. If possible, angle the sputter target away from the substrate. Install a grid/mask on top of the chimney. To increase the deposition rate the opposite of the previous listed things can be done. Another way to increase the deposition rate is by simply adding another target of the same material. Controlling the oxidation phase of the deposited film is perhaps the most difficult. For this I would recommend investigating the working/throw distance. One can also play with the lateral distance to the target. Generally the closer the substrate is to the target the less oxidized the film is, this can be observed by sputtering a gradient film. In Fig. 2.6 a gradient film is shown where the host material is SiAlO. Metal Si/Al alloy target

is sputtered from a single target located towards the bottom of the film in a mixed Ar/O atmosphere. As can be seen on the photo, the film has a yellow/brown tint at the bottom of the film. This color has been attributed to absorption due to oxygen vacancy defects. This has been confirmed with EDS results that show that the top of the sample has roughly 65% O content, whilst the bottom an average of 61% O content. To have more fine tune control of the hysteresis one can try to adjust the effective pumping speed which allows the user to get closer and closer to the first critical point without going over. I would suggest conducting a design of experiments described in **Table 2.3**.

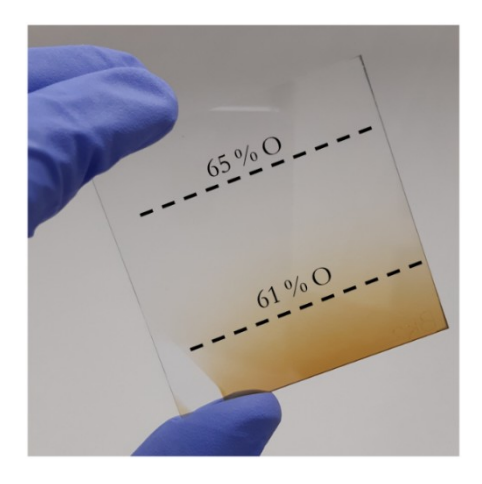


**Fig. 2.6.** A gradient compositional SiAlO:Sm film. The metallic, compound SiAl target is installed on the bottom side of the sputter coater. The film on the bottom side has an O content is 61 % whereas to the top of the film the O content is 65 %, both are regions are indicated by the dashed line.

# 2.1.5 Cleaning Procedure

There comes a time when the chamber is due for a deep clean. It can happen that cleaning the system can resolve some problems related to plasma instability. The deep cleaning of the sputter coater is a days' worth of work. Luckily the process is quite simple and is described in the steps below. After reaching atmospheric pressure by turning off the pump and before opening the chamber, it is important to always close the main valve to protect the turbo-molecular pump.

- 1. Remove current targets
- 2. Remove substrate holder and the 4 sputter gun components of each gun:
  - a. Target clamp
  - b. Ground shield
  - c. Chimney

- d. Shutter
- 3. Optional is to remove the QCM arm, substrate shutter and the large ring around the heating lamps
- 4. Sand blast substrate holder, sputter components and optional components
- 5. Wash sputter components in ultrasonic bath
  - a. 20 minutes in soapy water
  - b. 20 minutes in ethanol
- 6. Place sputter components in an oven to remove moisture
- 7. Use sandpaper to sand off the inside of the sputter chamber
- 8. Use a vacuum cleaner to remove any dust build-up after sanding the chamber walls. Wipe the surfaces with a lint-free tissue and some ethanol
- 9. If needed use a glass polish to clean the inside of the viewing windows
- Install new targets and re-assemble sputter gun components and optional components
- 11. Close chamber, open main valve and evacuate.
- 12. Achieve a lower base pressure by heating the chamber using the custom bake jacket for 8 hours at 90 °C or less
- 13. Sputter clean target surfaces to remove any oxygen contamination

This deep clean should be conducted anytime there is a change in targets to avoid contamination and after a period of heavy usage. The cleaning can be nicely split between two people where one sandblasts the sputter components while the other cleans the inside of the chamber.

**Safety**: During the cleaning of the chamber a lab coat, gloves, protective eye wear and a FFP3 mask should be worn at all times. When working with hazardous reactive gasses like  $H_2S_2$  a suitable detector should be used.

With that we have covered how to synthesize our thin films using a sputter coater. An equally important part of thin film research is the characterization of the properties of the thin film. In the case of my research the optical and luminescent properties are of particular interest.

# 2.2 Gradient Composition Thin Film Characterization

Once the ideal film is made in terms of composition and crystallinity it is time to characterize the thin films properties. There are four key photoluminescence properties that are included in almost any research article regarding photo-luminescent materials:

- Excitation
- Emission

- Radiative lifetime
- Quantum yield

We want to know at which wavelengths of excitation results in emission (Excitation). Then at which wavelengths our emission takes place (Emission). How long does our emission lasts for after pulsed excitation (Radiative lifetime). Lastly, what fraction photons that we use to excite our material result in emitted photons (Quantum yield). Jeffrey, a colleague, would call this the bread and butter of luminescence characterisation. There are more exotic properties such as up/down-conversion, energy transfer, temperature, power or pressure dependence, transient vs steady-state and more. In addition, optical properties such as transmission, reflectance, refractive index, optical band-gap, surface roughness and more are hard to miss in any thin film research article.

Combining the composition, crystallinity, photoluminescence and optical properties of thin films provides the ground work for a plethora of fascinating thin film research. However, the infinite number of compositions of a gradient thin films that must be characterized can be overwhelming. Luckily there is a technique developed at the luminescent materials group at TU Delft that expedites the characterisation of a range of properties using what is called the 'gradient sputter method' or 'XY method'. The idea is simple. Create a thin film with a compositional gradient simply by sputtering multiple sputter targets (combinatorically) at right angles from one another while not rotating the substrate. Then perform position-dependent measurements on the thin film. Combining the position dependent composition and luminescent properties allows one to plot composition vs luminescent properties. At TU Delft, this technique was first used by Michiel de Jong on Ca<sub>3</sub>Si<sub>2</sub>N<sub>2</sub>O<sub>4</sub>:Eu<sup>2+</sup> and NaCl:Tm<sup>2+</sup> thin films [16, 17]. The technique was further developed and put in the spot light by an article dedicated to this method by Evert Merkx [18]. When Evert left the group in 2020, so did the knowledge on how to properly operate and maintain the XY experimental set-up. Not before long the XY set-up became unusable due to software issues. In comes my first master student, Bauke Kooger, and he single handily builds the XY set-up from the ground up with new features and a focus on user friendliness. He summarized his project in his master thesis which serves as a great starting point to learn about software development and the XY-method [19]. In the following sections I aim to provide a 'quick start guide' for how to implement the XY-method. First we look in detail at the position dependent composition of thin films using EDX. This is followed in somewhat less detail by the position dependent transmission, excitation/emission and radiative lifetime measurements of thin films. The goal of this method is to map or relate the composition of the thin film to luminescent/optical properties.

## 2.2.1 Composition - EDX/EDS

Energy dispersive x-ray spectroscopy (EDX/EDS) is a common technique used to determine the composition of various materials. The operating principle is quite simple. Using an electron microscope to bombard a material with electrons. Incoming electrons can eject electrons from atoms inside our material. The ejected electron leaves a hole behind which can be filled by other electrons bound to the atom. The difference in energy is released as a characteristic x-ray which can be measured. Each atom emits unique x-rays with a specific energy, as the name characteristic x-ray would suggest. This way we can find out what our film is made of.

For details on the technique, and how to perform the measurements properly, one should consult a dedicated lab technician specialized in the experimental set-up. Wrong input parameters of the electron microscope (acceleration voltage, probe current, working distance, pressure, integration time and more) can lead to erroneous results which can cause difficulty in the interpretation of the data.

I will now go over, step by step, my process of determining the position dependent composition of a thin film. I have chosen to use a sample that consists of Yttrium, Aluminium, Chromium, Neodymium and Oxygen to serve as an example. The first step is to prepare the sample for measurements and to choose the positions on the film. Then we simply perform the measurements on each position. In **Fig. 2.7**a we see positions marked on a film at which we will perform the measurements. Performing, in this case, 6x4 measurements can be tedious. With some smart programming, one can develop an 'auto-clicker' which can automate button-clicks required to move the stage, start the measurement and save the data. Something worth looking into. **Fig. 2.7**b shows the spectrum of one measurement circled in **Fig. 2.7**a. There is a broad background signal due to so-called bremsstrahlung, or 'braking radiation'. On top of the bremsstrahlung are several peaks, each associated with the elements present in our thin film. Note that Si is present which is a contribution from the glass substrate mainly made of SiO<sub>2</sub>. The presence of O in the substrate can also introduce difficulties in determining O values.

The built in software of the JEOL electron microscope can analyse the spectrum shown in **Fig. 2.7**b and estimate the atomic or mass percentage of each element present in the measurement. Such a table is shown in **Table 2.5** for the measurement shown in **Fig. 2.7**b.

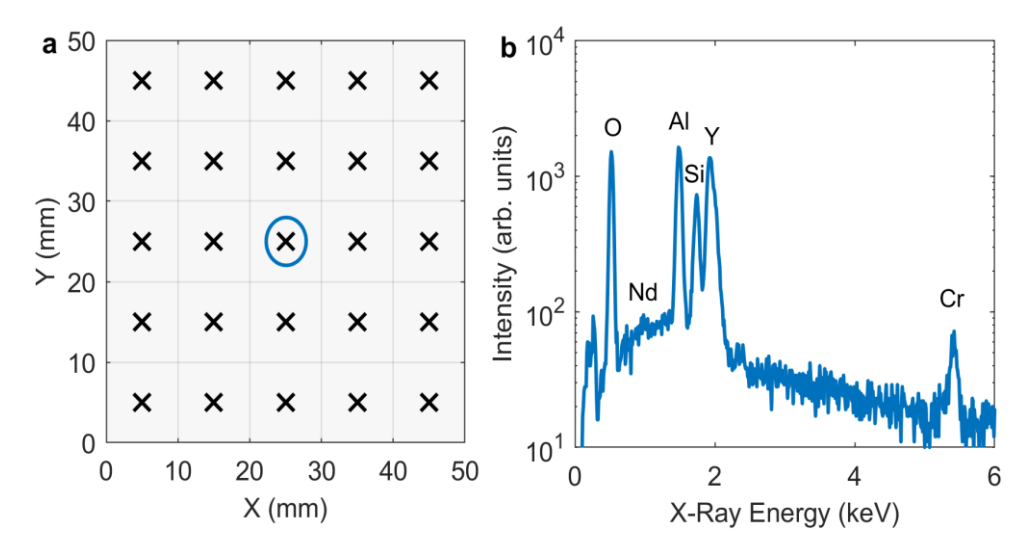


**Fig. 2.7. a)** Schematic of the thin film with black 'x' markers to indicate at which positions EDS measurements are done. The EDS measurements performed at the marker circled in blue is shown in b. **b)** EDS spectrum shown for the measurement circled in a. Characteristic x-ray peaks are labelled for O, Nd, Al, Si, Y and Cr.

**Table 2.5** Values obtained by the software for elemental composition of the spectrum shown in **Fig. 2.7**b.

Formula	Mass (%)	Atomic (%)
С	2.67	6.59
О	30.70	56.87
Al	12.61	13.85
Si	5.44	5.74
Cr	3.80	2.17
Y	43.70	14.57
Nd	1.09	0.41
Total	100	100

Note that every EDS measurement will likely show some form of carbon contamination. We know that the most stable oxidation state for these cations is 3+, or in other words, each cation forms  $X_2O_3$  (X=Y, Al, Cr, Nd). If we assume that our sample is fully oxidized, then we know that 40% of all atoms are cations. Remember that the nature of the research behind this compositional gradient is to establish trends rather than absolutes. Another thing worth pointing out is that the O content tends to be unreliable due to the difficulty in measuring O accurately with EDS and due to a contribution by the substrate. Lastly, low atomic concentrations (<1%) are prone to large errors or can be difficult to measure all together. Multiple measurements can

reduce the errors and longer integration times can assist in detection. Once again, this method is useful in revealing trends, as an exact measurement is not always necessary.

Summarizing the composition of each position in a table such as **Table 2.6** is a good starting point for analysis.

**Table 2.6** Summary of composition of the film for each position indicated in **Fig. 2.6**a. Atomic percentages of the cations are normalized to 100 %

Position (mm)		Cation (%)					
X	y	Al	Y	Cr	Nd		
1.6	9.5	22.77	71.83	5.27	0.12		
1.6	20.5	31.42	63.41	4.47	0.71		
1.6	31.5	42.46	51.2	5.47	0.88		
1.6	42.5	55.89	39.75	3.65	0.71		
9.6	9.5	24.04	72.03	3.8	0.13		
9.6	20.5	33.31	61.18	5.41	0.1		
9.6	31.5	43.58	49.32	5.94	1.15		
9.6	42.5	58.33	36.31	4.95	0.4		
17.6	9.5	23.84	68.32	7.11	0.73		
17.6	20.5	32.67	59.91	7	0.43		
17.6	31.5	44.95	47.29	7.04	0.71		
17.6	42.5	57.02	36.63	5.83	0.52		
25.6	9.5	24.21	66.18	8.76	0.85		
25.6	20.5	33.89	58.25	7.86	0		
25.6	31.5	45.51	47.24	7	0.26		
25.6	42.5	57.51	34.39	7.91	0.2		
33.6	9.5	24.44	64.44	10.29	0.83		
33.6	20.5	34.14	55.5	9.52	0.85		
33.6	31.5	45.8	43.18	11.02	0		
33.6	42.5	58.42	32.26	8.59	0.73		
41.6	9.5	24.08	63.69	11.98	0.26		
41.6	20.5	34.42	53.28	11.71	0.59		
41.6	31.5	46.62	42.76	10.51	0.1		
41.6	42.5	59.93	31.14	8.92	0		

To further curate the data, I like to create 2D grids with each grid point resembling a single measurement on a x (mm), y (mm) location (n x m, n = number of y measurements, m = number of x measurements) of each column in **Table 2.6**. In this

example that results in 6 grids, 2 grids for the position (x and y) and 4 grids for the cation percentage (Al, Y, Cr and Nd). Note that this organization of data is also used by the custom software for the XY photoluminescence set up described later. An example of these grids are shown in Fig. 2.8. The x position grid (Fig. 2.8a) are constant along the columns whereas the y position grid (Fig. 2.8b) is constant along the rows. The Al cation percentages shown in Fig. 2.8c quickly tells us that along the columns the Al percentage is fairly constant, while there is a clear increase going from the top to the bottom row. In the case of Cr (Fig. 2.8d) we can see an overall increase in cation percentage from left to right. These grids can be used as a quick sanity check to see if the orientation of the installed sputter targets matches with the expected compositional gradient i.e. that Al was installed on the top position of the sputter coater and that Cr installed on the left side. Remember that in the sputter coater the film is facing down, whereas for any other measurements (compositional or otherwise) the film is facing up. In my case I flip the sample along the vertical, so left becomes right and right becomes left, top and bottom remain the same.

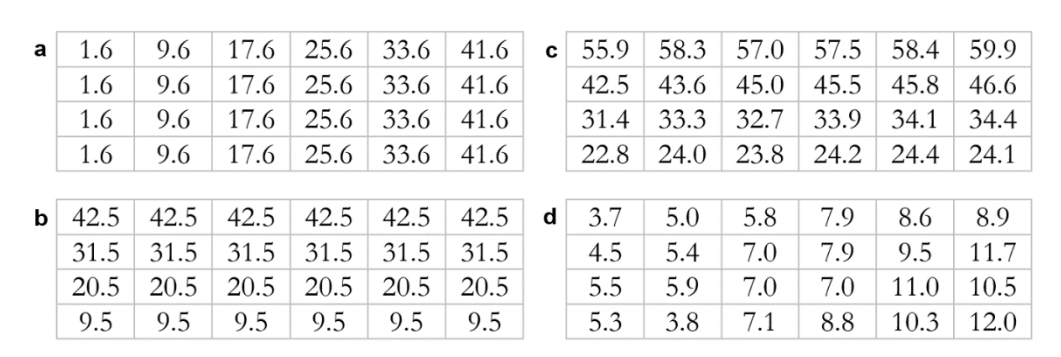


**Fig. 2.8.** Grids to show the x and y position (mm) of the measurements (a) and (b). Grids to show the cation percentages (%) of Al (c) and Cr (d).

With the x and y position, along with an element we can generate 3D plots or 2D heat maps. In **Fig. 2.9**a the Al cat % is presented as a heat map. We can see from **Fig. 2.9**a that we do not cover the composition of the entire film and the colors do not transition particularly smoothly. In order to create a smooth heat map requires more data points than a 6x4 grid of data points. This is where we can interpolate and extrapolate are data. There is a somewhat complicated equation called the 'surface source evaporation equation', which considers the geometry of the sputter coater in order to model the spatial mass deposited upon your substrate [18]. Other simulation software such as SRIM and SIMTRA can also be used to model the sputtering process and give the composition across the entire film [20, 21]. However, I have found that a good old

fashioned 2 dimensional linear fit works quite well. Once again, it is about trends, rather than absolute values. In **Fig. 2.9**b the data has been 2D linearly fitted to a 12x12 grid across the entire film resulting in a satisfying looking heat map suitable for publication. For more compositional heat maps made using this method, I forward the reader to **Chapter 4** where Al<sub>2</sub>O<sub>3</sub>-Y<sub>2</sub>O<sub>3</sub> doped with Cr and Nd is studied in more detail.

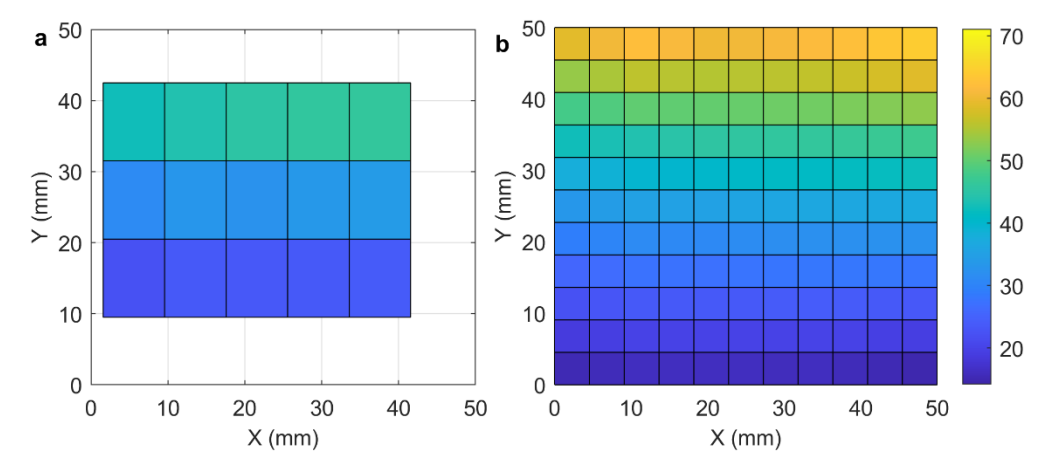


**Fig. 2.9. a)** Example of a schematic of the film with a projected heat map of the Al cation (%). The heat map combines the data from **Fig. 2.8**a, b and c. b) The Al cation (%) of the entire film found by linearly interpolating and extrapolating the data in **a**.

I would like to quickly mention one other interesting way of presenting the composition of your thin film through the use of ternary diagrams. Triangular ternary diagrams allows one to project your thin films composition for three species in a single diagram. As an example, in **Fig. 2.10** we can see the cation composition of a SiAlO:Sm thin film in a single diagram and show that a single thin film can have a 'library' of compositions [18]. The outline and shaded area represents the thin film. Each point on the diagram adds up to 100%. For example the point circled in blue has 80% Si, 10% Al and 10% Sm. The values can be found by paying attention to the direction of the axis ticks. The shaded area, representing the thin film, can also be replaced by a color heat map representing for example a luminescent property of the thin film, like the Sm luminescence intensity. For examples of such diagrams I would recommend visiting previous work done by Evert and others [18, 22, 23]. These type of diagrams can be easily constructed with software such as OriginPro.

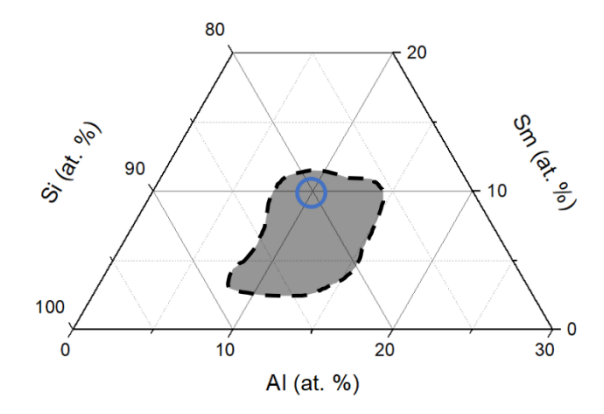


Fig. 2.10. An example of a ternary diagram used to show the composition 'library' of a single gradient sputtered thin film.

The aim of this section was to guide the reader through the work flow of finding the composition across a compositional gradient film. Now it is time to move on to the optical and luminescent properties of the film using the custom XY set-up. Unlike this section, there are numerous reports done by master students at the TU Delft on how to perform these measurements and do the subsequent analysis. There is a dedicated master thesis to this very set-up and a scientific publication [18, 19]. For this reason I will not go into detail on the how and what, but rather briefly mention the capacity at which it is used throughout this thesis.

# 2.2.2 The XY Set-Up

The XY Set-up is a nifty custom built experimental set up used in the research group at TU Delft. The inventor is Evert Merkx and my master student Bauke Kooger built upon his work. The set-up is relatively simple and is shown in **Fig. 2.11** (left). It uses two linear translation stages to move your sample around indicated by yellow boxes. There are two input light sources, a laser and a broadband light source, shown in the top left corner of **Fig. 2.11** (left). The former is to excite your sample at certain wavelengths and in pulses, whereas the latter is to investigate overall transmission. We collect the output with an optical fibre connected to a spectrometer or photomultiplier tube (PMT), these are labelled optics transmission/emission in **Fig. 2.11** (left). The set-up includes various optical components such as lenses, mirrors, prisms beam-splitters and more, but I will not go into detail of each. Finally, there is also a power meter that can be positioned on various location in the laser path and can be read out by the software.

The beauty in the set up lies in the programming that automates the process of doing many measurements on a single film. The software controls various instruments such as the stages, a digitizer, tuneable laser, shutter, spectrometer and power meter in a systematic way. In Fig. 2.11b we see the main menu to choose an experimental mode, like transmission, excitation/emission or decay. Each applicable instrument is read-out for each measurement and is neatly packaged in a single output file. There is something satisfying about programming the software to measure at 10x10 positions on your film and hearing the stages move, the laser changing wavelengths, shutters opening, spectrometers updating and then moving to the very next point. It would be unnecessary for me to go into detail about the workings of the software and how to design such an experimental set-up when it has already been done by my aforementioned master student: Bauke. To give an impression of the software, the main screen of the excitation/emission set up is shown in Fig. 2.12a. The read out of the spectrometer and power meter are shown in the blue and orange boxes respectively. A number of measurements on the film can be chosen as shown by the schematic in the black box. On the right hand side of the main screen there are various widgets (which are illegible in Fig. 2.12a) that allow the user to program the different instruments used during the experiment. Examples of the standalone widgets are shown in Fig. 2.12b-d. If you are interested in learning how to program instruments and automate measurements, I highly recommend his master thesis. Bauke's thesis also goes into detail on how to perform the measurements.

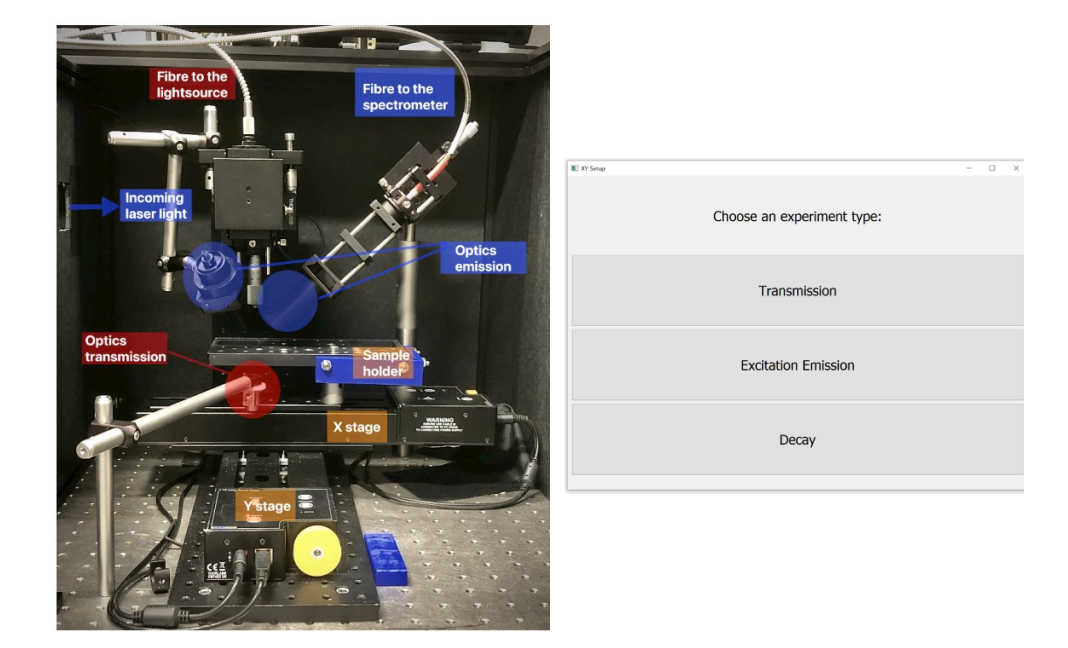


**Fig. 2.11. Left:** front view of the custom XY set up at the luminescent materials research group at TU Delft. **Right:** Main menu of the custom made accompanying software of the XY set-up. Taken from the master thesis of Bauke Kooger [19].



Fig. 2.12. a) Main screen of an excitation-emission measurement. b. Widget for metadata of the output file. c) Widget to control the laser. d) Widget to control the spectrometer.

The output file given by the XY set-up can be read out using custom built software developed in MATLAB. Again more information on this can be found in other reports. In short, an user interface (UI), also called the 'data picker', can read in the experiments output file (.hdf5) and shows a schematic of the thin film with markers where the measurements have been done. This interface is shown in Fig. 2.13, where the blue outline shows the schematic of the film and the black outline is where the user can choose settings such as the plotting the desired wavelength range, normalizing the data or fitting the data. The heat map shown on the schematic of the film represents the emission intensity in this example. The markers on the UI can be clicked whereby in a separate window the measurement of that position is shown. Multiple positions can be clicked to reveal and compare multiple measurements. In Fig. 2.14a the plotted measurements are shown while in Fig. 2.14b the position at which these measurements were taken are shown. If applicable, multiple measurements at the same position can also be shown, for example when multiple excitation wavelengths are used on a single position. This can also been seen in Fig. 2.14a. Functionality of the software includes the normalization of data, removing background, selecting ranges of data and also

automated fitting protocols. For transmission measurements the thin film interference (if observed) can be fitted using the Swanepoel method. An algorithm in the XY set-up software is used to fit over the entire film to retrieve the thickness and refractive index across the entire film. For excitation and emission measurements, peaks can be fitted with Gaussian functions. Radiative lifetime measurements can be fitted with by a single or double exponential functions. All these tools allow one to compare various properties to one another and unlocks a vast amount of data in a single thin film. The XY set-up has provided the foundation of the research in this thesis. Examples of using it are shown in the next three chapters and are therefore not included in this section. For more information on the set-up the reader can read the experimental methods sections in **Chapter 4** and **Chapter 5**.

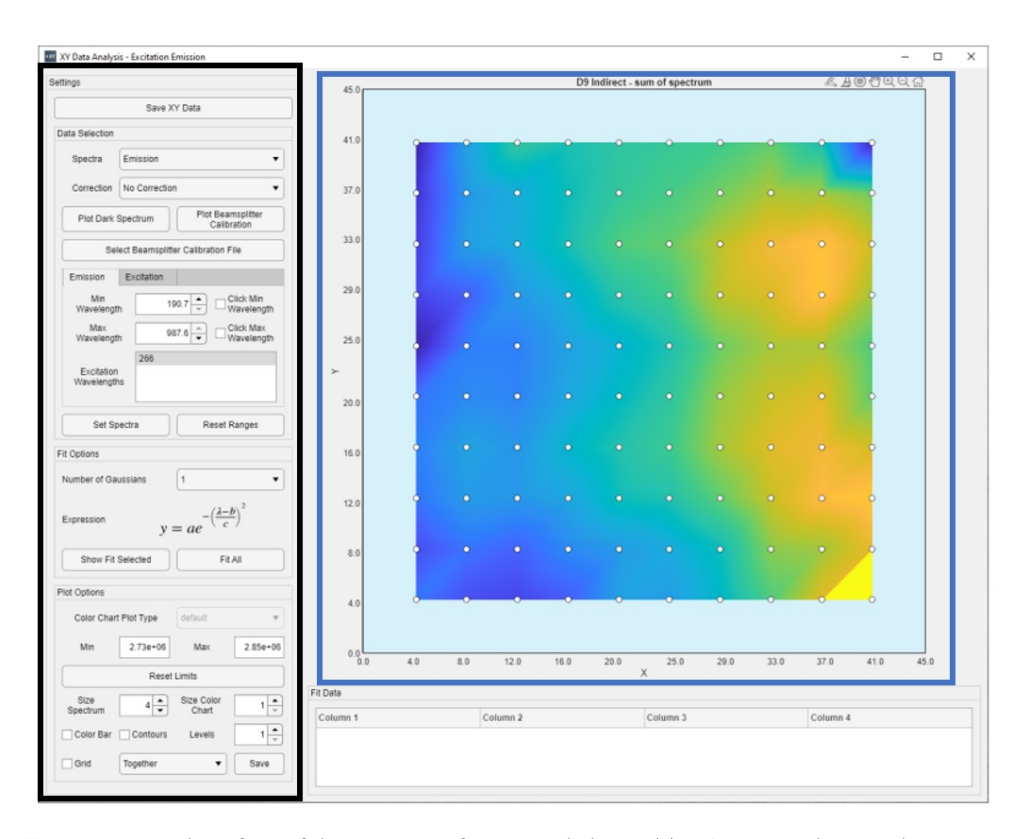


Fig. 2.13. User interface of the custom software made in MATLAB to complement the XY Set up.

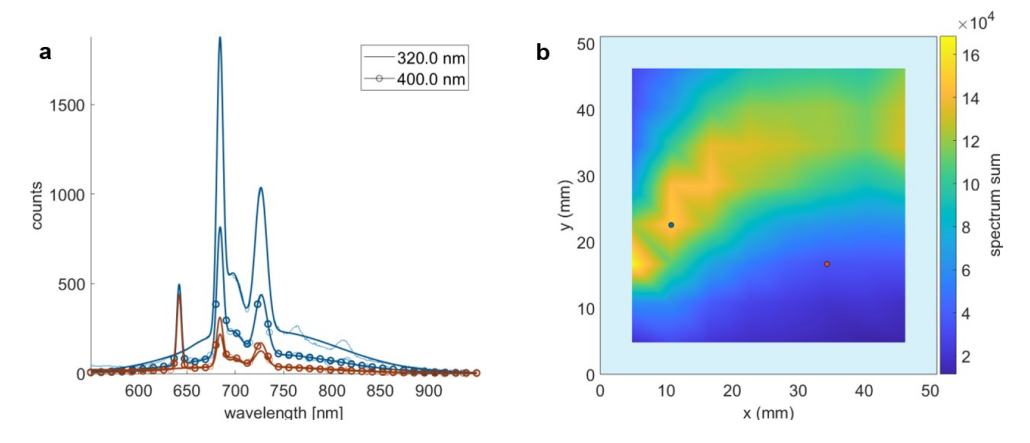


Fig. 2.14. a) Emission measurements at multiple excitation wavelengths plotted after clicking the positions in the UI shown in Fig. 2.13. b) The heat map represents the integrated intensity of the wavelength range selected.

## 2.3 Closing Remarks

The compositional gradient thin film research opens many doors for possible research directions. The custom XY set up lays down the ground work for characterising thin films. To anyone who continues with this research I would suggest to first learn the basics of the tools and then build upon them with your own scripts. Writing short programs to automate tasks such as fitting protocols, extracting radiative lifetimes or plotting various graphs are mandatory tools in this type of research given the vast amount of data. The act of writing scripts improves programming skills and also invites one to think about what you want to do with acquired data in general. Lastly, it can be great timesaver to have scripts that generate figures and heat maps in a way that make them publishable. These remarks are applicable to most research projects and can perhaps be perceived as trivial to the experienced scientist, however for those starting out in academia it is something that can't be learned early enough.

#### 2.4 References

- [1] M. Ohring, Materials Science of Thin Films: Depositon and Structure. Elsevier Science, 2001.
- [2] D. Depla and S. Mahieu, Reactive Sputter Deposition. Springer Berlin Heidelberg, 2008.
- [3] K. Seshan, Handbook of Thin Film Deposition. Elsevier Science, 2012.
- [4] K. Wasa, I. Kanno, and H. Kotera, Handbook of Sputter Deposition Technology: Fundamentals and Applications for Functional Thin Films, Nano-Materials and MEMS. Elsevier Science, 2012.
- [5] D. Depla, Magnetrons, Reactive Gases and Sputtering. Lulu.com, 2017.
- [6] J. Tesař, J. Martan, and J. Rezek, "On surface temperatures during high power pulsed magnetron sputtering using a hot target," Surface and Coatings Technology, vol. 206, no. 6, pp. 1155-1159, 2011.
- [7] D. Depla, S. Heirwegh, S. Mahieu, J. Haemers, and R. De Gryse, "Understanding the discharge voltage behavior during reactive sputtering of oxides," *Journal of Applied Physics*, vol. 101, no. 1, 2007, doi: 10.1063/1.2404583.
- [8] W. D. Sproul, D. J. Christie, and D. C. Carter, "Control of reactive sputtering processes," Thin Solid Films, vol. 491, no. 1, pp. 1-17, 2005/11/22/ 2005, doi: https://doi.org/10.1016/j.tsf.2005.05.022.
- [9] F. Wang, Y. Abe, M. Kawamura, K. H. Kim, and T. Kiba, "High-rate sputter deposition of chromium oxide thin films using water vapor as a reactive gas," *Surface and Coatings Technology*, vol. 387, p. 125509, 2020.
- [10] M. Chandra Sekhar, P. Kondaiah, S. V. Jagadeesh Chandra, G. Mohan Rao, and S. Uthanna, "Effect of substrate bias voltage on the structure, electric and dielectric properties of TiO2 thin films by DC magnetron sputtering," *Applied Surface Science*, vol. 258, no. 5, pp. 1789-1796, 2011/12/15/ 2011, doi: https://doi.org/10.1016/j.apsusc.2011.10.047.
- [11] J.-C. Park, M. Al-Jassim, and T.-W. Kim, "Optimization of vertical and lateral distances between target and substrate in deposition process of CuGaSe2 thin films using one-step sputtering," *Materials Express*, vol. 7, no. 1, pp. 35-42, 2017, doi: 10.1166/mex.2017.1349.
- [12] S. Bergkamp, "Ytterbium doped chalcogenides as a coating for the LSC application," Masters, Radiation Science & Technology, University of Technology Delft, 2022.
- [13] K. Strijckmans and D. Depla, "A time-dependent model for reactive sputter deposition," *Journal of Physics D: Applied Physics*, vol. 47, no. 23, p. 235302, 2014.
- [14] K. Strijckmans, R. Schelfhout, and D. Depla, "Tutorial: Hysteresis during the reactive magnetron sputtering process," *Journal of Applied Physics*, vol. 124, no. 24, 2018.
- [15] O. Kohnstamm, "Tuning the bandgap of Yb3+ doped Cu(Al,Ga,In)S2 and CuGa(O,S,Se)2 for LSC applications," Masters, Radiation Science & Technology, University of Technology Delft, 2023.
- [16] M. de Jong, W. Kesteloo, and E. van der Kolk, "Deposition of luminescent NaCl:Tm2+ thin films with a Tm concentration gradient using RF magnetron sputtering," *Optical Materials*, vol. 46, pp. 149-153, 2015/08/01/ 2015, doi: https://doi.org/10.1016/j.optmat.2015.03.061.
- [17] M. de Jong, V. E. van Enter, and E. van der Kolk, "DC/RF magnetron sputter deposition and characterisation of Ca3Si2N2O4: Eu2+ luminescent thin films," *Journal of Luminescence*, vol. 164, pp. 52-56, 2015.
- [18] E. P. J. Merkx and E. van der Kolk, "Method for the Detailed Characterization of Cosputtered Inorganic Luminescent Material Libraries," ACS Combinatorial Science, vol. 20, no. 11, pp. 595-601, 2018/11/12 2018, doi: 10.1021/acscombsci.8b00068.
- [19] B. Kooger, "A Scanning Spectroscopy Setup for Optical Characterization of Gradient Thin Films," Masters, Radiation Science & Technology, University of Technology Delft, 2022.
- [20] K. Van Aeken, S. Mahieu, and D. Depla, "The metal flux from a rotating cylindrical magnetron: a Monte Carlo simulation," *Journal of Physics D: Applied Physics*, vol. 41, no. 20, p. 205307, 2008.
- [21] J. Biersack and J. Ziegler, "The stopping and range of ions in solids," in Ion Implantation Techniques: Lectures given at the Ion Implantation School in Connection with Fourth International Conference on Ion Implantation: Equipment and Techniques Berchtesgaden, Fed. Rep. of Germany, September 13–15, 1982, 1982: Springer, pp. 122-156.

- [22] E. P. Merkx, S. van Overbeek, and E. van der Kolk, "Functionalizing window coatings with luminescence centers by combinatorial sputtering of scatter-free amorphous SiAlON: Eu2+ thin film composition libraries," *Journal of Luminescence*, vol. 208, pp. 51-56, 2019.
- [23] D. de Vries, S. van Overbeek, E. P. Merkx, and E. van der Kolk, "Sm2+-doped SiAlO sputter deposited coatings for self-absorption and scatter-free luminescent solar concentrator applications," *Journal of Luminescence*, vol. 225, p. 117321, 2020.

# 3 Sm<sup>2+</sup> in Glass

The main objective of this thesis is to explore ways to increase absorption in thin film, rare earth based LSCs. This chapter presents my maiden attempt to do so with divalent samarium (Sm) doped in glass materials such as aluminium borosilicate (SiAlBO) and strontium borate (SrBO). Divalent Sm, unlike trivalent Sm, has strong and broad  $4f^6 \rightarrow 4f^5 5d^1$  absorption in the visible part of the spectrum. Subsequent non-radiative relaxation from the  $5d^14f^5$  to an excited  $4f^6$  state can result in narrow radiative  $4f^6 \rightarrow 4f^6$  transitions. The parity forbidden  $4f^6 \rightarrow 4f^6$  emission from  $5m^{2+}$  is beneficial in minimizing self-absorption. In this chapter a short introduction is given about the spectroscopic differences between trivalent and divalent samarium along with past research done on samarium doped in silicates and strontium borates. The key challenge addressed in this research project is that of the poor solubility of  $5m^{2+}$  in silicate based glasses. Sm inside silicates generally prefers to be in the undesired, poor absorbing, trivalent state. The aim of this work is to improve the incorporation ability of  $5m^{2+}$  in the glass matrix by introducing boron (B) as a co-dopant.

#### Challenges, Setbacks and Lessons Learned

The work presented in this chapter has gone unpublished, but still encapsulates a lot of work done in the first two years of my PhD. This chapter also represents the nearly universal experience of each PhD student where a certain project does not develop into a publication. There are many reasons why a piece of scientific work goes unpublished: unreproducible results, insufficient novelty or significance, failed experiments, arguments with collaborators, setting a too high standard for oneself or perhaps finding a previous study that covered the topic at hand in detail. A large time-sink in this project was on the experimental side where in particular the sputtering of Boron was troublesome. Two boron sputter targets had broken due to lack of proper target calibration described in **Chapter 2**. To add to that, the incorporation of B simply did not yield any significant increase in Sm2+ emission intensity. Lastly, the lack of systematic research conducted during this time made it difficult to present the results in a scientific paper. However, going through the data a couple of years later and equipped with more knowledge and experience I have decided to come back to this topic because the results contain valuable information on utilizing industry practises of thin film synthesis techniques to fabricate thin film LSCs not published before.

#### 3.1 Introduction on Sm<sup>2+</sup> and Sm<sup>3+</sup> luminescence

As stated in the general introduction, all lanthanides have a stable trivalent state. However, trivalent europium and ytterbium only need one extra electron to obtain an energy favourable half or fully filled 4f orbital, therefor Eu<sup>2+</sup> and Yb<sup>2+</sup> are relatively stable as well. The neighbours to the left of Eu and Yb in the periodic table, Sm and Tm, are also found in their 2+ states as they have a nearly half or fully filled 4f orbital respectively [1]. The singly added electron when going from a 3+ to 2+ ion has great consequences on its spectral properties. The ion becomes larger due to an increase in the repulsion between the electrons and a smaller attraction to the core. This shift in ion size changes the effective energy distance between electronic transitions, resulting in different absorption and emission properties. Transitions between the 4f and 5d orbitals typically require energies associated with UV for trivalent lanthanides. The divalent lanthanide, however, has a much lower energy difference between the 4f and 5d orbitals. Unlike  $4f\rightarrow 4f$  transitions, the  $4f\rightarrow 5d$  transition is allowed according to parity selection rules which results in a much stronger absorption compared to 4f->4f transitions. A 4f->5d transition causes a displacement in the atomic arrangement which leads to broad absorption and emission properties. For more details the reader is encouraged to look at configurational coordinate diagrams. What's more is that unlike the 4f orbitals, 5d orbitals are not shielded by other orbitals and are thereby subjected to crystal field splitting due to the local symmetry around the ion. The crystal field splitting of the 5d orbitals results in further broadening of the absorption properties. In the case of Sm<sup>2+</sup> the strong and broad 4f<sup>6</sup>  $\rightarrow$  4f<sup>5</sup>5d transitions are typically in the visible part of the spectrum, which is what makes Sm<sup>2+</sup> a good candidate to fulfill the criteria of an efficient LSC. In Fig. 3.1 a typical excitation and emission spectrum is shown of homemade sputtered samples consisting of Sm2+ and Sm3+ in a silicon aluminate host (SiAlO). A number of features (i-v) can be seen in these spectra and can be explained as follows:

- (i) Charge transfer transition of Sm<sup>3+</sup> where an electron from the valence band (oxygen 2p orbitals) is transferred to the Sm<sup>2+</sup> ground state
- (ii) Excitation from the Sm<sup>3+</sup> ground state to an excited 4f state (4f<sup>5</sup> $\rightarrow$ 4f<sup>5\*</sup>)
- (iii) Excitation from the Sm<sup>2+</sup> ground state to the  $4f^55d^1$  Sm<sup>2+</sup> state  $(4f^6 \rightarrow 4f^55d^1)$
- (iv) Emission from the excited Sm<sup>3+</sup> state ( ${}^4G_{5/2}$ ) to lower lying states including the ground state ( ${}^6H_1$  manifold) ( ${}^4F_{5/2}$ )
- (v) Emission from the excited  $4f^6$  Sm<sup>2+</sup> state ( $^5D_0$ ) to lower lying states including the ground state ( $^7F_1$  manifold) ( $4f^55d^1 \rightarrow 4f^6$ )

It should be noted that for Sm<sup>2+</sup> it is possible to observe  $4f^6 \rightarrow 4f^6$  excitation, should the lowest lying  $4f^5d^1$  state lie above the  $4f^6$  excited states.  $4f^55d^1 \rightarrow 4f^6$  emission can also be observed if there were sufficient relaxation of the ion take place after excitation. This

would place the  $4f^55d^1$  excited state below the emissive  $4f^6$  state ( $^5D_0$ ). These two transitions are not significantly observed in the samples presented. An energy diagram of these electronic states and transitions were estimated following the work of Dorenbos in **Fig. 3.2**. where vacuum is used as a reference energy [2]. The conduction band (CB), valence band (VB),  $Sm^{2+/3+}$  ground state and  $Sm^{2+}$  lowest lying  $4f^55d^1$  state positions are taken from literature values [3, 4]. For clarity, not every 4f energy level is presented in **Fig. 3.2**. The transitions labelled ii, iii and iv represent a range of  $4f^{5/6} \rightarrow 4f^{5/6}$  transitions rather than a single one. The available  $4f^n \rightarrow 4f^n$  transitions of each trivalent can be found in the well-known Dieke diagram. The excited 4f state from which emission takes place is  $^5D_0$  and  $^4G_{5/2}$  for  $Sm^{2+}$  and  $Sm^{3+}$  respectively. For divalent Sm, the electron configuration is the same of  $Eu^{3+}$  which can therefore be used as an estimation for the  $4f^6 \rightarrow 4f^6$  transitions of  $Sm^{2+}$  shown in **Fig. 3.2**.

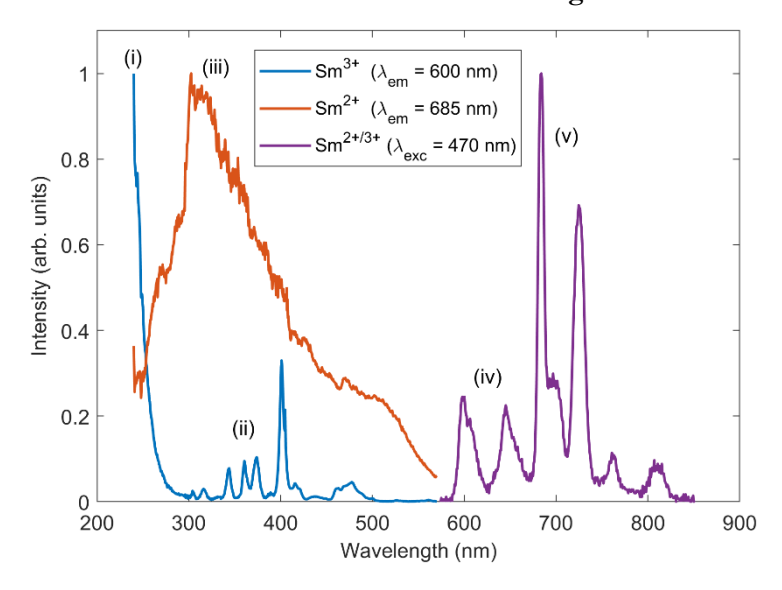


**Fig. 3.1.** Typical excitation and emission spectra of  $Sm^{2+/3+}$  of one of our reactively sputtered thin films. The electronic transitions labelled i, ii, iii, iv and v are represented by arrows in the energy diagram presented in **Fig. 3.2**.

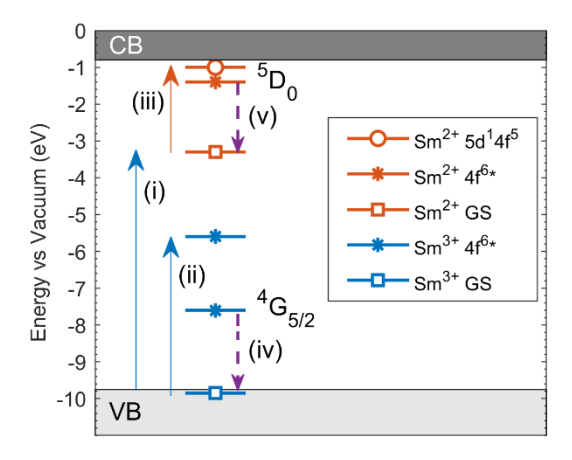


Fig. 3.2. Estimated energy diagram for SiO<sub>2</sub>:Sm. The labels (i-v) represent the features found in the excitation and emission spectra presented in Fig. 3.1.

#### SiAlO:Sm<sup>2+</sup>

In 2020, the same year I started my PhD research, there was a publication that came from the lab of the luminescent materials group at TU Delft regarding the possibility of using silicon aluminate glass doped with Sm (SiAlO:Sm²+) thin film for LSC applications [5]. These thin film LSCs displayed the broad excitation properties related to 4f→5d transitions of Sm²+ and showed the favourable emission around 710 nm as shown earlier. In **Fig 3.3**b a UV flashlight is used to excite the Sm²+ ions in such a thin film. The Sm²+ ions emit in the red which is concentrated at the edge of the sample. However, the thin films appear transparent as can be seen in **Fig 3.3**a, which indicates that the absorption is too weak for a succesfull application.

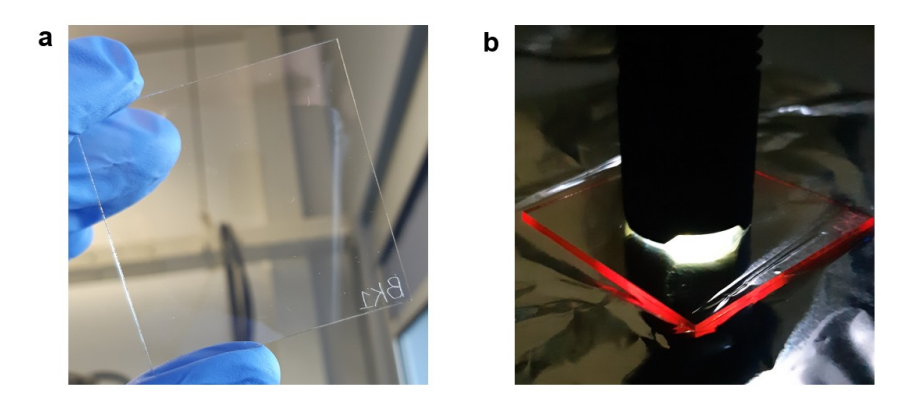


Fig 3.3. a) Photo of a SiAlO:Sm thin film on a quartz substrate. b) The same sample depicted in (a) under illumination of a ultraviolet and visible flashlight

It was found through x-ray photo-electron spectroscopy (XPS) that a significant percentage of the Sm in the SiAlO matrix was trivalent, rather than divalent. In an unpublished study conducted by a master student at the TU Delft the highest percentage of Sm<sup>2+</sup> of all Sm ions was found to be 23%. It has been shown that the ratio between Si and Al in the glass host can greatly influence the Sm<sup>2+</sup> solubility in the SiAlO matrix [6-8]. The key results of these studies are that the incorporation of Al in SiO<sub>2</sub> prevents agglomeration of Sm and promotes the conversion of Sm<sup>3+</sup> into Sm<sup>2+</sup>. It is evident from these studies that Sm<sup>2+</sup> prefers a local symmetry that is surrounded by Al-O polyhedral, particularly AlO<sub>6</sub>. Post heat treatments of the samples in a reducing atmosphere also assist in the formation of Sm<sup>2+</sup> in silicate based hosts [8]. The aforementioned study done within the group at TU Delft had already optimized the performance of the SiAlO:Sm<sup>2+</sup> thin film by tuning the Si-Al ratio. The question that came to mind is whether another element, not Al, could yield higher Sm<sup>2+</sup> content in silica based glasses.

#### **Boron Co-doping Strategy**

Similar to the role of Al in reducing Sm in silicate glasses and increasing its solubility, it has been shown that an increased boron content in sodium borate glasses can promote the reduction of Eu [9]. The reason given is that BO<sub>4</sub> units are replaced by BO<sub>3</sub> units in the glass matrix which depolymerize the matrix providing a larger, more favourable site for Eu<sup>2+</sup>. Another explanation for the reduction of Eu lies in the decrease of the so-called optical basicity [10]. The optical basicity of a glass is often described as the 'electron donor power' of the constituent oxygen atoms [11]. The phrase 'electron donor power' can be confusing as it might suggest that a glass with a high optical basicity is more likely to reduce the valence of cations within the glass matrix. When in fact the opposite is true. I believe a better phrase to describe optical basicity would be 'electron availability'. Glasses with lower optical basicity tend to stabilize cations in lower oxidation states because they have less electron availability to neutralize (or 'charge compensate') the higher positive charges of ions in higher oxidation states. These studies formulated one objective of the study which is to improve the solubility of Sm<sup>2+</sup> in the SiAlO host by incorporating B in the glass host.

Moving away from amorphous glass materials, another interesting material to host divalent samarium are strontium borates (SrBO) which are also considered for LSC applications [12, 13]. Strontium provides a suitable site for Sm to replace, both in terms of valence (2+) and ionic radius. It has been shown that co-doping strontium borate with Mg can further improve the reduction of Sm<sup>3+</sup> in strontium borates [14]. To

successfully incorporate divalent rare earth's in solid state compounds, Pei et al proposed four conditions to be met in order to do so [15]:

- i) no oxidizing ions like Cr<sup>4+</sup> are present in the host compounds
- ii) the dopant rare-earth ion replaces a divalent cation in the host
- iii) the substituted cation has a similar radius to the divalent rare earth ion
- iv) the host compound has an appropriate structure, based upon tetrahedral anion groups (BO<sub>4</sub>, SO<sub>4</sub>, PO<sub>4</sub> or AlO<sub>4</sub>).

The last condition is somewhat contradicting with what is mentioned above where AlO<sub>6</sub> and BO<sub>3</sub> groups were suggested to be responsible for hosting divalent samarium/europium. One study shows, using Raman spectroscopy, a correlation between the reduction of Tb and the concentration of BO<sub>3</sub> groups, rather than BO<sub>4</sub> groups [16]. In the case of Pei they found that Sr<sub>3</sub>B<sub>2</sub>O<sub>6</sub>, Sr<sub>2</sub>B<sub>2</sub>O<sub>5</sub> and SrB<sub>2</sub>O<sub>4</sub>, which consists of BO<sub>4</sub> groups rather than BO<sub>3</sub> groups were unable to host Sm<sup>2+</sup>. Whereas, SrB<sub>4</sub>O<sub>7</sub>, which is built on BO<sub>3</sub> groups, is suitable to host Sm<sup>2+</sup>. A recent study in 2023 found that SrB<sub>6</sub>O<sub>10</sub> is a superior host for housing Sm<sup>2+</sup> than SrB<sub>4</sub>O<sub>7</sub> is [13, 17]. Strontium borate doped with rare earths remains a topic of research for solar energy applications to this day.

Taken together, these studies were the motivation to attempt to fabricate SiAlBO:Sm and SrBO:Sm based thin film LSCs with a focus on increasing Sm content in order to satisfy absorption requirements for thin film LSCs. Unique to this research is the fabrication method used: reactive magnetron sputtering, an already established industry practice. Previous studies primarily focused on solid state synthesis, crystal growth or sol-gel techniques [12, 13, 15, 17]. The approach of this research is twofold. First, incorporate boron into a silica (SiO), an alumina (AlO) and an aluminosilicates (SiAlO) type host and observe any changes in luminescence intensity from Sm³+ or Sm²+. A SiBO:Sm film with a compositional gradient (i.e. varying Si, B and Sm content as function of position on the film) is studied to determine a trend in Sm²+ intensity against Sm content on various positions (or compositions) of the film. Second, a sputtered strontium borate (SrBO) thin film doped with samarium is analysed and compared to previous studies. The suitability of these materials as sputtered thin film LSCs is the subject of the discussion.

# 3.2 Experimental Methods

The experimental methods used for this project are described in detail in chapter two of this thesis. For this reason they are only briefly discussed here. The thin films were synthesized on 5x5 cm quartz or Borofloat® substrates using reactive magnetron sputtering. Single sputter targets, Si, Al, B, Sm and Sr with a 2" diameter and 1/4"

thickness were purchased from Demaco. A compound target consisting of 90 % Si and 10 % Al (mass %) was used for SiAlO:Sm (B5). An AJA-Orion 5 sputter coater is used which can hold up to 4 targets. A pulsed D.C power supply is connected to the Si target whereas the others are connected to a RF power supply. Sputtering is done in a reactive atmosphere of Ar and O with a total flow of 15 sccm and at a pressure of 3 mTorr. To reduce the deposition rate of Sm a mask is installed above the target and the magnetic field strength is reduced. The working distance between the targets and substrate is roughly 10 cm. The sputtering conditions of the films can be seen in **Table 3.1**. All films were post annealed in a reducing atmosphere of N<sub>2</sub>/H<sub>2</sub> for 30 minutes at 600 °C. The sputter process of SiBO (B3) was repeated while the substrate was not rotating in order to achieve a compositional gradient. The large range in deposition time and deposition rates results in variations in the final thickness of the film. Therefor studies comparing absolute luminescent intensities are non-trivial and have been left out of this analysis. For experimental details on the instruments used for the characterization of the film, including the photoluminescence and optical properties, composition and crystallinity the reader is referred to Chapter 2 of this thesis and to the experimental methods sections in **Chapter 4** and **Chapter 5**.

**Table 3.1.** Sputter conditions for samples presented in this chapter. \*a copy is made of B3 where the substrate is not rotating creating a compositional gradient with Si, B, and Sm rich sides. \*\*a single SiAl (90:10, Si:Al) target was used.

ID	Composition	O <sub>2</sub> (sccm)	Sr/Si/Al/B/Sm (W)	Dep. Time (s)
<b>B</b> 1	SiO:Sm	1.5	0/110/0/0/20	8200
B2	AlBO:Sm	1.5	0/0/18/100/15	20000
B3*	SiBO:Sm	1.5	0/135/0/100/15	12000
<b>B</b> 4	SiAlBO:Sm	1.5	0/135/45/100/15	12000
B5**	SiAlO:Sm	0.9	0/120/120/0/15	10500
B6	SrBO:Sm	1.1	25/0/0/150/20	40000

#### 3.3 Results and Discussion

The transmission spectra of the SiBO (B3) and SrBO (B6) are shown in **Fig. 3.4**. The transmission spectra of SiO(B1) and AlBO (B2) resembled that of the SiBO (B3) sample while the SiAlBO (B4) and SiAlO (B5) resembled that of the SrBO (B6) sample. For this reason the transmission spectra of B1, B2, B4 and B5 are omitted from **Fig. 3.4**. The absorption of SrBO (B6) below 300 nm is due to the borosilicate substrate used. SiBO (B3) was deposited on a quartz substrate and therefor has no absorption below 300 nm. All samples do not show absorption related to Sm<sup>2+</sup>. The thin film interference

pattern observed for SrBO (B6) can be fitted using the Swanepoel method to retrieve the thickness and refractive index of the thin film [18]. The same has been done for SiAlBO (B4) and SiAlO (B5). For SiBO (B3) there is no clear interference pattern observed, which is likely due to a high similarity between the refractive index of the substrate (1.46) and the thin film. To retrieve the thickness of SiBO (B3), SiO (B1) and AlBO (B3) a DekTak profilometer is used. The refractive index of B1-B3 is assumed to be 1.45. The results are summarized in **Table 3.2**.

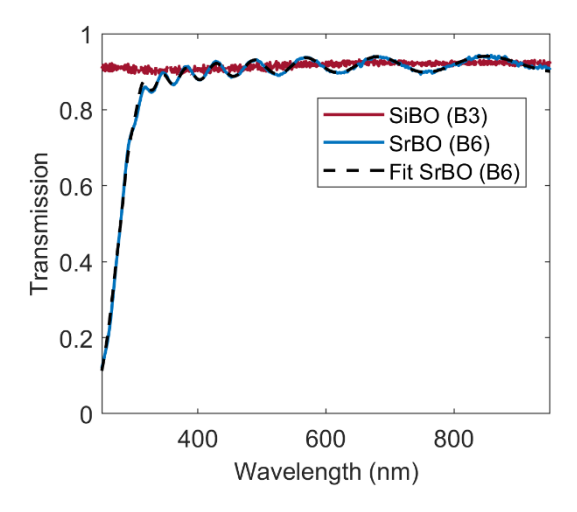


Fig. 3.4. Transmission spectra of the SiBO (B3) and SrBO (B6) samples. The thin film interference pattern of SrBO (B6) is fitted using the Swanepoel method and shown by the dashed line.

The cation atomic content for each thin film is shown in **Table 3.2**. The anion content (O), is difficult to determine due to a contribution of the silicate based substrate and due to general difficulties in quantifying O content using EDS. The Sm content varies between 0.2 and 1.5 %, except for AlBO (B2), where the Sm content is significantly higher at 3.4 % due to difficulties with the relatively low deposition rate of B compared to that of the dopant Sm. SiAlO (B5) used a compound Si-Al sputter target with 90 % Si and 10 % Al (mass %), however the resulting film had roughly 60 % Si and 40 % Al. This difference in final film stoichiometry vs target stoichiometry has not been investigated.

**Table 3.2** Cation atomic percentages of samples measured through EDS. Refractive index (n) and thickness d (nm) are found by fitting the transmission spectra like the one presented in **Fig. 3.4**.

ID	Sr %	Si %	A1 %	B %	Sm %	n	d (nm)
<b>B</b> 1	0	98.5	0	0	1.5	*1.45	890
B2	0	0	5.4	91.2	3.4	*1.45	550
В3	0	79.6	0	20.2	0.2	*1.45	1650
B4	0	57.3	26.4	14.6	0.2	1.51	1830
B5	0	60.3	39.3	0	0.4	1.56	1130
B6	24.6	0	0	74.9	0.5	1.59	1070

The normalized Sm emission ( $\lambda_{\text{exc}} = 400 \text{ nm}$ ) of B1 to B5 are shown in **Fig. 3.5**. Samples SiO (B1) and AlBO (B2) show only narrow Sm3+ emission at roughly 550, 600, 650 nm and a broader emission at 700 nm, all associated with the  ${}^4G_{5/2} \rightarrow {}^6H_{5/2}$ ,  ${}^6H_{7/2}$ ,  ${}^6H_{9/2}$ , <sup>6</sup>H<sub>11/2</sub> transitions of Sm<sup>3+</sup>, respectively. Note that the highest peak is around 650 nm for SiO (B1), whereas it is at 600 nm for AlBO (B2), indicating a change in local environment for Sm3+ when going from a silicate to an aluminum borate and that both host lattices provide a more stable environment for the 3+ valence state of Sm. SiBO (B3) shows narrow characteristic Sm<sup>2+</sup> emission at mainly 685 and 730 nm, associated with the  ${}^5D_0 \rightarrow {}^7F_0$ ,  ${}^7F_2$  transitions respectively. A weak contribution of Sm<sup>3+</sup> emission is still observed in SiBO (B3). Samples SiAlBO (B4) and SiAlO (B5) show no Sm3+ emission when excited at 400 nm. B3-B5 show a broad band situated underneath the sharp peaks, likely associated with a 4f<sup>5</sup>5d<sup>1</sup>  $\rightarrow$  4f<sup>6</sup> transition of Sm<sup>2+</sup>. These results show that B in SiBO has a similar role as Al in SiAlO: enhancing the formation of Sm<sup>2+</sup> over Sm<sup>3+</sup>. To confirm the results of previous studies that relate the increase in Sm<sup>2+</sup> intensity to an increase in BO3 units could be accomplished by Raman spectroscopy, but this has not been done in this work. The incorporation of boron oxide will, by definition, reduce the optical basicity of alumina and silica based glasses. The key result of this work presented thus far is showing that it is possible to fabricate luminescent thin films of borosilicate and aluminoborosilicate doped with Sm<sup>2+</sup> via reactive magnetron sputtering and that previous studies have been corroborated that B can promote the formation of Sm<sup>2+</sup> inside the glass network.

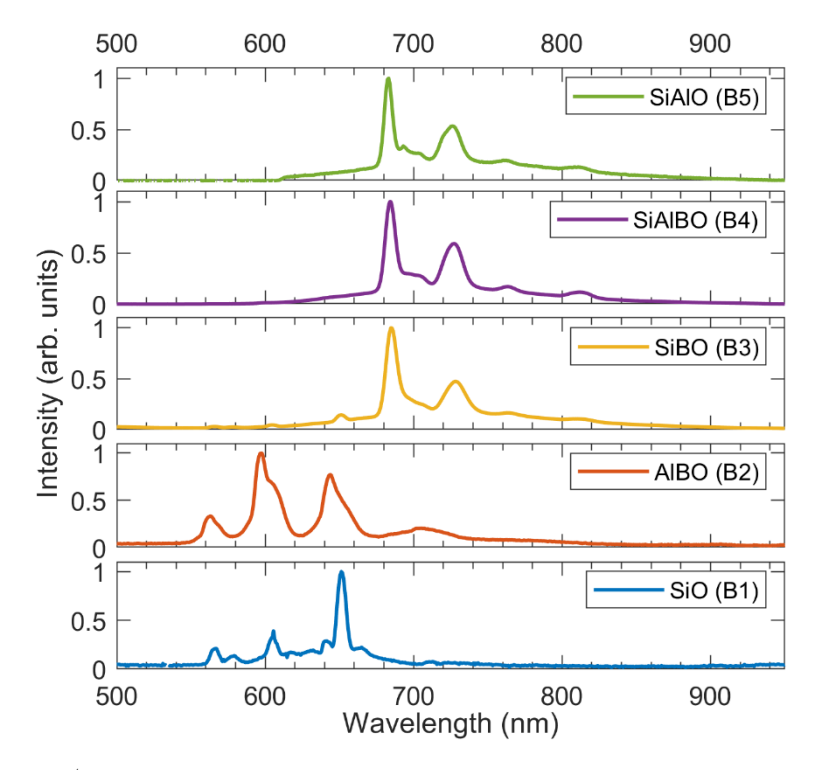


**Fig. 3.5.**  $Sm^{2+/3+}$  emission ( $\lambda_{exc}$  = 400 nm) of samples B1 to B5. Emission below and above 675 nm are related to  $Sm^{3+}$  and  $Sm^{2+}$  respectively. At 700 nm there is broad emission by both  $Sm^{2+}$  and  $Sm^{3+}$ .

#### SiBO (with a compositional gradient)

A copy of the SiBO (B3\*) sample, but with a compositional gradient, is presented in this section. During deposition the substrate was simply not rotating to achieve said compositional gradient. In Fig. 3.6b the emission ( $\lambda_{\rm exc} = 400$  nm) at three locations on the SiBO:Sm (B3\*) film are shown. The positions are chosen in a line across the film (left to right), where the Si:B ratio (found by positional EDS measurements) is constant at roughly 4:1 (the same as B3), as can be seen in Fig. 3.6a. However, the Sm content varies from 0.01 to 0.14 (at. %) across this line. Increasing the Sm content from 0.01 to 0.07 (at.%) results in a decrease in peak emission by 60%. From 0.01 to 0.14 results in less than 10% of the original peak emission intensity. Position dependent transmission spectra, taken at the same positions as the emission measurements, are shown in Fig. 3.6c. The transmission spectra are nearly identical, and the detector lacks the dynamic range to show potential changes in absorption properties. The increase in Sm content appears to increase the concentration quenching of Sm<sup>2+</sup> more strongly than the potential increase in absorption. This effect may be enhanced due to a larger fraction of the Sm ions being present in the Sm<sup>3+</sup> valence state and thereby no longer contributing to the absorption. These results indicate that increasing Sm content further will not result in sufficient absorption for the LSC application especially since concentration quenching of Sm<sup>2+</sup> is already very efficient at 0.14%.

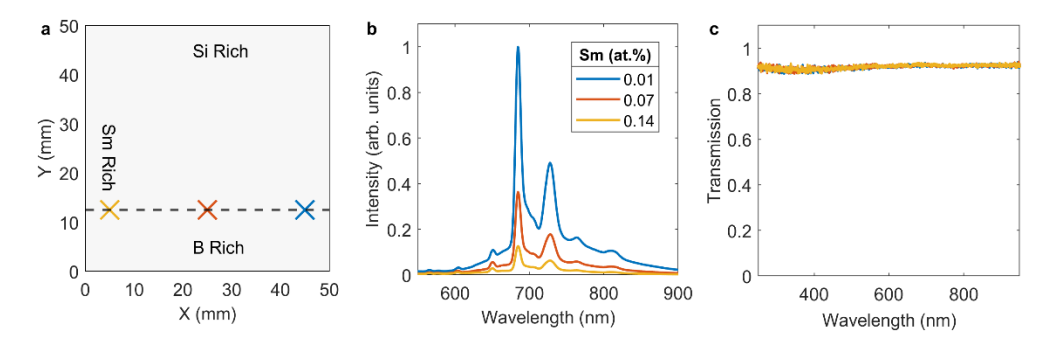


**Fig. 3.6. a)** Schematic of the thin film with compositional gradient where the highest Si, B and Sm content is found at the top, bottom and left side respectively. The dashed line represents a constant Si:B ratio of roughly 4:1. The colored markers represent the positions at which emission measurements are performed shown in (b). **b)** Sm<sup>2+</sup> intensity ( $\lambda_{exc} = 400$  nm) with various Sm content measured at colored markers in (a). **c).** Transmission measurements at the position indicated in (a). The three measurements overlap each other indicating no change in transmission or absorption properties.

#### SiAlO:Sm versus SiAlBO:Sm

In **Fig. 3.7** a photograph is shown of the most optimized SiAlO:Sm (B5, left) and SiAlBO:Sm (B4, right) samples when illuminated with UV light. B4 has been cut into 4 pieces for other experiments and just one of the four pieces is shown. At first glance the smaller SiAlBO:Sm (B4) sample appears to have a more intense red Sm<sup>2+</sup> emission concentrated at the edge than the larger SiAlO:Sm (B5) sample. However, due to the size difference a fair comparison cannot be made as LSCs are known to reduce in efficiency with increasing size due to self-absorption and scattering losses in the waveguide. What's more is that the SiAlBO:Sm (B4) thin film has a thickness of 1830 nm whereas 1130 nm is the thickness of the SiAlO:Sm (B5) thin film. Though **Fig. 3.7** is a nice picture of the LSC effect. The low Sm content of 0.2%, as explained above and shown by the transmission measurements presented in **Fig. 3.6**c, will certainly not provide adequate absorption for LSC applications.



**Fig. 3.7.** Photograph of sample B5 (SiAlO:Sm, left) and B4 (SiAlBO:Sm, right) under an UV light source. B4 has been cut in smaller pieces for another study. Luminescent contaminations, shown as white dots, originate from the lamp stand and not from the samples (note to self: clean set-ups every now and then).

#### SrBO:Sm

We now move on to the strontium borate thin film doped with samarium using reactive magnetron sputtering. No literature was found on fabricating such thin films using sputtering. The ratio between Sr and B for the film is 1:3 as shown in **Table 3.2**. As stated before, the refractive index (n) and thickness d (nm) are found by fitting the transmission spectrum in Fig. 3.4 with the Swanepoel method. Despite that the power on the B target (150 W) was much larger than on the Sr target (25 W) the Sr:B ratio was not the optimal 4:1 (SrB<sub>4</sub>O<sub>7</sub>) or 6:1 (SrB<sub>6</sub>O<sub>10</sub>) for Sm<sup>2+</sup> luminescence found in previous studies that used solid-state reaction synthesis [12, 14]. The emission spectrum ( $\lambda_{\rm exc}$  = 400 nm), presented in Fig. 3.8a, shows transitions associated with both Sm<sup>3+</sup>  $({}^4G_{5/2} \rightarrow {}^6H_I)$  and Sm<sup>2+</sup> ( ${}^5D_0 \rightarrow {}^7F_I$ ). The excitation spectrum when monitoring the Sm<sup>2+</sup> emission at 685 nm shows a similar shape to that of the SiAlO:Sm (B5) sample, indicating that Sm<sup>2+</sup> occupies a similar site and that it does not replace Sr<sup>2+</sup> ions as one would expect if the film contains the SrB<sub>4</sub>O<sub>7</sub> crystalline phases. The main feature is a broad excitation band associated with the 4f<sup>6</sup>→4f<sup>5</sup>5d<sup>1</sup> transitions. This excitation spectrum is different than elsewhere reported excitation spectrum of Sm<sup>2+</sup> in SrB<sub>4</sub>O<sub>7</sub>, where the splitting of the 5d orbital is clearly distinct [15]. These two bands are associated with a lower eg and higher t2g band, explained by the Sm occupation of the capped cubic Sr site [17]. This suggests that our Sm does not occupy a Sr site in our sample as explained above. X-ray diffraction measurements were systematically performed after a series of anneal processes with increasing temperature and is shown in Fig. 3.8b. The only phase identified is that of B<sub>2</sub>O<sub>3</sub> which starts to form around 1050 °C [19]. These results confirm the amorphous nature of the SrBO:Sm film. The ratio of Sr:B (1:3) in our sample should be further optimized via tweaking of the sputter parameters to promote the formation of SrB<sub>4</sub>O<sub>7</sub>. It has been shown in previous studies that a non-crystalline SrB<sub>4</sub>O<sub>7</sub> is far less efficient at room temperature than its crystalline counterpart [20].

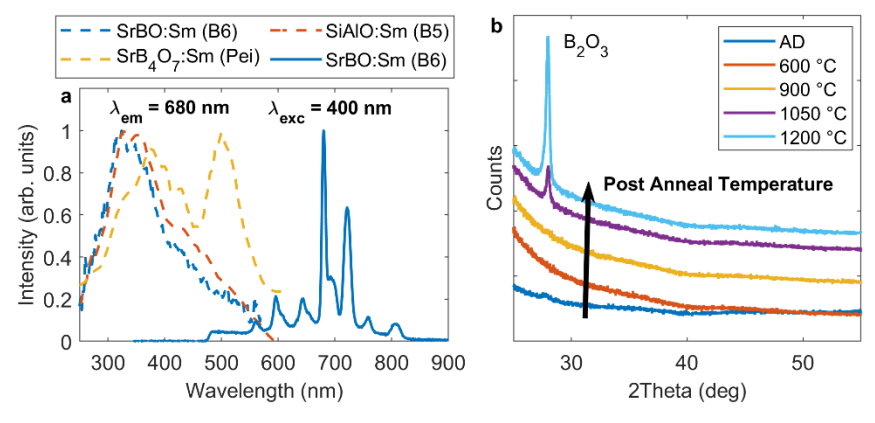


**Fig. 3.8. a)** Excitation (dashed) and emission spectra of SrBO:Sm (B6). Two additional excitation spectra are shown for comparison purposes: SiAlO:Sm (B5) and from literature [15]. **b)** X-ray diffractograms of B6 as function of temperature, where AD stands for as deposited.

## 3.4 Summary and Concluding Remarks

In this work we have synthesized a series of amorphous silica and borate based luminescent thin films through reactive magnetron sputtering. We have corroborated previous work that the formation of Sm<sup>2+</sup> is promoted by the incorporation of Al or B in silicate based glasses. The most intense Sm<sup>2+</sup> luminescence was found with the lowest Sm content of 0.01 % in a SiAlBO host. These low Sm content do not provide adequate absorption in thin films for LSC applications. A strontium borate host was also sputtered, however the sputter settings were not optimized to acquire the desired SrB<sub>4</sub>O<sub>7</sub> or SrB<sub>6</sub>O<sub>10</sub> composition due to practical problems concerning the low sputter rate of the B target. Instead, a 1:3 ratio of Sr:B was studied. The strontium borate films appear to be amorphous and Sm takes on a similar site in strontium borate as it does in aluminium silicate. To further examine strontium borate thin films doped with Sm requires overcoming challenges in the synthesis of the sputtered thin films. Though strontium borate doped with Sm has been considered for LSC applications, the path to implement them through sputtering thin films appears to be difficult.

## 3.5 References

- [1] E. Nakazawa, "The lowest 4f-to-5d and charge-transfer transitions of rare earth ions in YPO4 hosts," *Journal of Luminescence*, vol. 100, no. 1, pp. 89-96, 2002/12/01/ 2002, doi: https://doi.org/10.1016/S0022-2313(02)00429-5.
- [2] P. Dorenbos, "Systematic behaviour in trivalent lanthanide charge transfer energies," *Journal of Physics: Condensed Matter*, vol. 15, no. 49, p. 8417, 2003.
- [3] N. Fujimura, A. Ohta, K. Makihara, and S. Miyazaki, "Evaluation of valence band top and electron affinity of SiO2 and Si-based semiconductors using X-ray photoelectron spectroscopy," [apanese Journal of Applied Physics, vol. 55, no. 8S2, p. 08PC06, 2016.
- [4] P. Dorenbos, "Modeling the chemical shift of lanthanide 4 f electron binding energies," *Physical Review B—Condensed Matter and Materials Physics*, vol. 85, no. 16, p. 165107, 2012.
- [5] D. de Vries, S. van Overbeek, E. P. Merkx, and E. van der Kolk, "Sm2+-doped SiAlO sputter deposited coatings for self-absorption and scatter-free luminescent solar concentrator applications," *Journal of Luminescence*, vol. 225, p. 117321, 2020.
- [6] M. Nogami, T. Hagiwara, G. Kawamura, E.-S. Ghaith, and T. Hayakawa, "Redox equilibrium of samarium ions doped in Al2O3–SiO2 glasses," *Journal of luminescence*, vol. 124, no. 2, pp. 291-296, 2007.
- [7] R. Morimo et al., "Enhancement of fluorescent intensity of a SiO2: Sm glass by Al codoping and local structure around Sm by an EXAFS study," Journal of The Electrochemical Society, vol. 137, no. 7, p. 2340, 1990.
- [8] J. Jin, S. Sakida, T. Yoko, and M. Nogami, "The local structure of Sm-doped aluminosilicate glasses prepared by sol–gel method," *Journal of non-crystalline solids*, vol. 262, no. 1-3, pp. 183-190, 2000.
- [9] Q. Jiao, X. Yu, X. Xu, D. Zhou, and J. Qiu, "Phenomenon of Eu3+ self-reduction induced by B2O3 configuration structure in sodiumborate glasses," *Journal of Applied Physics*, vol. 114, no. 4, 2013, doi: 10.1063/1.4816445.
- [10] S. Liu et al., "Reduction of Eu3+ to Eu2+ in aluminoborosilicate glasses prepared in air," *Journal of the American Ceramic Society*, vol. 91, no. 8, pp. 2740-2742, 2008.
- [11] J. A. Duffy, "A review of optical basicity and its applications to oxidic systems," *Geochimica et Cosmochimica Acta*, vol. 57, no. 16, pp. 3961-3970, 1993.
- [12] D. K. de Boer et al., "Progress in phosphors and filters for luminescent solar concentrators," Optics express, vol. 20, no. 103, pp. A395-A405, 2012.
- [13] L. Erasmus *et al.*, "Making Eu2+-and Sm2+-Doped Borates Fit for Solar Energy Applications," *ACS Photonics*, vol. 10, no. 3, pp. 609-622, 2023.
- [14] G. Odendaal, L. Erasmus, R. Kroon, and H. Swart, "Reduction methods for Sm3+ to Sm2+ in strontium borates for solar energy applications," *Physica B: Condensed Matter*, vol. 669, p. 415319, 2023.
- [15] Z. Pei, Q. Su, and J. Zhang, "The valence change from RE3+ to RE2+ (RE Eu, Sm, Yb) in SrB4O7: RE prepared in air and the spectral properties of RE2+," *Journal of alloys and compounds*, vol. 198, no. 1-2, pp. 51-53, 1993.
- [16] H. Yin, Y. Gao, H. Guo, C. Wang, and C. Yang, "Effect of B2O3 content and microstructure on Verdet constant of Tb2O3-doped GBSG magneto-optical glass," *The Journal of Physical Chemistry C*, vol. 122, no. 29, pp. 16894-16900, 2018.
- [17] H. Liang, Q. Zeng, T. Hu, S. Wang, and Q. Su, "Local structure and valences of samarium in SrB4O7: Sm and SrB6O10: Sm prepared in air," *Solid state sciences,* vol. 5, no. 3, pp. 465-467, 2003.
- [18] R. Swanepoel, "Determination of the thickness and optical constants of amorphous silicon," Journal of Physics E: Scientific Instruments, vol. 16, no. 12, p. 1214, 1983/12/01 1983, doi: 10.1088/0022-3735/16/12/023.
- [19] B. H. Tran, K. Tieu, S. Wan, H. Zhu, S. Cui, and L. Wang, "Understanding the tribological impacts of alkali element on lubrication of binary borate melt," RSC advances, vol. 8, no. 51, pp. 28847-28860, 2018.

[20] J. Verwey, G. Dirksen, and G. Blasse, "The luminescence of divalent and trivalent rare earth ions in the crystalline and glass modifications of SrB4O7," *Journal of Physics and Chemistry of Solids*, vol. 53, no. 3, pp. 367-375, 1992.

# 4 Cr<sup>3+</sup> and Nd<sup>3+</sup> in the Al<sub>2</sub>O<sub>3</sub>-Y<sub>2</sub>O<sub>3</sub> System

#### 4.1 Abstract

The characterization of a wide range of luminescent thin films can be a long and tedious endeavor. With reactive combinatorial sputtering of multiple metal targets, it is possible to fabricate thin films with a gradient in composition simply by not rotating the substrate. In this work, combinatorically sputtered thin films of Cr3+ and Nd3+ doped in the Al<sub>2</sub>O<sub>3</sub>-Y<sub>2</sub>O<sub>3</sub> system (YAlO) are studied for application in thin film-based luminescent solar concentrators (TFLSCs). Contrary to mm's thick plate type LSCs, TFLSCs of just several 100 nm thickness require much higher Cr3+ concentration to achieve 40% absorption which can enable several 10's of W/m<sup>2</sup> LSC power efficiencies. Our transmission measurements on a Cr<sub>2</sub>O<sub>3</sub> film with a thickness gradient result in an absorption cross section at 460 nm of  $1.3 \pm 0.7 \times 10^{-19}$  cm<sup>2</sup> showing that the TFLSC absorption requirement can be fulfilled provided that the Cr<sup>3+</sup> concentration is in the order of 10<sup>22</sup> ions/cm<sup>3</sup>. The Y:Al ratio of the YAlO host in our films ranged between 0.5 and 3.5, thereby including the monoclinic (Y<sub>4</sub>Al<sub>2</sub>O<sub>9</sub>), perovskite (YAlO<sub>3</sub>) and garnet (Y<sub>3</sub>Al<sub>5</sub>O<sub>12</sub>) stoichiometry's on a single film. Position dependent XRD, EDX, excitation, emission and lifetime measurements of Cr3+ and Nd3+ show that the unique gradient film sputtering method is able to characterize thin films as a function of host composition and doping concentration. Energy transfer between Cr3+ and Nd3+ in codoped YAIO films is concluded from Cr3+ excitation bands observed while monitoring Nd<sup>3+</sup> emission and from the matching of the rise-time of Nd<sup>3+</sup> 1340 nm emission (<sup>4</sup>F<sub>3/2</sub>  $\rightarrow$  <sup>4</sup>I<sub>11/2</sub>) and the decay time of Cr<sup>3+</sup> 840 nm emission (<sup>4</sup>T<sub>2</sub>  $\rightarrow$  <sup>4</sup>A<sub>2</sub>). Nd<sup>3+</sup> lifetime systematically decreases from 0.24 to 0.05 ms with increasing Cr<sup>3+</sup> concentration in  $Y_3Al_{5-x}Cr_xO_{12}$ :Nd (0.05 < x < 2). The constraints of heavily doped  $Cr^{3+}$  thin films for enabling adequate absorption and energy transfer to Nd3+ in TFLSC applications are the subjects of the discussion.

The content of this chapter is based on the publication:

**Derksen, M.**, Bosco, G., Muller, T. and van der Kolk, E., 2024. Photoluminescence of combinatorically sputtered Al<sub>2</sub>O<sub>3</sub>–Y<sub>2</sub>O<sub>3</sub> thin films with a Cr<sup>3+</sup> and Nd<sup>3+</sup> co-doping concentration gradient. *Journal of Luminescence*, 269, p.120503.

## 4.2 Introduction:

Conventional luminescent solar concentrators (LSCs) are in the form of a single glass or polymer plate of several millimetres thick in which the luminescent species are introduced directly [1,2]. The plate acts as a sunlight absorbing waveguide in which generated luminescence light is guided to mounted solar cells at the edge. Thin film based luminescent solar concentrators (TFLSCs) fabricated via (reactive) magnetron sputtering are an attractive alternative design due to the compatibility with current glass industry large-scale coating capabilities. In general to achieve an LSC power conversion efficiency of 5-10% (i.e. several 10's of W/m2) with Si-solar cells there are three main criteria that must be met [3]:

- i. Broadband UV to VIS absorption of around 40% at all wavelengths
- ii. Minimum reabsorption losses due to overlap of absorption and emission.
- iii. Near-unity photoluminescent quantum yield (PLQY) of the emission that is efficiently convertible to power by silicon solar cells.

Nd<sup>3+</sup> satisfies the last two criteria, but not the first. The narrow, weak, forbidden 4f-4f transitions of the rare-earths do not provide adequate absorption. To accommodate for this, a strong and broad absorbing sensitizer can be used such as Cr<sup>3+</sup>. The combination of Cr<sup>3+</sup> and Nd<sup>3+</sup> in glass has been considered for LSC applications in the conventional bulk plate configuration in the 1980s. [4, 5].

The Cr<sup>3+</sup> concentration in these works was < 1 mol.%, which would be too low in a thin film of several hundred nanometers considering condition (i). The absorption of a material can be calculated using equation 4.1, known as the Lambert-Beer law:

$$A = 1 - e^{-\alpha d} \tag{4.1}$$

Where a is the absorption coefficient (cm<sup>-1</sup>) and d the film thickness (cm). It can be shown using the Lambert-Beer law, that the absorption coefficient of the thin film must be roughly 5000 cm<sup>-1</sup> in order to achieve 40% internal absorption (excluding reflection or scattering losses) in a thin film with an industrial compatible thickness of 1  $\mu$ m. a is simply the product of the concentration C of absorbing ions (cm<sup>-3</sup>) and the absorption cross section  $\sigma$  (cm<sup>2</sup>). Using Cr doped inside Al<sub>2</sub>O<sub>3</sub>, commonly known as ruby, as an example, we can find the necessary Cr<sup>3+</sup> content to absorb approximately 40% within a 1  $\mu$ m thin film. Because  $\sigma$  of Cr<sup>3+</sup> at 430 nm in Al<sub>2</sub>O<sub>3</sub> is  $1.1 \times 10^{-19}$  cm<sup>2</sup> [6], C must be around  $4.5 \times 10^{22}$  cm<sup>-3</sup>, which is close to C of Al in Al<sub>2</sub>O<sub>3</sub> ( $4.7 \times 10^{22}$  cm<sup>-3</sup>). This indicates that nearly all Al atoms must be replaced with Cr. This simple calculation shows that in order for TFLSCs to be efficient they must work with high concentrations of relatively strong absorbing species. Part of this work demonstrates a simple method to find the absorption cross section of Cr<sup>3+</sup> using a single Cr<sub>2</sub>O<sub>3</sub> thin film with varying thickness together with the Lambert-Beer law.

Although Al<sub>2</sub>O<sub>3</sub> can accommodate a high concentration Cr<sup>3+</sup> at the Al<sup>3+</sup> sites, there is no available site for the much larger Nd<sup>3+</sup> ion. Yttrium aluminate (Y<sub>2</sub>O<sub>3</sub>-Al<sub>2</sub>O<sub>3</sub>) provides a suitable site for both Cr3+ and Nd3+ and has been studied for numerous applications such as solid-state lasers, solar pumped lasers, luminescent thermometers and more [7-9]. Yttrium aluminate exists in three phases: monoclinic (Y<sub>4</sub>Al<sub>2</sub>O<sub>9</sub> or YAM), perovskite (YAlO<sub>3</sub> or YAP) and garnet (Y<sub>3</sub>Al<sub>5</sub>O<sub>12</sub> or YAG). The energy transfer between Cr<sup>3+</sup> and Nd<sup>3+</sup> has extensively been studied for YAG and YAP crystals with reported energy transfer efficiencies of 48 and 67% respectively [10-12]. The probability of energy transfer from Cr<sup>3+</sup> was reported to be higher than that of non-radiative transitions of Cr3+, indicating that the fluorescent quantum efficiency of Cr3+ is not a limiting factor in the maximum energy transfer efficiency [4, 13]. Studies of Cr<sup>3+</sup> luminescence as function of concentration in single doped Al<sub>2</sub>O<sub>3</sub> has shown that Cr<sup>3+</sup> emission quenches at concentrations < 1 at.% due to the formation of Cr pairs that act as energy sinks [14, 15]. Single Cr<sup>3+</sup> ions can efficiently transfer energy amongst one another until it arrives at a Cr pair of which the decay rate is much faster, resulting in a quick dissipation of the energy. However it has been shown that incorporating another dopant such as Nd3+ allows to delay the Cr3+ concentration quenching effect [16]. Taken all together it is worth revisiting the Cr3+ and Nd3+ pair, in order to study their behavior in thin films with high concentration of Cr3+ which can provide adequate absorption and perhaps facilitate energy transfer to Nd3+.

Studying luminescent properties of Y<sub>2</sub>O<sub>3</sub>, YAM, YAP, YAG and Al<sub>2</sub>O<sub>3</sub> thin films doped with a range of Cr and Nd concentrations is a daunting task. However, using a unique approach that involves sputtering composition and doping concentration gradient thin films allows to analyze the behavior of the luminescence as a function of composition in a rapid fashion with a limited number of thin films. Our strategy is to use the gradient method to identify the optimum composition and subsequently when it is worthwhile to sputter homogeneous films with the same composition with other specialized sputtering systems. In this work we demonstrate the usefulness and validity of this gradient deposition technique as we explore the Al<sub>2</sub>O<sub>3</sub>-Y<sub>2</sub>O<sub>3</sub> system doped with Cr<sup>3+</sup> and Nd<sup>3+</sup>. Rather than to investigate various properties of each phase of the Al<sub>2</sub>O<sub>3</sub>-Y<sub>2</sub>O<sub>3</sub> system in detail, this work concerns itself with trends on single gradient films to underscore the power of the gradient method. We report on which phases of the Al<sub>2</sub>O<sub>3</sub>-Y<sub>2</sub>O<sub>3</sub> system are most likely to form in thin films. The energy transfer between Cr<sup>3+</sup> and Nd<sup>3+</sup> as a function of host and Cr<sup>3+</sup> concentration is qualitatively studied. We consider extreme cases where we replace 100% of Al with Cr in Cr<sub>2</sub>O<sub>3</sub> and YCrO<sub>3</sub> thin films. Position dependent transmission, emission and lifetime measurements are provided and related to local composition. Finally a discussion is made on this gradient film method and the limitations of highly doped Cr3+ thin films to accommodate the necessary absorption and to facilitate energy transfer to Nd3+ for LSC applications.

# 4.3 Experimental details

#### **Fabrication of Thin Films**

A total of 9 samples were deposited on a non-rotating 44x44x1 mm<sup>3</sup> quartz substrate (except for one sample, CR08, which was deposited on a 50x50x1 mm<sup>3</sup> quartz substrate) using an AJA ATC Orion 5 magnetron sputtering system. Sputtering was done in a mixed atmosphere of oxygen and argon from four 2" diameter and 1/4" thick targets: Y (99.9%), Al (99.999%), Cr (99.95%) and Nd (99.9%) (Demaco). Two pulsed direct current (DC) and two radio-frequency (RF) power supplies were used. Prior to deposition the sputter chamber is evacuated to a base pressure in the order of 0.1 mPa. The working pressure during sputtering is 0.4 Pa with a total gas flow of 15.0 sccm. The oxygen gas flow was chosen to be at the 'first critical point' identified through a typical hysteresis experiment [17]. The power on each target along with the O<sub>2</sub> flow was varied slightly between samples to acquire the desired compositions. Sputtering parameters used per sample can be seen in Table 4.1. The deposition time for CR01 to CR07 is 1500s and 2000s for CR08 and CR09, this deposition time was chosen to ensure a thickness below 1 micron. The working distance between target and substrate is 10 cm. The four targets are at right angles from one another, where each target is aligned so that the highest deposition rate is approximately at the edge of the substrate, in a sputter up configuration. In order to achieve doping concentrations between 1 and 10% of Cr a mask with holes is installed above the targets to reduce deposition rates by roughly 75 or 90%. For Nd, the magnetic strength of the magnetron is reduced to achieve doping concentration between 0.5 and 4%. For CR09 (Cr2O3), it has been shown that a substrate temperature of at least 500 °C is required to promote crystallinity which results in clear Cr<sup>3+</sup> absorption [18]. The substrate is heated at 600 °C during deposition for all films and is not rotated in order to obtain a compositional gradient. A schematic can be seen in Fig. 4.1. The gradient Al<sub>2</sub>O<sub>3</sub>-Y<sub>2</sub>O<sub>3</sub> films doped with Nd and Cr are given the name YAlO:Cr (x%) where x is the desired doping percentage of Cr in the center of the film, whereas the Nd concentration gradient was such that values never exceed 1 at.% anywhere in the film. After deposition, each sample was post annealed using a tube furnace at 1100 °C in an air atmosphere for three hours. Annealing at these temperatures proved to be crucial in obtaining Cr<sup>3+</sup> luminescence in thin films.

**Table 4.1.** Sample specific sputter parameters used for the fabrication of the 9 thin films reported in this work. Common parameters are mentioned in the text. Sample names indicate their estimated doping Cr concentration at each film's center. All samples are estimated to have 1% Nd doping in the center except for CR02 and CR03 which have no Nd. \*Mask placed on target to reduce deposition rate of Cr by roughly \*70% or \*\*90%. <sup>\( \Delta \)</sup>No Nd in film. +substrate of 50x50x1 mm<sup>3</sup> used instead of 44x44x1 mm<sup>3</sup>.

ID	Layout	Composition	O2 (sccm)	Y / Al / Cr / Nd (W)
CR01	1	YAlO	1.9	120 / 120 / 0 / 25
CR02	1	YAlO:Cr (1%) ∆	1.6	110 / 130 / 90** / 0
CR03	1	YAlO:Cr (10%) ∆	2	100 / 150 / 75* / 0
CR04	1	YAlO:Cr (1%)	1.65	110 / 130 / 90** / 25
CR05	1	YAlO:Cr (10%)	1.85	110 / 130 / 90* / 25
CR06	1	YAlO:Cr (20%)	2.1	100 / 150/ 65 / 28
CR07	1	YAlO:Cr (40%)	3.3	100 / 150 / 110 / 40
CR08+	2	YCrO <sub>3</sub>	2.2	135 / 0 / 110 / 20
CR09	2	$Cr_2O_3$	3	0 / 0 / 200 / 30

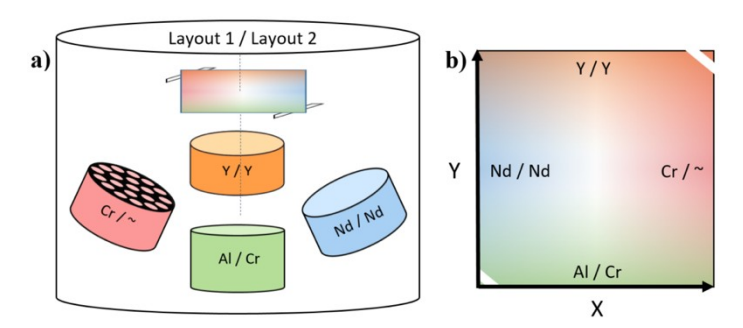


**Fig. 4.1. a)** schematic drawing of the sputter coater with the orientation of each source with respect to film orientation. Two layouts were used to aquire the desired concentration gradients. A mask was used on Cr for films with a low Cr concentration. **b)** The orientation of the films for each measurement with colour gradients to indicate the expected concentration gradient for each element.

### Characterization of Thin Films

Energy-dispersive X-ray spectroscopy (EDS/EDX) measurements were done for 60 seconds using the JEAOL IT-100 EDX/SEM electron microscope at x1000 magnification with an acceleration voltage of 12 kV, probe current of 60% and in a low vacuum pressure of 35 Pa.

X-ray diffraction (XRD) measurements were performed with a fixed slit width of 0.5 cm for half an hour using the PANalytical X'pert Pro MPD diffractometer. The equipment consists of a Cu K $\alpha$  (1.54056 Å) anode which is operating at 45 kV and 40 mA.

Photoluminescence emission, excitation and lifetime measurements used a focused optical parametric oscillator OPO EKSPLA/NT230 laser as excitation source with a pulse duration of 3-6 ns FWHM. Excitation wavelength is tunable between 193 and 2600 nm. A beam splitter is used to re-direct part of the laser to the sample, whilst the transmitted part is read out by Thorlabs thermal power meter to correct for the power of the laser in excitation measurements modes. The laser is focused with a converging lens, however the sample is placed slightly further from the focal point to avoid laser damage due to high power density, the laser spot size is approximately 2 mm in diameter. Appropriate cut-off filters were used to remove the laser observed in second order from emission measurements. The collection of the emission is optimized via two lenses where the sample is located in the focal point of the first lens, the first lens is located two focal lengths away of the second lens and finally an optical fiber is one focal length away of the second lens. The optical fiber is connected to either an Ocean Optics QE Pro (400 to 1100 nm) or the NIRQuest 512 (900 to 1600 nm) spectrometer for emission/excitation measurements. For lifetime measurements the optical fiber is connected to either a Hamamatsu R7600U-20 (300 – 920 nm sensitivity) or Hamamatsu H10330A-75 (950 to 1700 sensitivity) photomultiplier tube both operating at 800V which is subsequently read out by a CAEN DT5724 digitizer after a trigger pulse from the EKSPLA laser.

All measurements, except for XRD measurements, were performed by placing the sample on two translation stages at right angles with precise position read-out. EDS measurements are made on a 5x5 grid whilst photoluminescence measurements are done on a 21x21 grid. This allowed us to directly link the local compositions of the film to the local photo-luminescent properties. Further details on this method can be found in previous work [19].

### 4.4 Results & Discussion

## Thin Film Composition

The concentration (at. %) of Nd in film CR01 is presented in Fig. 4.2a. Per film, a total of 25 points in a 5x5 grid were measured using EDS. Two dimensional linear interpolation and extrapolation were used to retrieve the concentration across the entire film. The corresponding color bar is shared with Fig. 4.2b at the top. A clear gradient is observed with increasing Nd content from right to left; however the gradient is not particularly smooth. This is due to the relatively poor accuracy of EDS for low concentrations. Yet the accuracy is more than enough to verify the expected Nd composition trends increasing from right to left. It can be concluded that the Nd concentration is always below 1 at.% throughout the film and increases approximately linearly from right to left between 0.1 and 0.8 at. %. This linear relationship in concentration with a stationary substrate has also been shown in previous work [20]. The concentration range of Nd was chosen below 1% to prevent any cross relaxation between Nd<sup>3+</sup> atoms which typically occurs at concentrations above 1% [21]. Similarly, in film CR02, the Cr concentration is between 0.1 and 0.7 at. % as shown in Fig. 4.2b. Fig. 4.2c and d show the Y and Al concentration of CR01 respectively and share a different color bar. For the YAlO:Cr, Nd samples (CR01 - CR07), the Nd, Y and Al concentration distribution are fairly constant. Fig. 4.2a-d demonstrate nicely that the alignment of the sputter coater is in such a way that each element is edge-focused to the corresponding side of the substrate, i.e. Nd on the left, Cr on the right, Y at the top and Al at the bottom. The Cr concentration was then systematically increased in the codoped films series, from CR04 to CR07. Within a single film the Cr concentration increases from left to right. In Fig. 4.2e-h, the Y:(Al + Cr) ratio is shown for CR04 -CR07. It is possible to get the Y:(Al+Cr) stoichiometry ratio, y, of the three well-known crystal structure phases with y = 2, 1 and 0.6, for YAM, YAP and YAG respectively, on a single film indicated by the white contour lines in Fig. 4.2e-h. Note that the white contour lines are purely based on measured stoichiometry and are not on the crystal structure patterns. XRD results are presented in the following section. The Y:(Al + Cr) ratio for CR05, CR06 and CR07 are shown in Fig. 4.2f, g and h respectively. Markers are placed on the contour lines of the YAG (Y<sub>3</sub>Al<sub>5-x</sub>Cr<sub>x</sub>O<sub>12</sub>) stoichiometry to indicate certain doping concentrations of  $Cr^{3+}$  where x = 0.025, 0.05, 0.25, 0.5, 1, 1.5 and 2 which correspond to doping percentages of 0.5%, 1%, 5%, 10%, 20%, 30% and 40% respectively. From a compositional point of view, these four films (CR04, CR05, CR06 and CR07) can be used to study the Al<sub>2</sub>O<sub>3</sub>-Y<sub>2</sub>O<sub>3</sub> system with low atomic concentrations of Nd (<1%) and large range of doping concentrations of Cr (0.025 to 40%) within only 4 films. Similarly to the Y:(Al + Cr) ratio, for CR08 the Y:Cr ratio varied linearly from bottom to top in the range of 0.5 to 3 but these results are not shown. CR09 simply

contained Cr<sub>2</sub>O<sub>3</sub> and thus only varied in thickness. Both CR08 and CR09 showed similar Nd content ranging between 0.1 and 0.8 at.% from right to left.

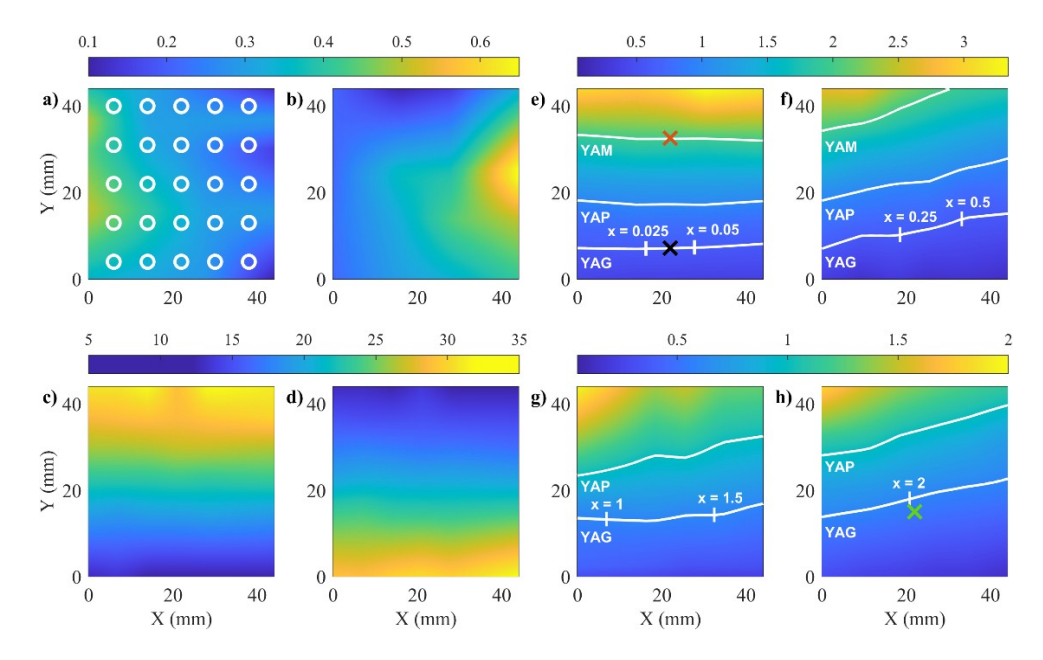


**Fig. 4.2. a)** Heat map of the concentration (at .%) of Nd in CR01, the color bar is shared with b. **b)** Concentration of Cr (at .%) of CR02. **c)** and **d)** concentration of Y and Al (at .%) in CR01 respectively. **e), f), g)** and **h)** ratio between Y and Al + Cr of CR04, CR05, CR06 and CR07 respectively. YAM, YAP and YAG stoichiometry's, where Y:(Al + Cr) are 2, 1 and 0.6, are respectively indicated by the white contour lines . Vertical markers on the YAG contour line indicate number of Al atoms replaced by Cr out of 5 (i.e. Y<sub>3</sub>Al<sub>5-x</sub>Cr<sub>x</sub>O<sub>12</sub>). Colored 'X' markers in black and red in c) and green in f) – indicate where XRD measurements were performed. XRD diffractograms are shown in **Fig. 4.3**.

### Phase identification of thin films

**Fig. 4.3** shows XRD measurements done on specific spots on the CR04, CR07, CR08 and CR09 samples. CR08 and CR09 show as expected characteristic peaks corresponding to the intended YCrO<sub>3</sub> and Cr<sub>2</sub>O<sub>3</sub> phases. CR08 required annealing to promote crystallinity as the as deposited sample was amorphous. CR09 showed crystallinity as deposited and improved on XRD peak intensity after a post anneal treatment.

As shown by the EDS results, we get the stoichiometry of the three main phases of the Al<sub>2</sub>O<sub>3</sub>-Y<sub>2</sub>O<sub>3</sub> system on a single film. However, the correct stoichiometry does not

necessarily translate to the appropriate corresponding phase. One part Y<sub>3</sub>Al<sub>5</sub>O<sub>12</sub> and one part Y<sub>2</sub>O<sub>3</sub> yields a Y:Al ratio of 1 without the YAP phase present. The YAP phase was not identified through XRD measurements anywhere in the samples. The YCrO<sub>3</sub> phase, unlike YAlO<sub>3</sub>, was clearly measured, as shown in Fig. 4.3. The reason for this can be that Y<sub>2</sub>O<sub>3</sub>-Al<sub>2</sub>O<sub>3</sub> is more likely to form the YAG or YAM phases, whereas Y<sub>2</sub>O<sub>3</sub>-Cr<sub>2</sub>O<sub>3</sub> only has the YCrO<sub>3</sub> phase and their respective individual phases (Y<sub>2</sub>O<sub>3</sub> and Cr<sub>2</sub>O<sub>3</sub>). Growing YAP on silica glass has been successful in other work but it was found that using a perovskite substrate promoted a higher chance of success [22]. Prior to annealing, the CR01-CR07 films were amorphous. Upon annealing, the peaks in the XRD diffractogram were present primarily belonging to the YAM and YAG phases. Of all the phases, YAG was most prominent throughout the CR01-CR07 films. Two measurements were done on CR04 at the bottom and top of the sample (indicated by a black and red marker in Fig. 4.2e). Towards the bottom of the film where the stoichiometry resembles that of YAG, the phase is almost exclusively YAG with some YAM. Contrary to the top of the film we see YAG peaks lose intensity whilst YAM peaks increase in intensity, which is as expected when looking at the Y:(Al + Cr) ratio.

Towards the bottom of the CR04 film (indicated by a black 'x' in **Fig. 4.2**c) the amount of Cr is roughly 0.05, whereas in CR07, at the green 'x' marker in **Fig. 4.2**h), it is roughly 2. The peak around 33° is shifted by 0.12° to the left. Replacing Al with Cr leads to a larger lattice due to the Cr ion being bigger than Al. This results in a shift in the XRD peaks to the left, which is shown in the inset in **Fig. 4.3**. This observed shift indicates that Cr successfully takes the place of Al in the YAG phase.

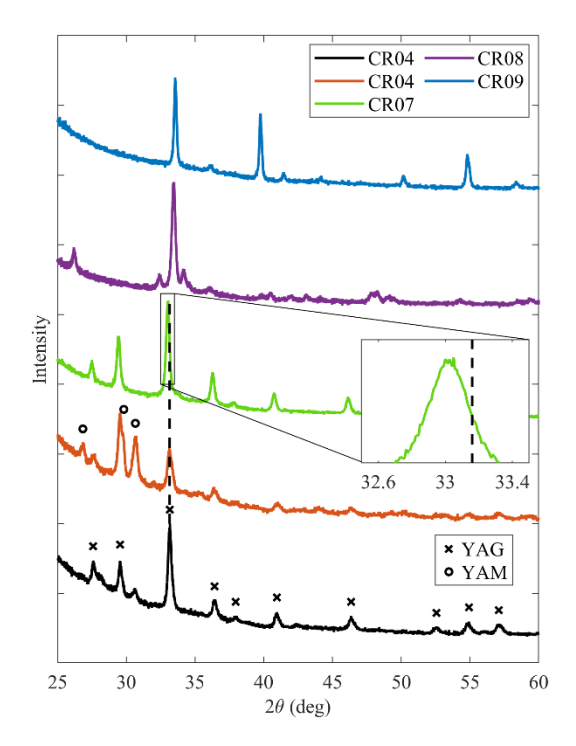


**Fig. 4.3.** XRD measurements of samples CR04, CR07, CR08 and CR09. The black, red, and green plots are measured at their corresponding-colored markers in **Fig. 4.2**e and h. An inset provides a closer look at the peak shift occurring due to Cr doping. Markers of the YAG and YAM peaks are taken from ICDD reference 04-008-3458 and 04-011-4887 respectively. In blue and purple samples CR08 and CR09 are measured and a close match to the Cr<sub>2</sub>O<sub>3</sub> and YCrO<sub>3</sub> phase is found when compared to references 01-078-5443 and 01-081-8632 respectively.

# Chromium absorption

In **Fig. 4.4**a, a series of transmission spectra are plotted from the top to the bottom of the Cr<sub>2</sub>O<sub>3</sub>:Nd sample (CR09). Nd<sup>3+</sup> absorption is not observed due to the weak, parity-forbidden, 4f-4f transitions of trivalent lanthanides. Two clear absorption bands from Cr<sup>3+</sup> can be seen centred around 460 and 600 nm which are attributed to the spin-allowed <sup>4</sup>A to <sup>4</sup>T<sub>1g</sub> and <sup>4</sup>T<sub>2g</sub> transitions which have been reported for Cr in various compounds [23]. At lower energies there is the spin forbidden transition of <sup>4</sup>A to <sup>2</sup>E, also known as the ruby line or R-line, which is not observed but have been reported elsewhere [23]. The absorption below 400 nm is attributed to the optical band-gap which is a result of a charge transfer transition between the 2p oxygen valence band atoms and the Cr<sup>3+</sup> 3d conduction band [23,24]. This charge-transfer absorption prevents the higher energy spin allowed transition <sup>4</sup>A to <sup>4</sup>T<sub>1</sub> to be observed. In **Fig.** 

4.4b the thin film interference fringes in the region of 800 to 1600 nm are fitted at 21x21 points using a combination of the software package OPTIFIT [24, 25] and in-house built software that automates the fitting procedure for each point as described in [19, 27]. Optical constants, n and k, and the thickness are retrieved across the entire film. The thickness ranges in between 350 (at the far side from the Cr target) and 840 nm (at the near side from the Cr target). A thickness map is plotted in **Fig. 4.4**b. The refractive index was found to be around 2.4  $\pm$  0.1 at 586 nm over the whole film. The refractive index is a close match to other fabricated Cr<sub>2</sub>O<sub>3</sub> thin films [18, 28]. An estimation of the transmission of a bulk-like Cr<sub>2</sub>O<sub>3</sub> film, generated by the n and k dispersion relation, given by [26, 27], is shown by the red dotted line. This line indicates the (Mie) scattering and (Fresnel) surface reflection losses. By taking the scattering and reflection loss into account it is possible to estimate the absorption caused by the Cr<sup>3+</sup> transition bands, indicated by the black arrow. Here we look at the absorption at 460 nm. The thickness plotted against this estimated absorption is plotted in Fig. 4.4c. At thicknesses below 700 nm there appear oscillations in a similar fashion to the transmission data which is due to thin film interference. At thicknesses above 700 nm, this behaviour ceases due to the increased absorption, leaving insufficient light to affect the transmission data with thin film interference. This data has been fitted shown in blue using the Lambert-Beer law (equation 4.1) to find an absorption coefficient of 5.4×10<sup>3</sup> cm<sup>-1</sup> at 460 nm. Using the molar mass of Cr to be 152 g/mol and the bulk density of 5.22 g/cm<sup>3</sup> the concentration of Cr ions is 4.1×10<sup>22</sup> cm<sup>-3</sup>. Assuming this concentration is constant over the film we find an absorption cross section of  $1.3 \pm 0.7 \times 10^{-19}$  cm<sup>2</sup>. This uncertainty comes from the estimation in the scattering losses. Note that the density of the thin film has not been measured and can deviate (often lower) from the bulk density. Despite these uncertainties, this result corresponds well with what has been reported for Cr<sup>3+</sup> absorption cross sections found in ruby, which is 1.1×10-19 cm<sup>2</sup> [6, 29].

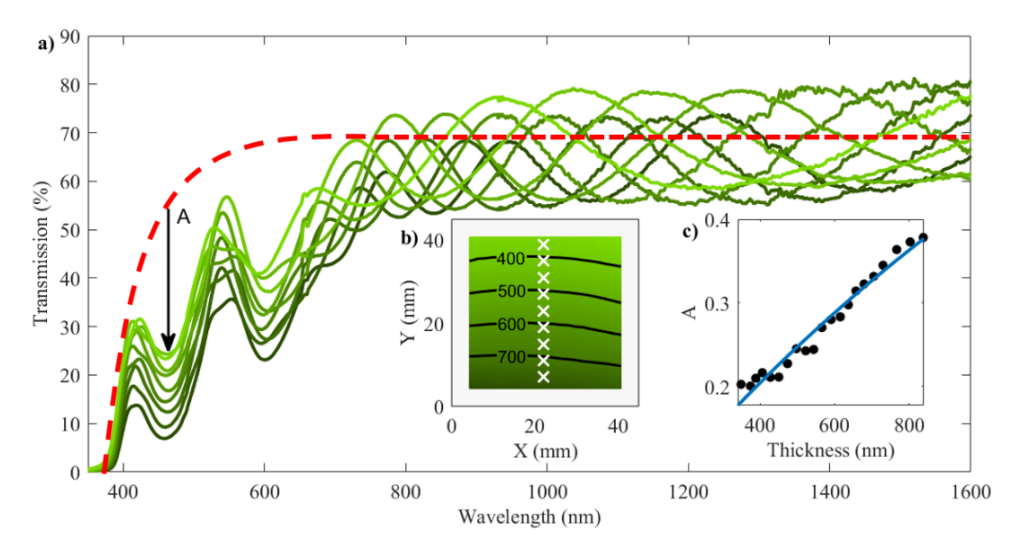


**Fig. 4.4. a)** Transmission measurements of CR09 taken along the arrow in b). The dotted line represents an estimation of the average scattering and reflection losses. The green arrow represents absorption due to Cr<sup>3+</sup>. b) a heat map of the film thickness. c) thickness plotted against absorption for 21 points from top to bottom in the center of the film. These points are fitted with the Lambert Beer law in blue.

In **Fig. 4.5** the transmission spectra as function of Cr content are shown. Measurements for the YAlO films (CR04 – CR07) are taken at the white vertical markers shown in **Fig. 4.2**e-h. The transmission of YCrO<sub>3</sub> was measured where the Y:Cr ratio was 1:1. The charge transfer absorption of Cr below 400 nm becomes stronger with higher content, ultimately leading to match the optical bandgap in Cr<sub>2</sub>O<sub>3</sub>. The lower energy bands of Cr<sup>3+</sup> at 430 and 600 nm are clearly visible in Cr<sub>2</sub>O<sub>3</sub> and YCrO<sub>3</sub>, however at lower concentrations it is difficult to observe due to the thin film interference effects. Optical properties are again fitted using the OPTIFIT method and are shown in **Table 4.2**. Increasing Cr content also leads to a higher refractive index. These results are shown in **Table 4.2**. The theoretical absorption is calculated using the Lambert-Beer law with the absorption cross section found earlier along with thickness found through fitting and the concentrations calculated through the theoretical molecular weight and density of YAG (593 g/mol and 4.6 g/cm<sup>3</sup>), YCrO<sub>3</sub> (189 g/mol, 5.7 g/cm<sup>3</sup>) and Cr<sub>2</sub>O<sub>3</sub> (152 g/mol, 5.2 g/cm<sup>3</sup>).

In this section we have shown through XRD, EDS and optical measurements that these gradient thin films are of consistent quality and can be used to investigate the required concentration of  $Cr^{3+}$  in order to obtain adequate absorption for thin film based LSC applications. Results show that 100%  $Cr^{3+}$ concentration is required in order to achieve 40% absorption at 460 nm for films with thickness below 1  $\mu$ m. In the next section we investigate the luminescence behaviour of low concentrations of  $Nd^{3+}$  inside the  $Al_2O_3$ - $Y_2O_3$  system, with no  $Cr^{3+}$ present.

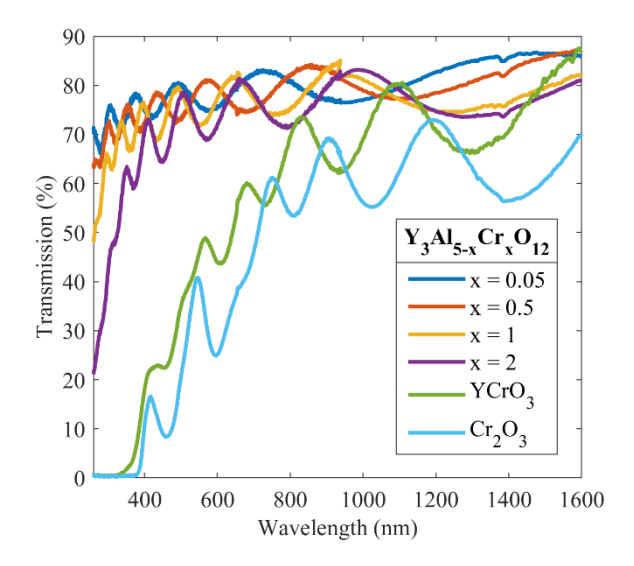


**Fig. 4.5.** Transmission spectra taken from samples CR04-CR09. The specific positions on the films of the measurements for CR04-CR07 are shown via the vertical markers in **Fig. 4.2**e-h. At wavelengths 655 and 933 nm there are discontinuity due to artefacts caused by an intense sharp peak from the deuterium light source and the combining of the spectra from two separate spectrometers respectively.

**Table 4.2.** Refractive index (n) and thickness (d) retrieved through fitting of the thin film interference fringes. Concentrations of  $Cr^{3+}$  are used to estimate film absorption taking the  $Cr^{3+}$  absorption cross-section of **Fig. 4.4c**.

$Y_3Al_{5-x}Cr_xO_{12}$	n	c (cm <sup>-3</sup> )	d (nm)	A (460 nm)
x = 0.05	1.76	$2.3 \times 10^{20}$	412	0.002
x = 0.5	1.78	2.3×10 <sup>21</sup>	480	0.02
x = 1	1.85	4.6×10 <sup>21</sup>	519	0.045
x = 2	1.91	9.2×10 <sup>21</sup>	521	0.09
YCrO <sub>3</sub>	2.16	1.8×10 <sup>22</sup>	782	0.25
$Cr_2O_3$	2.17	4.1×10 <sup>22</sup>	780	0.47

# Single doped Gradient Neodymium Film (YAlO:Nd3+)

In Fig. 4.6a) an excitation and emission spectrum taken at the centre of the film CR01 is presented. Sample CR01 has a similar composition to CR04 that was presented in Fig. 4.2e), with the exception that no Cr<sup>3+</sup> is present. The Y:Al ratio varied between 3.5 and 0.3 from top to bottom (Fig. 4.2e)), whereas the Nd3+ concentration ranged between 0.1 and 0.6 at. % from right to left (Fig. 4.2a). Typical Nd3+ 4f-4f excitation and emission transitions are present. The main emission lines are grouped around 885, 1060 and 1340 nm and correspond to transitions from the <sup>4</sup>F<sub>3/2</sub> manifold to the <sup>4</sup>I<sub>9/2</sub>, <sup>4</sup>I<sub>11/2</sub>, <sup>4</sup>I<sub>13/2</sub> levels respectively. In **Fig. 4.6**b) a heat map is presented of the intensity of the 885 nm emission. Unfortunately, the intensity observed is not only dependent on the intrinsic luminescence properties of the material but also on the out-coupling efficiency controlled by film morphology and surface roughness which is difficult to correct for. The shape of the emission is however unaffected by the these out-coupling effects and can therefore be compared between different locations at the film. In Fig. **4.6**c) three spectra are shown on the top and bottom of the film indicated by the x in Fig. 4.6b). At the top of the film, where the YAM phase is dominant, we see that the emission peak of the  ${}^4F_{3/2} \rightarrow {}^4I_{11/2}$  transition is located at 1058 nm, which is consistent with previous reported literature [29]. Towards the bottom of the film, spectra more related to YAG are observed with a well-known peak at 1064 nm used for laser applications. Both spectra have a broad emission underneath their peaks indicating that inhomogeneous broadening is taking place - which is likely due to amorphous phases being present in the sample. It should be noted that the emission spectrum in Fig. 4.6a) was obtained by two spectrometers. A spectrum from an Ocean Optics QE Pro (400 – 1100 nm) and a NirQuest (900 – 1600 nm) were connected at 900 nm. The spectra have been corrected for their corresponding detector efficiencies. The Ocean Optics QE Pro spectrometer has a higher wavelength resolution, allowing for more detailed photoluminescence structures, and was therefore used for the measurements in Fig. **4.6**c).

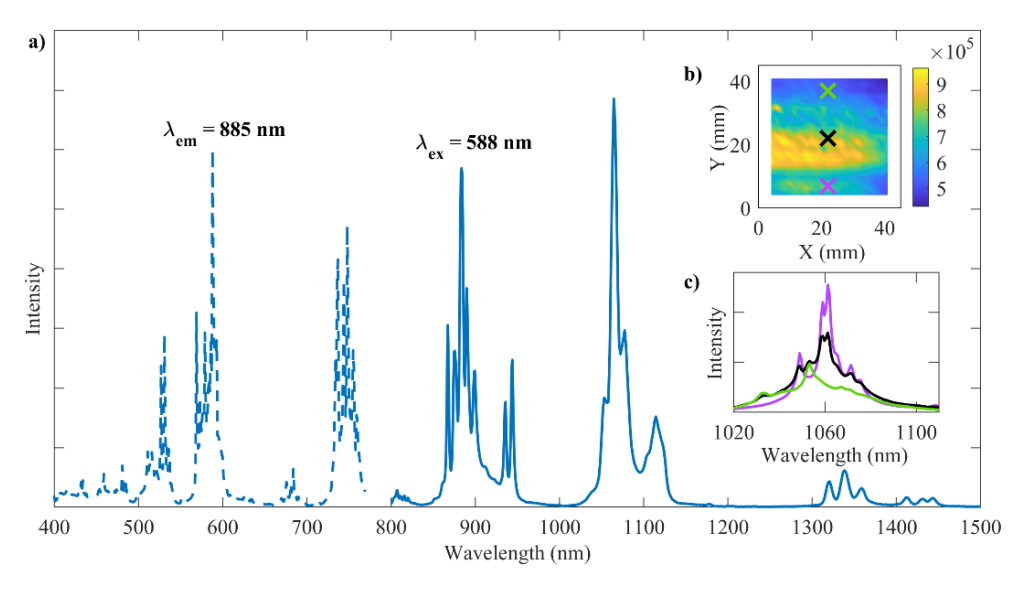


Fig. 4.6. a) Excitation-emission spectra of CR01 when excited in the center of the film. b) Heat map of the  $\lambda_{em} = 1064$  nm intensity of Nd<sup>3+</sup>. c) Emission spectra of Nd<sup>3+</sup> with  $\lambda_{ex} = 588$  nm at two positions on the film indicated by the corresponding colored markers in b.

Similarly to the shape of the emission, the lifetime of the emission is independent of the out-coupling efficiency. The radiative lifetime measurements at four locations on the film – indicated by **Fig. 4.7**b - are shown in **Fig. 4.7**a. The lifetime is not monoexponential and therefore a mean lifetime ( $\tau_{\text{mean}}$ ) is calculated instead using the formula:

$$\tau_{mean} = \frac{\int_0^\infty t \Phi_t(t) dt}{\int_0^\infty \Phi_t(t) dt}$$
 (4.2)

where t is time after excitation (at t=0) and  $\phi_t(t)$  is the time-resolved luminescence intensity. We see that the radiative lifetime ranges from 0.1 to 0.5 ms from bottom to top. These results are consistent with reported literature where the lifetime of Nd<sup>3+</sup> in YAG (bottom of the film) is around 0.24 ms and that of YAM is 0.6 ms [20, 30]. These results demonstrate that this gradient method can be used to study trends as a function of varying host composition. The Nd<sup>3+</sup> lifetime from right to left, where the Nd concentration increases from 0.1 to 0.6 at.%, remains constant, indicating that there is no concentration quenching occurring within the film. Later, when we look at the codoped materials, we can exclude cross-relaxation between Nd<sup>3+</sup> ions to be a cause of non-radiative transitions.

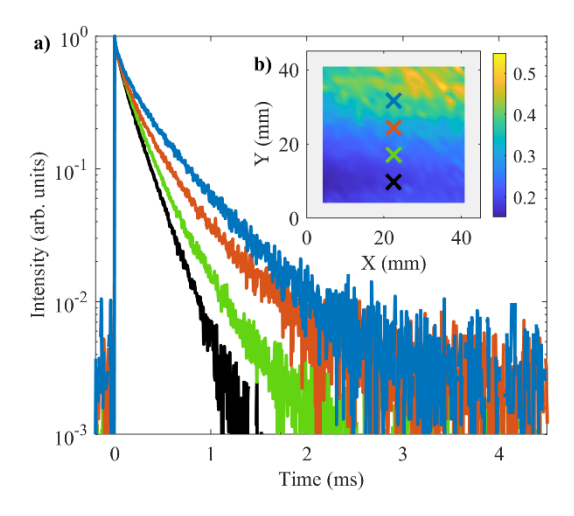


Fig. 4.7. a) Series of lifetime measurements of  $\lambda_{em} = 1064$  nm of Nd<sup>3+</sup> with  $\lambda_{ex} = 588$  nm, measurements are taken of CR01 on locations indicated via corresponding colored markers shown in b. b) Heat map showing the mean decay time in ms across the entire CR01 sample.

# Chromium doped gradient Films (YAlO:Cr3+)

For the YAlO:Cr3+ films, CR02 and CR03, the Cr content increases from left to right from 0.1 to 0.7% (Fig. 4.2b) and 0.6 to 3% respectively. The Y:Al ratio increased from bottom to top in the range of 0.4 to 3.5 in both films (similar to Fig. 4.2e). The excitation and emission spectra taken at the centre of the CR02 film is shown in Fig. 4.8a). In the excitation spectra we see two bands centred around 430 and 600 nm which are associated with the <sup>4</sup>A<sub>2</sub> to <sup>4</sup>T<sub>1</sub> and <sup>4</sup>T<sub>2</sub> transitions observed earlier in the transmission data of Cr<sub>2</sub>O<sub>3</sub> film. The emission closely resembles that of YAG:Cr<sup>3+</sup> which is elsewhere reported [31]. The main R line from the <sup>2</sup>E to <sup>4</sup>A<sub>2</sub> electronic transition is at 688 nm which has vibronic sideband with peaks at 709 and 725 nm. The R-line of YAP:Cr<sup>3+</sup> is situated around the vibronic sideband of YAG:Cr<sup>3+</sup> at 725 nm. The vibronic sidebands of the R-line in YAP:Cr<sup>3+</sup> at longer wavelengths have a peak around 750 nm [31], which is not observed anywhere in the sample. Combining this observation with the lack of YAP-related XRD peaks shows clearly that no YAP:Cr3+ is present anywhere in the sample. A key difference in the emission compared to earlier results is the longer wavelength sideband. Previous studies show that the vibronic sideband of the R line extends to no more than 800 nm [31]. However, we observe emission up until roughly 975 nm. This broad emission at longer wavelength is likely to be caused by Cr3+ ions situated at a site with a low ligand field strength for which the <sup>4</sup>T<sub>2g</sub> level lies below the <sup>2</sup>E level, resulting in broad and redshifted emission. Similar emission is reported for

glasses doped with Cr<sup>3+</sup> [5], indicating that an amorphous phase is also present in our films.

Fig. 4.8b) shows a heat map of the emission around 709 nm when excited at 435 nm. Again, due to the difficulty of correcting for out-coupling efficiencies, no definite statement can be made about where, in the composition space, the sample has the highest emission efficiency. However, it can be noted that towards the top of the sample, where the YAM phase is dominant, there is close to no luminescence observed. In Fig. 4.8c), a photograph of the sample is shown where one can see regions on the film that appear more diffuse or transparent. A horizontal stripe just below the centre of the film appears more transparent (i.e less scattering and lower out-coupling of the emission) which corresponds to the lower emission area in the heat map in Fig. 4.8b).

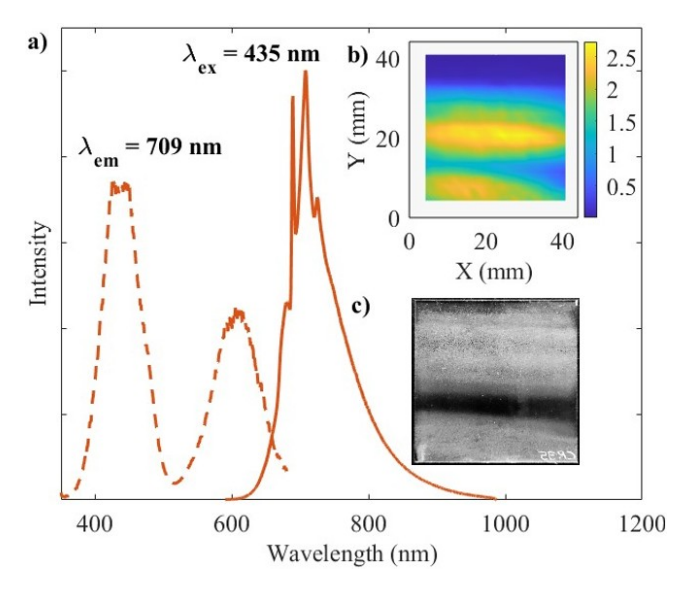


Fig. 4.8. a) Excitation-emission spectra taken at the center of CR03. b) heat map of the  $\lambda_{em}$  = 707 nm intensity. c) black and white photo of film CR02 showing the position dependent scattering nature of the film

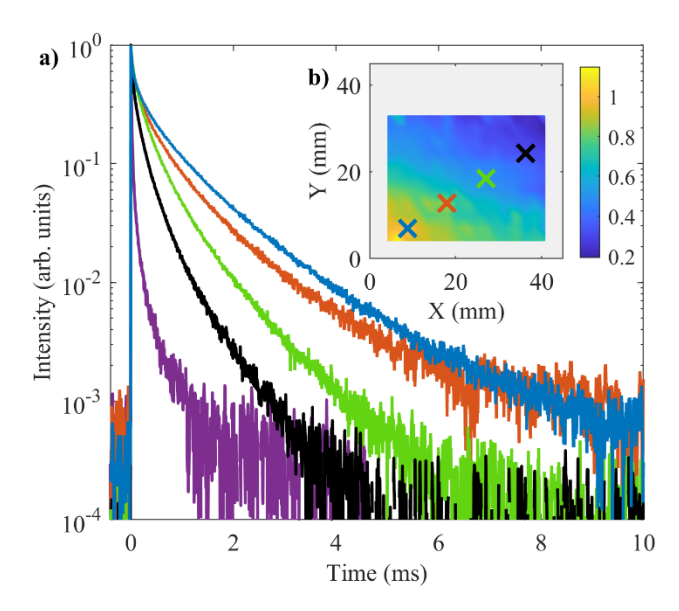


Fig. 4.9. a)  $Cr^{3+}$  lifetime measurements for  $\lambda_{em} = 707$  nm with  $\lambda_{ex} = 430$  nm of CR02 taken at the position indicated by the marker with their corresponding color in b). One measurement of the  $Cr^{3+}$  lifetime in CR03 is shown in purple, where the Cr content is 1.5 at.%. b) heat map of the radiative lifetime (ms) across the film.

In **Fig. 4.9**a), the decay curves of the 707 nm emission, excited with 430 nm, on 4 different locations on the CR02 film are shown. The radiative lifetime was calculated at 11x17 points across the film and is shown in **Fig. 4.9**b). The top part of the sample is not presented as there was no luminescence observed as shown in **Fig. 4.8**b). The radiative lifetime decreases from the bottom left (Cr poor, Al rich region) to the top right (Cr rich, Al poor region) which is consistent with the expectations of concentration quenching effects.

An additional lifetime measurement of CR03 is shown in purple in **Fig. 4.9**a) at a location for which the estimated Cr content is 1.5 at.% with a Y:Al ratio of 0.6 (YAG). The mean lifetime according to equation (**4.2**) is found to be 0.08 ms. The bottom left corner of CR02 has a lifetime around 1 ms (shown in blue in **Fig. 4.9**a), this position also has the YAG ratio, but the Cr content is estimated to be 0.1 at.%. This decrease in lifetime due to concentration quenching has been extensively studied in the past and is contributed to Cr-Cr pairs and Cr clusters acting as quenching centres [14, 15]. These exchange coupled Cr-Cr pairs start to form at concentrations > 0.5 at%. Previous studies show a radiative lifetime of the R-line emission of Cr<sup>3+</sup> to be 1.7 ms at 0.5 at.%

[16, 32], indicating significant radiative losses in the bottom left corner of CR02. This can be caused by mixed phases and defects present in the material.

So far we have looked at the Al<sub>2</sub>O<sub>3</sub>-Y<sub>2</sub>O<sub>3</sub> system doped separately with Nd<sup>3+</sup> and Cr<sup>3+</sup>. On single films we explained luminescent behaviour as function of host and concentration of both Nd<sup>3+</sup> and Cr<sup>3+</sup>. To further test this gradient film method, we now co-dope the films with Cr<sup>3+</sup> and Nd<sup>3+</sup> and investigate the energy transfer from Cr<sup>3+</sup> to Nd<sup>3+</sup> as a function of Cr<sup>3+</sup> concentration.

# Double doped thin films (Y<sub>3</sub>Al<sub>5-x</sub>Cr<sub>x</sub>O<sub>12</sub>:Cr<sup>3+</sup>, Nd<sup>3+</sup>)

In Fig. 4.10 the excitation and emission spectra taken at x = 0.05 and x = 0.5 (Y<sub>3</sub>Al<sub>5</sub>. <sub>x</sub>Cr<sub>x</sub>O<sub>12</sub>) of films CR04 and CR05 are presented. By monitoring the Nd<sup>3+</sup> 1060 nm emission, we can clearly see the two broad bands of  $Cr^{3+}$ , providing evidence that energy transfer is taking place. For x = 0.05 there remain Nd<sup>3+</sup> 4f-4f lines (around 530 and 588 nm) observed on top of the broad Cr<sup>3+</sup> bands. This indicates that the Nd<sup>3+</sup> emission when excited via Cr<sup>3+</sup> is comparable in intensity to the direct excitation of Nd<sup>3+</sup>. Generally, the emission is equal to the product of absorption, the energy transfer efficiency (if applicable) and the quantum yield. The observed comparable emission intensity when exciting through Cr3+ or directly into Nd3+ shows that the efficiency of the energy transfer must be low as the absorption of the spin-allowed Cr<sup>3+</sup> transition is much stronger than that of the parity forbidden 4f-4f transitions of Nd3+. This is with the assumption that the quantum yield of Nd3+ remains unchanged with the introduction of  $Cr^{3+}$ . However, at x = 0.5 (CR05),  $Cr^{3+}$  absorption dominates due to the higher concentration of Cr<sup>3+</sup> and the 4f-4f lines are hardly detectable which is observed in Fig. 4.10a). The Cr content increases by a factor of 10 from CR04 and CR05, which increases the Cr3+ absorption at 460 nm by a factor of 10 as shown in **Table 4.2.** The intensity of the excitation of Nd<sup>3+</sup> at 460 nm increases roughly by a factor 2, indicating that the energy transfer efficiency from Cr3+ to Nd3+ has decreased by a factor 5 with the increased Cr3+ content. This can be a result from the formation of Cr pairs and clusters acting as quenching centers discussed in the previous, single doped YAlO: $Cr^{3+}$  section. Furthermore, we can see from the solid blue plot (x = 0.05) in Fig. 4.10a, that with  $\lambda_{ex} = 430$  nm the emission consists of YAG:Cr<sup>3+</sup>, YAG:Nd<sup>3+</sup> and a broad band emission with a peak centered around 840 nm as shown by the solid black fitted curve to guide the eye. The broad emission has been attributed to the <sup>4</sup>T<sub>2</sub>  $\rightarrow$  <sup>4</sup>A<sub>2</sub> transition for Cr<sup>3+</sup> situated at sites with low ligand field strength. When increasing the Cr from x = 0.05 to x = 0.5 in YAG:Cr<sup>3+</sup>, the YAG:Cr<sup>3+</sup> emission is fully quenched. Despite the quenched YAG:Cr<sup>3+</sup> emission, there is still energy transfer taking place, as evidenced by the characteristic Cr<sup>3+</sup> bands in the excitation spectra. The broad band emission remains present in the emission spectra at the higher Cr concentration. To investigate the origin of the energy transfer between Cr<sup>3+</sup> and Nd<sup>3+</sup>, radiative lifetime measurements are performed and presented in the following section.

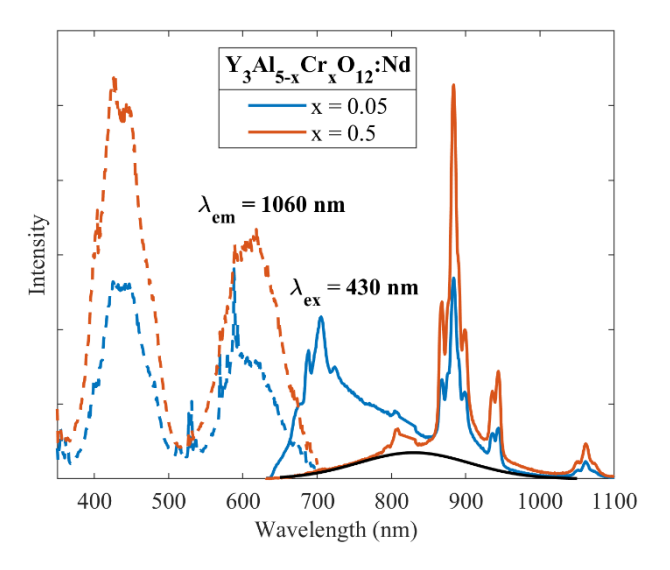


**Fig. 4.10.** Excitation ( $\lambda_{em} = 1060$  nm) and emission spectra ( $\lambda_{ex} = 430$  nm) of CR04 and CR05 taken at positions indicated by the vertical markers, shown in **Fig. 4.2c**) and d). Their stoichiometries ( $Y_3Al_{5-x}Cr_xO_{12}:Nd$ ) are x = 0.05 and x = 0.5. The solid black line represents emission from  $Cr^{3+}$  ions situated at sites with low ligand field fitted with a Gaussian function (using an eV scale).

In **Fig. 4.11**a) we see the time resolved intensity of the Cr<sup>3+</sup> R-line ( $\lambda_{em} = 707 \text{ nm}$ ) for the singly doped YAG:Cr3+ (CR02) and doubly doped YAG:Cr3+, Nd3+ thin film (CR04) shown in red and blue respectively. Measurements were done at the location for both films where the YAG stoichiometry was x = 0.05 which is shown with a marker labelled x = 0.05 in Fig. 4.2e). The mean lifetime of R-line  $Cr^{3+}$  emission for double doped YAG:Cr3+, Nd3+ was found to be 0.2 ms. This is four times shorter than the mean lifetime of the singly doped Cr3+ film CR02 which has a mean lifetime of around 0.8 ms. The decrease of the radiative lifetime is mainly caused by the introduction of a fast component which dominates until about t > 0.2 ms. However, the tail (>1 ms) of the Cr<sup>3+</sup> emission can be well fitted with a single exponential with a lifetime of 0.8 ms (R-square = 0.9907), similar to the mean lifetime of the single-doped Cr<sup>3+</sup> films. This suggests that energy transfer is taking place between the R-line and Nd3+ 4f states in the first 0.2 ms. When comparing the lifetime of the Nd3+ emission in the single doped YAG:Nd<sup>3+</sup> (CR01) with the double doped YAG:Nd<sup>3+</sup>, Cr<sup>3+</sup> (CR04), shown in Fig. **4.11b**) in red and blue respectively, it can be seen that there is indeed a rise time for the double doped YAG:Nd<sup>3+</sup>, Cr<sup>3+</sup>. However, this rise time appears much shorter than the

fast component of the Cr³+ emission. Generally, if energy transfer occurs between a donor (Cr³+) and acceptor (Nd³+) where the lifetime of the donor (0.8 ms) is longer than that of the acceptor (0.24 ms) one would expect the lifetime of the acceptor to be the same as the lifetime of the donor. For the Cr³+ Nd³+ system, it has been shown in previous studies that the Nd³+ lifetime has been reported to lengthen, from 0.24 to 0.4 ms due to energy transfer from the R-line of Cr in YAG [16]. In our case the mean lifetime of the Nd³+ 1340 nm emission when excited through Cr³+ is found to only slightly increases to 0.26 ms. Taken together, the reduction in the Cr³+ R-line mean lifetime in our sample does not appear to be caused by the energy transfer to Nd³+. The origin of this fast component has not been studied but can be the result of increased quenching centers caused by a poor incorporation of Nd³+ in the film.

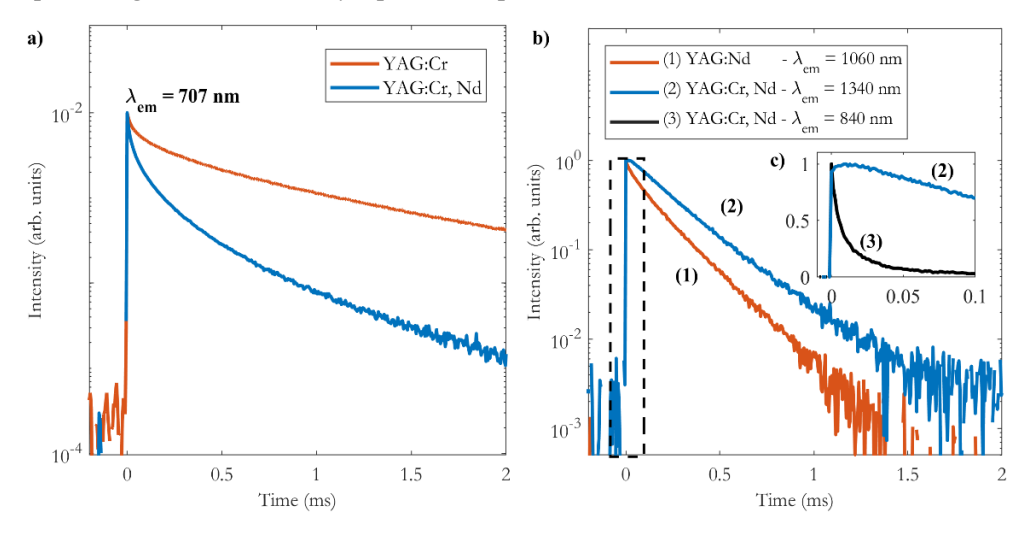


**Fig. 4.11. a)** Radiative lifetime of the Cr³+ R-line<sup>+</sup> ( $\lambda_{em}$  = 707 nm) in single doped YAG:Cr³+ and double doped YAG:Cr³+, Nd³+ with  $\lambda_{ex}$  = 620 nm. **b)** Radiative lifetime of the Nd³+ <sup>4</sup>F<sub>3/2</sub> manifold ( $\lambda_{em}$  = 1060 and 1340 nm) in single doped YAG:Nd³+ and double doped YAG:Cr³+, Nd³+ with  $\lambda_{ex}$  = 588 nm and  $\lambda_{ex}$  = 620 nm respectively. **c)** A shorter timeframe that includes the radiative lifetime of the broad Cr³+ emission around 840 nm in YAG:Cr³+, Nd³+ with  $\lambda_{ex}$  = 620 nm. All measurements were taken at locations with a YAG stoichiometry of x = 0.05 as shown in **Fig. 4.2**e.

In **Fig. 4.11c**) the lifetime of the broad  $Cr^{3+}$  emission ( ${}^4T_2 \rightarrow {}^4A_2$ ) around 840 nm is compared to the lifetime of the 1340 nm emission of Nd<sup>3+</sup> when excited at 435 nm. This broad emission of  $Cr^{3+}$  has a mean lifetime of 54 µs, which is much shorter than the R-line. This is due to the spin-allowed nature of the transition. We see that the rise time of Nd<sup>3+</sup> matches closely to the decay of this broad emission. Therefore, energy transfer appears to mainly take place between the low crystal field sites and Nd<sup>3+</sup> rather than between  $Cr^{3+}$  ions at regular lattice sites in YAG. The observed energy transfer between the broad emission of  $Cr^{3+}$  and Nd<sup>3+</sup>, rather than between the R-line of  $Cr^{3+}$ 

and Nd<sup>3+</sup>, makes sense when considering the better spectral overlap between the emission and absorption of Cr<sup>3+</sup> and Nd<sup>3+</sup> respectively and has been noted before [4].

Lastly, the mean radiative lifetime of Nd3+ is measured as a function of Cr3+ concentration in the YAG part of the films. In Fig. 4.12) we measure the lifetime of Nd<sup>3+</sup> as a function of x (Y<sub>3</sub>Al<sub>5-x</sub>Cr<sub>x</sub>O<sub>12</sub>) when exclusively exciting Cr<sup>3+</sup> at 435 nm. At low Cr concentration (x < 0.2) the mean lifetime of Nd<sup>3+</sup> is between 0.24 and 0.28 ms. The slightly longer mean lifetime of Nd3+ in YAG:Cr3+, Nd3+ over single doped YAG:Nd<sup>3+</sup> is likely due to the added rise time of Nd<sup>3+</sup> without suffering of subsequent quenching. However, increasing the Cr3+ concentration further leads to a systematic decrease in Nd3+ lifetime. The Nd concentration was kept low (<0.1 at%) to eliminate cross relaxation between Nd3+ ions to be a cause in drop of lifetime. The reduction in Nd<sup>3+</sup> lifetime can be caused by the incorporation of Cr<sup>4+</sup> inside the tetrahedral Al site in the YAG phase. Cr4+ has broad absorption around 1000 nm which can cause energy transfer from Nd3+ to Cr4+ [22]. If Cr3+ situated in low ligand field strength sites are nearby Nd3+ then energy transfer can also occur between the 4F3/2 and the 4T2 of Nd3+ and Cr<sup>3+</sup> respectively. Other culprit candidates are the host material which can have defects and mixed phases. An extensive study to investigate this quenching routes has not been done.

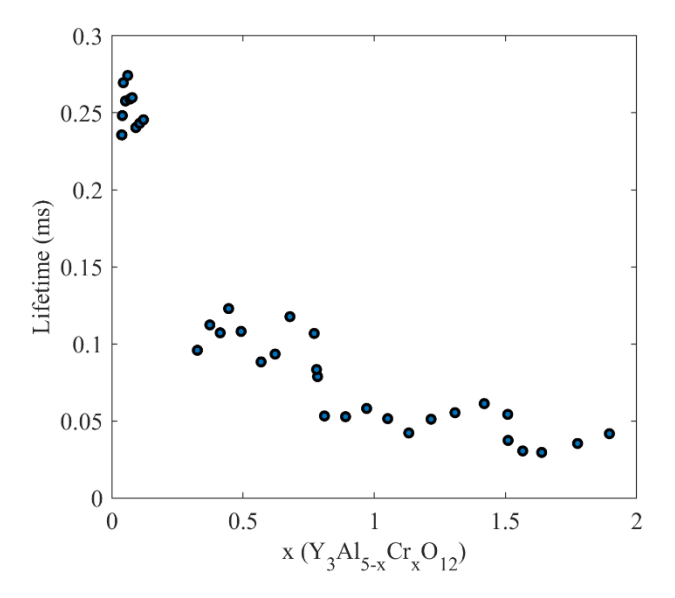


Fig. 4.12. Radiative lifetime of nm Nd<sup>3+</sup> emission ( $\lambda_{em} = 1340$  nm) as function of Cr content.

The aim of this work was to investigate further the interplay of strong  $Cr^{3+}$  absorption and subsequent energy transfer and emission of  $Nd^{3+}$ . In **Fig. 4.12** the  $Nd^{3+}$  lifetime drops to 0.05 ms at  $Cr^{3+}$  concentration of 10 at.% (x = 2) in YAG. To increase the  $Cr^{3+}$ 

further the YCrO<sub>3</sub> (20 at.% Cr<sup>3+</sup>) and Cr<sub>2</sub>O<sub>3</sub> (40 at.% Cr<sup>3+</sup>) host were briefly studied. In the Cr<sub>2</sub>O<sub>3</sub> and YCrO<sub>3</sub> films doped with Nd<sup>3+</sup> there was no emission of Nd<sup>3+</sup>, regardless of exciting exclusively in Cr<sup>3+</sup> or Nd<sup>3+</sup>. It appears that fully concentrated Cr<sup>3+</sup> systems like YCrO<sub>3</sub> and Cr<sub>2</sub>O<sub>3</sub>, do provide the desired absorption but are unable to facilitate energy transfer to Nd<sup>3+</sup>.

### 4.5 Conclusion

In this work we have provided, using the gradient sputtering approach, evidence that it is possible to acquire > 40% Cr<sup>3+</sup> absorption within a <1  $\mu$ m thin film with a fully concentrated Cr<sup>3+</sup> system i.e. Cr<sub>2</sub>O<sub>3</sub>.

The  $Al_2O_3$ - $Y_2O_3$  system was chosen to study the luminescent behavior of  $Cr^{3+}$  and  $Nd^{3+}$  both independently doped and co-doped. On a single film, via gradient sputtering, the Y:Al ratio varied between 0.5 and 3.5 which encompasses the stoichiometry of the YAG, YAP and YAM phases. XRD measurements showed YAG and YAM phases were present. No YAP phase was detected. Position dependent emission and lifetime measurements of  $Al_2O_3$ - $Y_2O_3$  gradient films doped with  $Nd^{3+}$  corroborated previously observed behavior of  $Nd^{3+}$  emission and lifetime across the films going from the YAM to the YAG dominant part of the film indicating the good quality of our films. The main emission peak ( ${}^4F_{3/2} \rightarrow {}^4I_{11/2}$ ) shifts from 1058 nm (YAM:Nd<sup>3+</sup>) to 1064 nm (YAG:Nd<sup>3+</sup>). The lifetime of the  ${}^4F_{3/2}$  level decreases from 0.6 to 0.24 ms typically for YAM:Nd<sup>3+</sup> and YAG:Nd<sup>3+</sup> respectively on a single film. These results demonstrate the unique value of this gradient method to study luminescent thin films.

Al<sub>2</sub>O<sub>3</sub>-Y<sub>2</sub>O<sub>3</sub> doped with Cr<sup>3+</sup> showed characteristic YAG:Cr<sup>3+</sup> emission with an R-line ( ${}^{2}E \rightarrow {}^{4}A_{2}$ ) emission at 707 nm. A broad emission in the near infrared ( ${}^{4}T_{2} \rightarrow {}^{4}A_{2}$ ) was also observed in the films. The mean lifetime of the R-line Cr<sup>3+</sup> emission in YAG was found to be 0.8 ms and shortened to 0.2 ms towards the Cr<sup>3+</sup> rich part of the film.

More data was provided on the Al<sub>2</sub>O<sub>3</sub>-Y<sub>2</sub>O<sub>3</sub> system doped with both Nd<sup>3+</sup> and Cr<sup>3+</sup> in order to investigate the energy transfer between Cr<sup>3+</sup> and Nd<sup>3+</sup> in the various identified phases. Excitation spectra have shown that Nd<sup>3+</sup> can be excited through Cr<sup>3+</sup>. Increasing Cr<sup>3+</sup> from 1% doping to 10% doping in YAG part of the film improved absorption of Cr<sup>3+</sup> but reduced energy transfer efficiency to Nd<sup>3+</sup>, potentially due to Cr pairs and clusters. The observed rise-time of the Nd<sup>3+</sup> emission intensity was found to match the decay of the broad-band emission of Cr<sup>3+</sup>, rather than that of the R-line. The energy transfer therefor appears to take place between the Cr<sup>3+</sup> ions situated at sites with low ligand field strength and Nd<sup>3+</sup>. Finally, fully concentrated Cr<sub>2</sub>O<sub>3</sub> and YCrO<sub>3</sub>, though promising due to their absorption, showed no energy transfer to Nd<sup>3+</sup> and appear to be ill-suited for thin film based LSC applications. Energy transfer was studied between Cr<sup>3+</sup> and Nd<sup>3+</sup> as function of Cr<sup>3+</sup> concentration. At high concentration (>0.5 at.%) of Cr<sup>3+</sup>, in the YAG part of the thin-films, the Nd<sup>3+</sup> lifetime systematically decreased from 0.25

to 0.05 ms, possibly due to transfer to  $Cr^{4+}$  or due to back-transfer to  $Cr^{3+}$  situated at low ligand field strength sites, which has been previously reported. The combination of reduced energy transfer to  $Nd^{3+}$  due to the Cr pairs/clusters and back-transfer from  $Nd^{3+}$  to  $Cr^{3+/4+}$  limits their use in thin film based LSCs.

## 4.6 References

- W. H. Weber and J. Lambe, 'Luminescent greenhouse collector for solar radiation', Applied Optics, 15, 2299-2300 (1976). doi:10.1364/ao.15.002299.
- [2] J.S. Batchelder, A.H. Zewai and T. Cole 'Luminescent Solar Concentrators 1: Theory of operation and techniques for performance evaluation', Applied Optics, 18, 3090-3110 (1979). doi:10.1364/ao.18.003090.
- [3] B.C. Rowan, L.R. Wilson and B.S. Richards, 'Advanced Material Concepts for Luminescent Solar Concentrators', IEEE Journal of Selected Topics in Quantum Electronics, 14(5), 1312–1322 (2008). doi:10.1109/jstqe.2008.920282.
- [4] R. Reisfeld, 'Future technological applications of rare-earth-doped materials', Journal of the Less Common Metals, 93(2), 243–251 (1983). doi:10.1016/0022-5088(83)90163-7.
- [5] B. Jeżowska-Trzebiatowska, E. Łukowiak, W. Stręk, A. Buczkowski, S. Patela, J. Radojewski, J. Sarzyński, 'Neodymium-chromium doped phosphate glasses as luminescent solar concentrators', Solar Energy Materials, 13(4), 267–277 (1986). doi:10.1016/0165-1633(86)90002-x.
- [6] E. H. Penilla, C. L. Hardin, Y. Kodera, S. A. Basun, D. R. Evans, and J. E. Garay, 'The role of scattering and absorption on the optical properties of birefringent polycrystalline ceramics: Modeling and experiments on ruby (Cr:Al<sub>2</sub>O<sub>3</sub>),' Journal of Applied Physics, 119(2), 023106 (2016). doi:10.1063/1.4939090.
- [7] Z.J. Kiss and R.J. Pressley, 'Crystalline solid lasers', Proceedings of the IEEE, 54(10), pp. 1236–1248 (1966). doi:10.1109/proc.1966.5112.
- [8] T. Saiki, K. Imasaki, S. Motokoshi, C. Yamanaka, H. Fujita, M. Nakatsuka, Y. Izawa, 'Disk-Type Nd/Cr:YAG ceramic lasers pumped by arc-metal-halide-lamp,' Optics Communications, 268(1), 155–159 (2006). doi:10.1016/j.optcom.2006.07.002.
- [9] L. Marciniak, A. Bednarkiewicz, J. Drabik, K.Trejgis and W. Strek, 'Optimization of highly sensitive YAG:Cr<sup>3+</sup>,Nd<sup>3+</sup> nanocrystal-based luminescent thermometer operating in an optical window of biological tissues', Physical Chemistry Chemical Physics, 19(10), 7343–7351 (2017). doi:10.1039/c6cp07213e.
- [10] J. A. Mareš, W. Nie and G. Boulon, 'Multisites and energy transfer in Cr<sup>3+</sup>-Nd<sup>3+</sup> codoped Y<sub>3</sub>Al<sub>5</sub>O<sub>12</sub> and YAlO<sub>3</sub> Laser Crystals', Journal de Physique, 51(15), 1655–1669 (1990). doi:10.1051/jphys:0199000510150165500.
- [11] S. R. Rotman, E. Luria, E. Herman, A. Shohan, J. A. Mares, G. Boulon, A. Brenier, L. Lou, 'Fast energy transfer from donor pairs to single acceptors in a Cr<sup>3+</sup>, Nd<sup>3+</sup>-doped YAlO<sub>3</sub> crystal', Optical Materials, 13(1), 63–65 (1999). doi:10.1016/s0925-3467(99)00012-9.
- [12] M. J. Weber, 'Chromium—rare-earth energy transfer in YAlO<sub>3</sub>', Journal of Applied Physics, 44(9), 4058–4064 (1973). doi:10.1063/1.1662895.
- [13] J. A. Mareš, Z. Khás, W. Nie and G. Boulon, 'Nonradiative energy transfer between Cr<sup>3+</sup> and Nd<sup>3+</sup> multisites in Y<sub>3</sub>Al<sub>5</sub>O<sub>12</sub> laser crystals', Journal de Physique I, 1(6), 881–899 (1991). doi:10.1051/jp1:1991174.
- [14] G.F. Imbusch, 'Energy Transfer in Ruby', Physical Review, 153(2), 326–337 (1967). doi:10.1103/physrev.153.326.
- [15] G.F. Imbusch, 'Energy transfer in heavily-doped ruby', Journal of Luminescence, 53(1–6), 465–467 (1992). doi:10.1016/0022-2313(92)90199-j.
- [16] K. Fujioka, T. Saiki, S. Motokoshi, Y. Fujimoto, H. Fujita, M. Nakatsuka, 'Luminescence properties of highly Cr co-doped Nd:YAG powder produced by sol–gel method', Journal of Luminescence, 130(3), 455–459 (2010). doi:10.1016/j.jlumin.2009.10.012.
- [17] K. Strijckmans, R. Schelfhout, and D. Depla, "Tutorial: Hysteresis during the reactive magnetron sputtering process", Journal of Applied Physics, 124(24), 241101 (2018). doi:10.1063/1.5042084.
- [18] P. Hones, M. Diserens and F. Lévy, 'Characterization of sputter-deposited chromium oxide thin films', Surface and Coatings Technology, 120–121, 277–283 (1999). doi:10.1016/s0257-8972(99)00384-9.
- [19] E. P. J. Merkx, and E. van der Kolk, 'Method for the detailed characterization of co-sputtered inorganic luminescent material libraries', ACS Combinatorial Science, 20(11), 595–601 (2018). doi:10.1021/acscombsci.8b00068.

- [20] Y. Deng, J.D. Fowlkes, J.M. Fitz-Gerald and P.D. Rack, 'Combinatorial thin film synthesis of Gd-doped Y<sub>3</sub>Al<sub>5</sub>O<sub>12</sub> ultraviolet emitting materials', Applied Physics A, 80(4), 787–789 (2005). doi:10.1007/s00339-003-2385-0.
- [21] L. D. Merkle, M. Dubinskii, K. L. Schepler and S. M. Hegde, 'Concentration quenching in fine-grained ceramic Nd:YAG', Optics Express, 14(9), 3893-3905 (2006). doi:10.1364/oe.14.003893.
- [22] Y. Shimizu, K. Ueda, F. Massuyeau, S. Jobic, 'Preparation of thin films of perovskite-type YAlO<sub>3</sub>:Gd<sup>3+</sup> Pr<sup>3+</sup> UV phosphors', Thin Solid Films, 571, 90–93 (2014). doi:10.1016/j.tsf.2014.09.075.
- [23] R.S. Pavlov, V.B. Marzá, and J.B. Carda, 'Electronic absorption spectroscopy and colour of chromium-doped solids', J. Mater. Chem., 12(9), 2825–2832 (2002). doi:10.1039/b201802k.
- [24] A. N.L. Jara, J. F. Carvalho, A. F. Júnior, L. J.Q. Maia, R. C. Santana, 'On the optical and magnetic studies of YCrO<sub>3</sub> Perovskites', Physica B: Condensed Matter, 546, 67–72 (2018). doi:10.1016/j.physb.2018.07.026.
- [25] R. Alvarez, A. Garcia-Valenzuela, C. Lopez-Santos, F.J. Ferrer, V. Rico, E. Guillen, M. Alcon-Camas, R. Escobar-Galindo, A.R. Gonzalez-Elipe, A. Palmero, 'High Rate Deposition of Stoichiometric Compounds by Reactive Magnetron Sputtering at Oblique Angles', Plasma Process. Polym., 13, 960– 964 (2016). doi:10.1002/ppap.201600019.
- [26] R. Swanepoel, 'Determination of the thickness and optical constants of amorphous silicon', Journal of Physics E: Scientific Instruments, 16(12), 1214–1222 (1983). doi:10.1088/0022-3735/16/12/023.
- [27] E. P. J. Merkx, S. van Overbeek, and E. van der Kolk, 'Functionalizing window coatings with luminescence centers by combinatorial sputtering of scatter-free amorphous SiAlON:Eu<sup>2+</sup> thin film composition libraries', Journal of Luminescence, 208, 51-56 (2019). doi:10.1016/j.jlumin.2018.12.011.
- [28] M.F. Al-Kuhaili and S.M.A. Durrani, 'Optical properties of chromium oxide thin films deposited by electron-beam evaporation', Optical Materials, 29(6), 709–713 (2007). doi:10.1016/j.optmat.2005.11.020.
- [29] D.M. Dodd, D.L. Wood, and R.L. Barns, 'Spectrophotometric Determination of Chromium Concentration in Ruby', Journal of Applied Physics, 35(4), 1183–1186 (1964). doi:10.1063/1.1713590.
- [30] W. Ryba-Romanowski, R. Lisiecki, A. Rzepka, L. Lipińska, A. Pajączkowska, 'Luminescence and excitation energy transfer in rare earth-doped Y<sub>4</sub>Al<sub>2</sub>O<sub>9</sub> nanocrystals', Optical Materials, 31(8), 1155–1162 (2009). doi:10.1016/j.optmat.2008.12.006.
- [31] K.M. Kinsman, J. McKittrick, E. Sluzky, and K. Hesse, 'Phase Development and Luminescence in Chromium-Doped Yttrium Aluminum Garnet (YAG:Cr) Phosphors', Journal of the American Ceramic Society, 77, 2866-2872 (1994). https://doi.org/10.1111/j.1151-2916.1994.tb04516.x.
- [32] Z.Y. Zhang and K.T.V Grattan, 'Temperature dependence of YAG:Cr<sup>3+</sup> fluorescence lifetime up to 550 K', Journal of Luminescence, 62(6), 263–269 (1994). doi:10.1016/0022-2313(94)90046-9.

#### 5.1 Abstract

The broad class of Cu(Al,Ga,In)(S,Se,Te)<sub>2</sub> solar absorber materials when doped with Yb3+ are interesting for thin film based luminescent solar concentrator (LSCs) application. In this work the strong and broad absorption properties of co-sputtered CuGaS<sub>2</sub> (CGS) thin films combined with the luminescent properties of Yb are reported. Energy-dispersive x-ray spectroscopy (EDS), x-ray diffraction, transmission, excitation, and temperature dependent emission as well as radiative lifetime measurements are performed on thin films with varying Cu:Ga ratios and Yb3+ concentrations. It is found that Yb<sup>3+</sup> emission can be broadly sensitized by the host in the range of 200 to 600 nm. A lower Cu:Ga ratio, crystallinity and post annealing in air provides a positive impact on the sensitization of Yb3+ emission. The temperature dependent time integrated decay curves show a clear thermal energy barrier of about 0.2 eV. Because the exponential tail, with a lifetime of 110 µs, is constant with temperature, we conclude that the barrier is connected to the thermal release of electrons trapped at the Yb<sup>2+</sup> ground state. The low energy transfer efficiency from the host to the Yb dopant is attributed to efficient non-radiative electron-hole pair recombination. The prospects and design criteria of Cu(Al,Ga,In)(S,Se,Te)<sub>2</sub> solar absorber materials for LSC applications is the further subject of the discussion.

The content of this chapter is based on the publication:

**Derksen, M.**, Bergkamp, S., Kohnstamm, O. and van der Kolk, E., 2024. Time, temperature and concentration resolved Yb<sup>3+</sup> luminescence study in co-sputtered Cu<sub>2-x</sub>Ga<sub>x</sub>S<sub>2</sub> (0.1< x< 1.6) thin films with a Cu-Ga composition gradient. *Optical Materials*, p.116220.

### 5.2 Introduction:

#### CIGS and LSCs

Copper Gallium/Indium Selenide/Sulfide (CIGS) type thin film solar cells gained significant interest since their debut in 1976 [1]. The versatility, strong absorption coefficient and lower manufacturing cost compared to traditional Si solar cells was the driving force behind their continued development. From the inception of the CIGS to now, the energy conversion efficiencies improved from a meager 4.5% to an impressive 22.3% [1, 2]. Despite this significant improvement, the thin film based solar cells (including CIGS, CdTe and amorphous Si-based) market share has been steadily decreasing from 17% in 2009 to 7-8% in 2014. Several factors contribute to this decline including the reduced cost in conventional crystalline Si solar cells, the reluctance to work with known toxic elements such as Cd and relatively scarce metals such as In [3].

Luminescent solar concentrators (LSCs) share a similar story to that of the CIGS solar cells. First conceptualized in the same year as the CIGS thin film solar cell and vastly improved power conversion efficiencies over the years [4, 5]. The basic operating principle of an LSC is to absorb incoming sunlight using a sheet of glass or polymer doped with luminescent centers. The absorbed sunlight is re-emitted at longer wavelengths by the luminescent centers and is wave-guided to the edges by the glass/polymer. Solar cells installed at the edge of the wave-guide can harvest and convert the emitted energy to useable electricity, thereby creating an electricity generating window. Similarly to the CIGS thin films solar cells, LSCs can also be made as a thin film and share similar benefits to CIGS. Rapid implementation, up-scalable and lower manufacturing costs.

A key challenge for thin film based LSCs is the limited thickness available for absorption. What's more is that in order to achieve appreciable power conversion efficiencies of more than 1% requires absorption of both UV and the visible part of the spectrum [6]. This leads to other challenges such as unwanted colorization of the window. To mitigate the unwanted colorization of a window requires that the thin film absorbs across the entire visible spectrum or is color-balanced with complementary (luminescent) ions. Luminescent centers such as the trivalent rare-earths Nd3+ and Yb3+ have narrow and weak absorption properties due to their forbidden 4f-4f transitions and are therefore unsuitable for thin film LSC applications without a sensitizer. The selenide based CIGS however, with its broad and narrow-bandgap transition (absorption < 800 nm) and high absorption coefficient (> 1 x 105 cm<sup>-1</sup>), is able to absorb nearly all of the UV and visible part of the solar spectrum in just 1 micron [7]. The absorption properties of the CIGS type thin film material, combined with the luminescent properties of trivalent rare-earths would make an ideal candidate for a thin film LSC. The requirement is that the CIGS host can efficiently sensitize the trivalent rare-earth. Numerous work has been done on semiconductor quantum dots doped with trivalent lanthanides (Ln³+) [8-10]. To our knowledge, no work has been done on doping Ln³+ in CIGS type hosts in thin films for LSC applications. In this work we hypothesize an energy transfer mechanism between the CIGS host and Ln³+ doping and discuss its validity through experimental photoluminescence results on sputtered CuGaS₂:Yb³+ thin films.

## **Energy Transfer Mechanism**

Two well-known energy transfer mechanisms are presented by Forster (dipole-dipole interaction) and Dexter (exchange interaction) [11, 12]. Both of these interactions are strongly dependent on spectral overlap between a sensitizer and activator. Mukherjee et al. provide an elaborate discussion on why these two mechanisms are likely to be negligible for the sensitization of Tb<sup>3+</sup> and Eu<sup>3+</sup> in ZnS nanoparticles [13]. Instead, they describe a mechanism that involves the Ln<sup>3+</sup> acting as either an electron or hole trap followed by a recombination event at the lanthanide site leaving the Ln<sup>3+</sup> in an excited state.

The charge trapping mediated  $Ln^{3+}$  emission sensitization mechanism, as they call it [14, 15], can be modelled using the vacuum referred binding energy (VRBE) diagrams developed by P. Dorenbos [16-21]. These diagrams relate position of the valence and conduction band of the host to the ground and excited states of all divalent and trivalent lanthanides and thereby possibilities for electron and hole trapping. In **Fig. 5.1** such a diagram is presented to visualize the charge trapping mediated  $Ln^{3+}$  emission sensitization mechanism. The steps of the sensitization mechanism are described by the arrows and their corresponding equations listed below. **Fig. 5.1** serves as a conceptual diagram and therefore does not provide absolute energy values. More examples of such a diagram of ZnX and CdX (X = S, Se, Te), but with absolute energy values, can be found in the work by Mukherjee et al. [13] First an electron-hole pair is generated after the absorption of a photon with enough energy to cross the band-gap as shown by arrow 1, figure 1. If the  $Ln^{3+}$  dopant ground state lies above the host's valence band, then the dopant can act as a trap for a hole.

$$Ln^{3+} + h^+ \rightarrow [Ln^{3+} + h^+] \rightarrow Ln^{4+},$$
 (5.2a)

where the notation  $[Ln^{3+} + h^{+}]$  indicates a charge transfer (CT) state. The possibility of hole trapping is however limited to the ions Ce<sup>3+</sup>, Pr<sup>3+</sup> and Tb<sup>3+</sup>. The other lanthanides have their ground state below the valence band maximum. The coulomb interaction will localize an electron near the trapped hole and subsequent recombination can lead to Ln<sup>3+</sup> in the excited state.

$$Ln^{4+} + e^- \to Ln^{3+*}$$
 (5.2b)

The alternative host-to-Ln<sup>3+</sup> ion energy transfer route is electron trapping.

$$Ln^{3+} + e^- \rightarrow [Ln^{3+} + e^-] \rightarrow Ln^{2+}$$
 (5.3a)

Followed by hole trapping at the dopant site and again creation of the excited Ln<sup>3+</sup>

$$Ln^{2+} + h^{+} \to Ln^{3+*}$$
 (5.3b)

For electron trapping to happen it requires that the Ln<sup>2+</sup> ground state lies below the conduction band of the host which is most likely the case for ions like Eu<sup>2+</sup>, Sm<sup>2+</sup>, Yb<sup>2+</sup> and Tm<sup>2+</sup>. It is a misconception that excited 4f levels of Ln<sup>3+</sup> ions (given by a Dieke diagram) lying below the conduction band can be electron traps. These excited states are electron donor states, not acceptor states. Only by first trapping the hole, creating Ln<sup>4+</sup>, will the Ln<sup>3+</sup> ground and excited states act as electron acceptor states or electron traps.

It is generally more intuitive, due to common convention, to follow the path of electrons than holes. In case of an electron trapping process shown in on the left in **Fig. 5.1** (2b and 2c), it is straightforward to visualize an electron moving through the conduction band to the first available energy level of  $Tb^{3+}$  below the conduction band ( $Tb^{3+}$  is shown as an example). Note that the electron can only be trapped by  $Tb^{4+}$  which is formed after the hole has been trapped by the  $Tb^{3+}$  ion. When the electron recombines with the  $Tb^{4+}$  ion it leaves a  $Tb^{3+}$  ion in one of its excited states below the CB as indicated in **Fig. 5.1** and equation 2c. It is possible that the electron is first trapped in a 5d state of the  $Ln^{3+}$  ion or in a so-called Ln-trapped exciton state or impurity-trapped state (ITS)  $[Ln^{4+} + e^{-}]$  that can be visualized by the shifted parabola labelled ITS (shown by 2b, **Fig. 5.1**).

However, when an electron is trapped first by a Ln³+ ion, thereby creating Ln²+, it is difficult to visualize how one ends up with Ln³+ in the excited state after the hole recombines with Ln²+. P. Dorenbos provided a useful insight in 2018 through what he calls the 'hole picture' [22]. The hole picture provides a convenient way to follow the path of the hole and is sometimes used in semiconductor physics [23]. In a typical energy diagram, like **Fig. 5.1**, the electron moves up as it gains energy and moves down as it relaxes. Contrarily, holes move up as they relax and down as they are excited. The excited Ln³+ states can be visualized by flipping the Dieke diagram upside down and placed with the Ln³+ ground state at the Ln²+ ground state. Traditional configurational coordinate diagrams can again be used to represent the well-known charge transfer (CT) states (like that for Eu³+ or Yb³+) in which a hole is trapped at the anion states coordinating the Ln²+ ion. Taken together we have a clearer picture of the sensitization of a Yb³+ ions mediated by a charge trapping mechanism. After Yb²+ is formed there is a CT state available for the hole to relax to, situated above the valence band (shown by 3b). From this CT state it can relax further to the excited Yb³+ state (3c). Yb, the subject

of this paper, is used as an example of this mechanism. A similar process would be true for Eu.

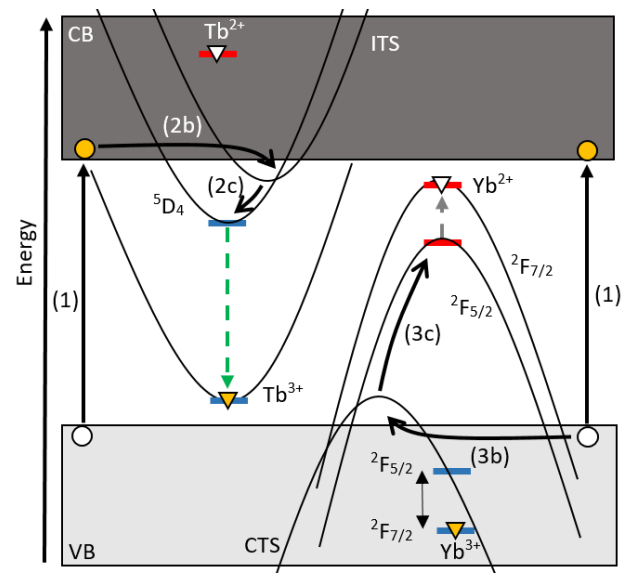


**Fig. 5.1.** A vacuum referred binding energy (VRBE) scheme along with configurational coordinate parabolas showing the proposed energy transfer mechanism. (1) generation of electron hole pair after photon absorption. (2b, 3b) electron or hole trapped by impurity-trapped state or charge transfer state respectively. (2c, 3c) electron or hole recombines with hole or electron respectively and leaves Ln<sup>3+</sup> in the excited state

The efficiency of the sensitization of the Ln³+ through this mechanism will be dependent on various parameters. First of all the electron and hole must have ample time to be trapped by the dopant. Therefore, the lifetime and mobility of the exciton must be sufficient to sensitize the Ln³+ dopant. What's more, considering the Yb³+ case, the Yb²+ ground state must not be situated too close to the conduction band as ionization can then be thermally activated where the electron escapes through the conduction band. Another quenching route can happen when the hole in the CTS can relax directly to the ground state, rather than to the excited state. Taken together, the position of the valence and conduction band relative to the Ln³+ dopant, the position of the CTS, and the intrinsic exciton properties of the host material are key parameters for the efficiency of the energy transfer in this mechanism.

It has been shown that these parameters can be tuned in CuGaS<sub>2</sub> by varying the Cu:Ga content [24]. Combinatorial sputtering allows to create thin films with a compositional gradient. With this method a CuGaS<sub>2</sub> thin film doped with Yb<sup>3+</sup> can be created that has a varying Cu:Ga ratio as a function of position on the film. Therefore, in the first part of this work a photoluminescence study on a composition gradient CuGaS<sub>2</sub>:Yb<sup>3+</sup> thin film with varying a Cu:Ga content and Yb concentration is presented. The second part

is a more detailed study, including x-ray diffraction, excitation spectra and temperature and time dependent luminescence is presented comparing three homogenous thin films with a Cu:Ga ratio of 0.95:1, 0.79:1 and 0.68:1. Finally a copy of the most efficient sample is post annealed in air and reinvestigated. More details on the synthesis of these films can be found in the experimental details section.

# 5.3 Experimental details

### **Fabrication of Thin Films**

A total of 4 samples were deposited on a 50x50x1 mm<sup>3</sup> fused silica substrate using an AJA ATC Orion 5 magnetron sputtering system. Sputtering was done in an argon atmosphere from three targets: CuGaS<sub>2</sub> (99.99%), Cu (99.9%), Yb (99.99%) (Demaco). It was found that sputtering from a single CuGaS<sub>2</sub> target resulted in a significant deviation from a 1:1 Cu:Ga ratio. Therefore, a Cu target was co-sputtered to compensate. It should be noted that others have done a study on the sputtering of Cu(InGa)Se<sub>2</sub> from a single target [25], however that is not the subject of this paper. The Cu target is connected to a pulsed direct current (DC) power supply, whilst the CuGaS2 and Yb targets are connected to radiofrequency (RF) power supplies. Prior to deposition the sputter chamber is evacuated to a base pressure in the order of 0.1 mPa. The working pressure during sputtering is 0.4 Pa with an argon gas flow of 15 sccm. Sputtering parameters used per sample can be seen in Table 5.3. The final three samples, S2, S3 and S4 were sputtered using a fresh CuGaS2 target. For this reason, there is a significant power difference on the CuGaS<sub>2</sub> targets between S1 and the others as the deposition rate was different for the two targets. The working distance between target and substrate is 10 cm. The three targets are at right angles from one another, where each target is aligned so that the highest deposition rate is located at edge of the substrate, in a sputter up configuration. To achieve doping concentrations (1%) of Yb a mask with holes is installed above the target to reduce deposition rates by roughly 90%. Similarly for Cu a mask was installed to reduce the deposition rate by roughly 60%. The substrate is heated at 250 °C during deposition. For S1 the substrate is not rotated to obtain a compositional gradient. The orientation of the film and the compositional gradient can be seen in Fig. 5.2b. The other films, S2, S3 and S4, are homogenous obtained by rotating the target with different Cu:Ga ratios obtained by having the Cu target at different powers. A schematic of the sputter coater can be seen in Fig. 5.2a. After deposition, each sample was post annealed in vacuum at 350 °C, according to an optimization study done by another group [26]. In an attempt to optimize the Yb<sup>3+</sup> intensity, one of the four pieces of the most emitting sample, S4, was post annealed in air for half an hour at 400 °C.

ID	Gradient	CuGaS <sub>2</sub> /Cu/Yb Power (W)	Deposition Time (s)
S1	Yes	110 / 30 / 15	10000
S2	No	180 / 40 / 15	7500
S3	No	180 / 20 / 15	8500
S4	No	180 / 0 / 10	11500

**Table 5.3.** Sputter deposition conditions of the samples.

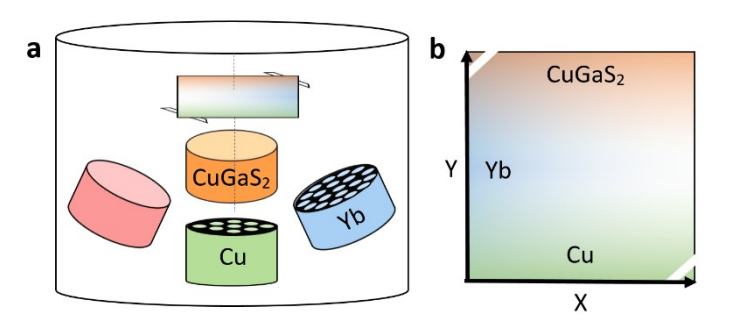


Fig. 5.2. a) Schematic of the sputter coater with the orientation of each source. b) Schematic of the gradient film (film side on top) where the colours represent a concentration gradient of the corresponding target.

#### Characterization of Thin Films

Energy-dispersive X-ray spectroscopy (EDS/EDX) measurements were done for 60 seconds using the JEOL JSM-IT100 EDX/SEM electron microscope at x1000 magnification with an acceleration voltage of 12 kV, probe current of 60% and in a low vacuum pressure of 35 Pa. For the homogenous films a total of 5 measurements were done on various positions on the film.

X-ray diffraction (XRD) measurements were performed with a fixed slit width of  $\frac{1}{2}$  cm for half an hour using the PANalytical X'pert Pro MPD diffractometer. The equipment consists of a Cu K $\alpha$  (1.54056 Å) anode which is operating at 45 kV and 40 mA.

Photoluminescence emission, excitation and lifetime measurements were done with an optical parametric oscillator OPO EKSPLA/NT230 laser as excitation source with a pulse duration of 3-6 ns FWHM. Excitation wavelength is tunable between 193 and 2600 nm. A beam splitter is used to re-direct part of the laser to the sample, whilst the transmitted part is read out by Thorlabs thermal power meter to correct for the power of the laser in excitation measurement mode. Appropriate cut-off filters were used to remove the laser observed in second order from emission measurements. Luminescence

is collected by an optical fiber connected to an Ocean Optics QE Pro (350 to 1100 nm) spectrometer for emission/excitation measurements. For lifetime measurements the optical fiber is connected to a Hamamatsu H10330A-75 (950 to 1700 nm sensitivity) photomultiplier tube both operating at 800V which is subsequently read out by a CAEN DT5724 digitizer after a trigger pulse from the EKSPLA laser. Transmission measurements were performed using an Avantes DH-S lamp which is a combination of a deuterium and a halogen lamp. The light is transported by an optical fiber and collimated to a spot (2 mm diameter) and subsequently collected by a focusing mirror and then transported through another optical fiber connected to and read out by the Ocean Optics QE65 Pro (230 to 900nm).

All measurements on the gradient film were performed by placing the sample on two translation stages at right angles with precise position read-out in order to analyze the sample on a 17x17 grid. EDS measurements for the gradient film are made along a vertical line with varying Cu:Ga ratios or a horizontal line for constant Cu:Ga ratios, but varying Yb concentration. This allows to correlate the compositions of the film directly to the film material properties. Further details on this method can be found in previous work [27].

Lastly, quantum efficiency measurements presented in this work are found using an integrating sphere with two optical fiber connectors, an LED at 375 nm with a full width at half maxima of 25 nm and the Ocean Optics QE Pro (350 to 1100 nm) spectrometer. A couple of optical fibres are used to couple the LED light into the integrating sphere whilst another is connected to the spectrometer. First a measurement is done with a substrate inside the integrating sphere. Then a measurement is taken with a substrate that has a thin film deposited. The difference in the LED intensity between the two measurements is taken as the absorption, whilst the difference in Yb<sup>3+</sup> emission (around 970 nm) is used as the emission intensity. Emission counts divided by absorption counts is used to estimate the quantum efficiency of the sample.

### 5.4 Results & Discussion

## **Gradient Thin Film**

An image of the S1 film is shown in **Fig. 5.3**. The orientation of the film is the same as depicted in **Fig. 5.2**b. The color of the film changes from a dark brown to a light yellow from the bottom (Cu rich) to the top (Cu poor). EDS measurements along the center vertical, indicated by circular white markers in **Fig. 5.3**, show that the Cu/Ga ratio ranges from 1.91 to 0.40 from bottom to top. The S/(Cu+Ga) ratio changes along this vertical between 0.84 and 1.10. The EDS and other results are summarized in **Table 5.4**. In **Fig. 5.4**b, XRD measurements done on Y = 5, 25 and 45 mm are presented and show that only the CuGaS<sub>2</sub> phase is present (JCPDS#25-0279). The Yb content ranged

between 0.33 and 0.75 % with an average of 0.53 %. There was no clear gradient of the Yb content along the vertical like for the Cu/Ga and S/(Cu+Ga) ratios, which is to be expected as the Yb source is at a right angle of the vertical. The Yb content is expressed as the percentage of all cations (Yb, Cu and Ga).

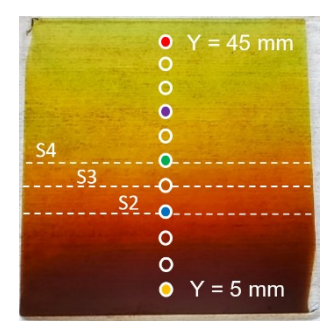


**Fig. 5.3.** Photograph of S1 with white circular markers to indicate where EDS measurements were done which are presented in **Table 5.4**. Transmission, XRD and (time-resolved) emission measurements (presented in **Fig. 5.4**a-b, 6 and 7) were recorded at the colored markers. The three white dashed lines indicate the position on the film where the Cu:Ga ratio represents that of the three homogenous films presented later.

In Fig. 5.4 the position dependent transmission and XRD measurements taken at the colored markers in Fig. 5.3 are presented. As the photo in Fig. 5.3 suggests, the absorption edge is blue shifted towards the top of the sample (Cu poor and S rich). A thin film interference pattern is observed at longer wavelengths (> 600 nm). Fitting the interference fringes with the Swanepoel method allows to estimate the film thickness and refractive index (defined at 589 nm) [28]. However, towards the bottom of the film (Y = 5 mm) the thin film interference is not observed, which does not allow for proper fitting of the fringes. The thickness increased from 630 nm to 950 nm and the refractive index decreased from 2.52 to 2.30 going from Y = 17 mm to Y = 45 mm. All fits had an R-square value higher than 0.99. The increase in thickness towards the top is expected due to the higher deposition rate of the CuGaS2 target at the top. The absorption edge shift can be attributed to the widening of the CuGaS<sub>2</sub> bandgap due to a deficiency in Cu, which is thought to be caused by a lowering of the valence band according to a previous study [24]. The XRD measurements shown in Fig. 5.4b are taken at positions Y = 5, 25 and 45 mm and are plotted on a logarithmic scale. All measurements have a broad peak at 22 degrees originating from the amorphous fused silica substrate. A single common peak is observed at 28 degrees related to the CuGaS<sub>2</sub> crystal structure. The peak decreases in intensity towards the top of the film, where the film becomes more deficient in Cu. Typically XRD of CuGaS<sub>2</sub> has 7 peaks between 20 and 60 degrees, with the main peaks at 28, 48 and 57 degrees (JCPDS#25-0279). However, thin films can be textured, which is a result of a preferred crystallite growth orientation during deposition. The bottom of the film (Y = 5 mm, in yellow) has a

second observed peak at 48 degrees also related to the CuGaS<sub>2</sub> structure. Other phases such as Cu, CuS, CuS2, CuO, Cu<sub>2</sub>O or Ga<sub>2</sub>S<sub>3</sub> where not observed. The gradient film can best be interpreted as an amorphous defect rich Cu<sub>x</sub>Ga<sub>y</sub>S<sub>2</sub> film with a varying fraction of CuGaS<sub>2</sub> crystallites.

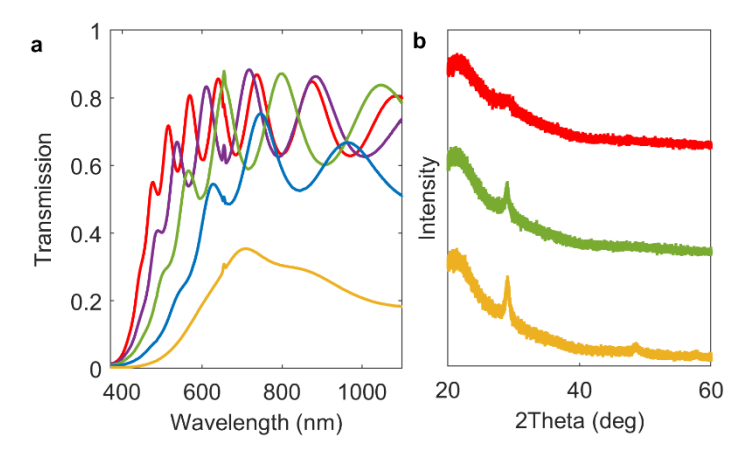


Fig. 5.4. Transmission spectra (a) and XRD diffractograms (b) of S1 taken at 5 (a) or 3 (b) positions on the film indicated by the colored markers shown in Fig. 5.3.

The transmission measurements presented in **Fig. 5.4**, along with the retrieved thickness using the Swanepoel method, can be used to estimate a band-gap value of our thin film using the Tauc method [29]. To apply the Tauc method a direct band-gap is assumed throughout the thin film. In **Fig. 5.5** the absorption coefficient, α (cm<sup>-1</sup>), is plotted against photon energy (eV) at the same positions as shown by the corresponding colored markers in **Fig. 5.3**. As per the Tauc method, the first linear region is extrapolated to intersect with the x-axis (shown by the dotted line). The value of the intersect is an estimation of the local band-gap of the material. The position-dependent band-gap values are summarized in **Table 5.4**. Similar difficulties as with the Swanepoel method prevent a band-gap estimation on the bottom side of the film.

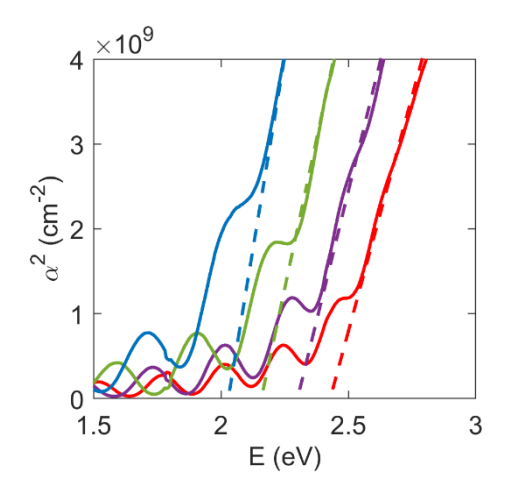
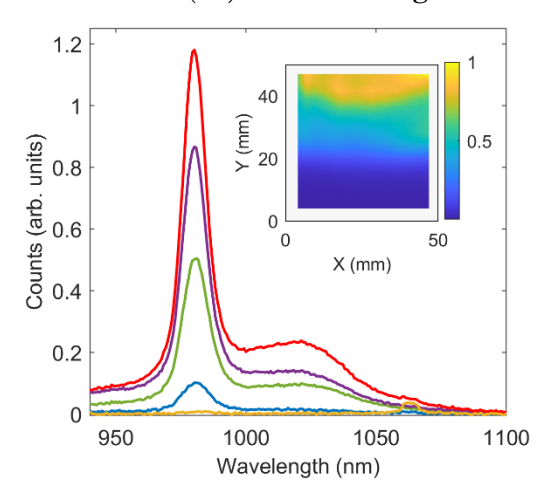


Fig. 5.5. Tauc plots of S1 at 4 positions on the film indicated by the colored markers shown in Fig. 5.3.

The Yb<sup>3+</sup> emission intensity ( $\lambda_{\rm exc}$  = 375 nm) has also been measured at the same points as the transmission measurements, shown in **Fig. 5.6**. The well-known  ${}^2F_{5/2} \rightarrow {}^2F_{7/2}$  4f-4f transition maximum of Yb<sup>3+</sup> is observed at 980 nm. The inset of **Fig. 5.6** shows heat map of the Yb<sup>3+</sup> intensity across the entire film. The Yb<sup>3+</sup> intensity heat map has a similar shape as that of the photo in **Fig. 5.3**. Comparing **Fig. 5.5** and **Fig. 5.6** it is clear that an increase in the band gap results in an increase of the Yb<sup>3+</sup> intensity. Close to no emission is observed at the bottom of the film, which is likely due to the low transmission at 980 nm of the film (0.2) as shown in **Fig. 5.4**a.



**Fig. 5.6.** Emission spectra ( $\lambda_{\rm exc}$  = 375 nm) of S1 taken at the same position as the transmission measurements (**Fig. 5.4**) indicated by the corresponding colored markers shown in **Fig. 5.3**. The inset shows a heat map of the integrated intensity of the 980 nm Yb<sup>3+</sup> emission taken at 17x17 positions and interpolated across the film.

Lastly, the time-resolved intensity of Yb<sup>3+</sup> ( $\lambda_{exc} = 375$ ,  $\lambda_{exm} = 980$  nm) was measured at the same positions as the transmission and emission measurements and are presented in **Fig. 5.7**. The decay of the  ${}^5F_{5/2}$  state of Yb<sup>3+</sup> is not mono-exponential. The lifetime is, therefore, calculated as a mean lifetime  $\tau_m$  which is defined as:

$$\tau_m = \frac{\int_0^\infty t * I_t(t)dt}{\int_0^\infty I_t(t)dt}$$
 (5.4)

where t is time after excitation (at t=0) and  $I_t(t)$  is the time-resolved luminescence intensity. The mean lifetime follows a trend similar to the intensity, where the mean lifetime increases from 2 to 37  $\mu$ s from the bottom to the top of the film. The multi-exponential behaviour of the Yb<sup>3+</sup> decay suggests that a large fraction of the Yb<sup>3+</sup> ions reside in the amorphous part of our samples causing a wide range of Yb<sup>3+</sup> ions close to or part of a defect, each with its own non-radiative rate. As will be discussed later in more detail (**Fig. 5.12**), it appears that the intrinsic and defect free decay time of Yb<sup>3+</sup> in CuGaS<sub>2</sub> is 110  $\mu$ s as shown by an exponential tail of the decay common to multiple samples.

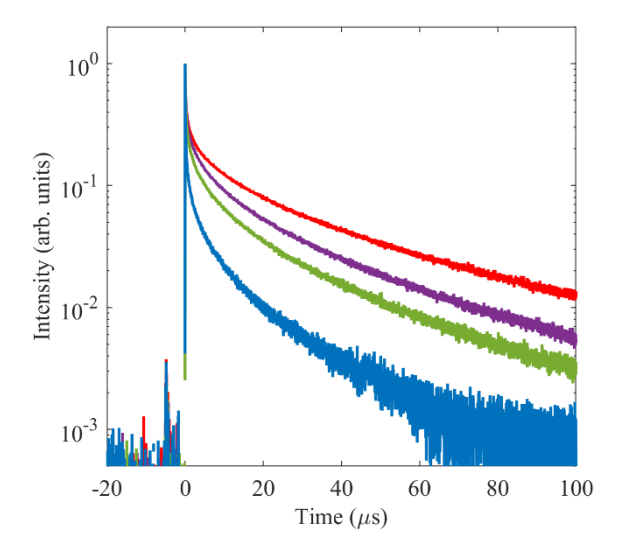


Fig. 5.7. Time resolved intensity measurements, normalized at t = 0, monitoring 980 nm of S1 taken at 4 positions on the film indicated by the corresponding colored markers in Fig. 5.3.

The position dependent EDS, transmission, emission and lifetime measurements of S1 demonstrate a trend that Yb<sup>3+</sup> finds a more suitable site in Cu-poor CuGaS<sub>2</sub> films. This is similar to the observed improved CuInGaSe<sub>2</sub> solar cell performance in Cu-poor films. The chief reason for improved solar cell efficiency in Cu-poor CuInGaSe<sub>2</sub> lies in the suppression of recombination events of the electron-hole pair for two reasons. First, Cu vacancies provide improved hole (the majority charge carrier in CIGS) conductance

and second, the valence band maximum is shifted to lower energies [30, 31]. These reasons can also play a role for the improved Yb<sup>3+</sup> intensity as they increase the lifetime and mobility of holes is beneficial for the energy transfer to Yb<sup>3+</sup> while a lower valence band makes excited Yb<sup>3+</sup> ions less prone to thermal quenching through the CTS. The role of the VB will be discussed in more detail in relation with the temperature dependent decay measurements. This quenching route becomes less efficient when the valence band is shifted downwards [32]. The data presented above including the composition, refractive index, thickness and estimated band-gap of the film and the intensity and mean decay time of Yb<sup>3+</sup> along the center vertical are summarized in **Table 5.4**.

**Table 5.4.** Position dependent composition, refractive index (n), thickness (d), band-gap ( $E_{bg}$ ), intensity (I) and mean lifetime  $\tau_{mean}$  of S1. Measurements are done at white circular markers shown in **Fig. 5.3**. Homogenous samples S2, S3 and S4 presented later have a similar Cu/Ga value at Y = 17, 21 and 25 mm respectively.

y (mm)	Cu/Ga	S/(Cu+Ga)	Yb (%)	n	d (nm)	E <sub>bg</sub> (eV)	I (arb. units)	$ au_{mean} (\mu s)$
45 (top)	0.40	1.10	0.6	2.32	940	2.42	0.95	44
41	0.41	1.09	0.4	2.35	890	2.37	1	38
37	0.47	1.08	0.5	2.36	840	2.32	0.85	34
33	0.50	1.08	0.5	2.38	790	2.28	0.68	31
29	0.58	1.07	0.7	2.40	750	2.20	0.57	26
25 (S4)	0.68	1.01	0.7	2.45	690	2.14	0.41	24
21 (S3)	0.81	0.98	0.8	2.53	650	2.09	0.3	20
17 (S2)	0.95	0.93	0.7	2.52	630	2.05	0.08	12
13	1.18	0.90	0.5				0.03	6
9	1.47	0.87	0.6				0.02	3
5 (bottom)	1.91	0.84	0.6				0.004	1

The position dependent intensity measurements presented in **Fig. 5.6** show that the intensity does not vary significantly across (from left to right) the film. Along the x-direction of the film the Cu, Ga and S content are constant whereas the Yb content varies continuously due to the geometry of the sputter coater as can be seen by the black square markers in **Fig. 5.8**. At Y = 17 mm the average Cu:Ga and S:(Cu+Ga) ratios were 0.94:1 and 0.92:1 with a standard deviation of 0.02 and 0.01 respectively. The Yb content decreases linearly from 1.3 to 0.4 % going from the left side to the right side of the sample.

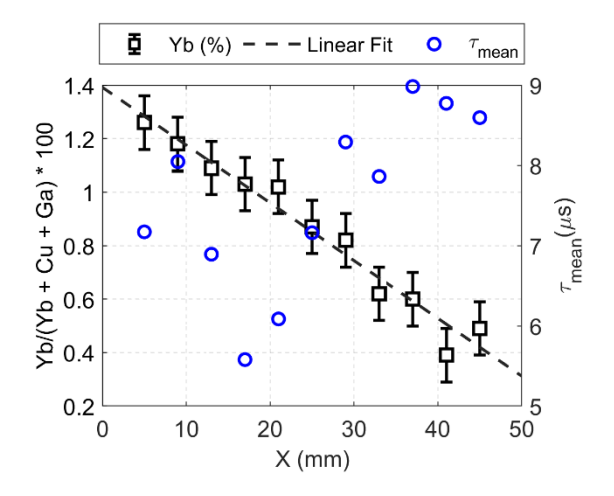


**Fig. 5.8.** Position dependent Yb content (black markers, left Y axis) across S1 where the film's composition is closest to stoichiometric CuGaS<sub>2</sub> (Y = 17 mm). The black dashed line is a linear fit of the Yb content and x position. Mean radiative lifetime (blue markers, right y axis) of Yb<sup>3+</sup> at the same positions along Y= 17 mm.

The Yb<sup>3+</sup> time-resolved intensity was measured ( $\lambda_{exc} = 375$ ,  $\lambda_{exm} = 980$  nm) along the same line as the EDS measurements. The mean lifetime of Yb<sup>3+</sup> was found to vary between 5.6 and 9.0 µs, with an average of 7.6 µs and a standard deviation of 1.1 µs. The mean lifetime versus X position is shown along the Yb content vs X in **Fig. 5.8**. Unlike the Yb content, no trend was observed in the mean lifetime as a function of X position along the Y = 17 mm horizontal. The lack of correlation between the Yb content and mean lifetime indicate that concentration quenching effects play an insignificant role at this range of Yb concentration (0.4 to 1.3 %, **Fig. 5.8**).

In this section we have presented and discussed the nature of Yb³+ luminescence in a gradient CuGaS₂ film. It is clear that a wider band-gap, Cu-deficient CuGaS₂ film is beneficial for the Yb³+ efficiency. However, the exact reason for this is still unclear. Temperature dependent photoluminescence measurements can provide useful data to deepen the understanding of the energy transfer mechanism. To conduct such measurements, it is not feasible to do so on gradient thin films due to experimental limitations. In the next section a comparison is made between four homogenous CuGaS₂:Yb films with different Cu:Ga ratios, but a similar thickness and S and Yb content. Temperature dependent lifetime and emission intensity measurements and a low temperature excitation measurement are presented to investigate any thermally activated quenching routes present. Finally, a quantum efficiency measurement at room temperature gives an indication on the energy transfer efficiency of the mechanism presented.

#### Homogenous Thin Films

Four homogenous films, S2, S3, S4 and S4-PA are presented in **Fig. 5.9**. The S4-PA sample is a part of the S4 sample which was post annealed (PA) in air for 30 minutes at 400 °C. EDS measurements are presented in **Table 5.5**. The Cu:Ga ratio is 0.95:1, 0.83:1, 0.74:1 and 0.75:1 for S2, S3, S4 and S4-PA respectively. The Yb cation content is approximately 0.3 % for all four samples. The O content in S2, S3 and S4 is around 3.5 %. However, it cannot be excluded that some oxygen EDX signal originated from the substrate. Upon annealing we see that S4-PA has an O content of 14.2 %, while de S content has decreased by roughly the same value, indicating that roughly 20 % of our S is replaced by O after annealing.



Fig. 5.9. Photo of the four homogenous samples

Table 5.5. Composition of samples S2, S3, S4 and S4-PA given in atomic percentages

	Cu (%)	Ga (%)	S (%)	O (%)	Yb (%)
S2	23.6	24.4	48.8	3.0	0.2
S3	22.3	26.9	46.7	4.0	0.1
S4	21.0	28.5	46.7	3.7	0.1
S4-PA	20.6	27.5	37.6	14.2	0.1

Transmission measurements, shown in **Fig. 5.10**a, were once again fitted using the Swanepoel method to retrieve the thickness and refractive index. The thickness is found to be 830, 890, 1060 and 1060 nm and the refractive index 2.51, 2.45, 2.40 and 2.38 for S2, S3, S4 and S4-PA respectively. The values for the refractive index follow the same trend as the gradient film, namely a lower Cu:Ga ratio leads to a smaller refractive index. The annealing of S4 in oxygen resulted in a slightly lower refractive index as some sulphur is replaced by oxygen. For samples S2 and S3 we note that the maxima of the interference fringes decreases at longer wavelengths, whereas for S4 and S4-PA this is not the case. The key interest for this work is the slight shifting of the absorption edge between the four samples and how this affects the Yb<sup>3+</sup> luminescence. It can be concluded that the properties of the homogeneous films are largely identical to the indicated locations at the gradient film as intended.

XRD measurements showed characteristic CuGaS<sub>2</sub> peaks. Results are shown in **Fig. 5.10**b. Once again a single peak is observed at 28 degrees, like in the gradient film. We note that the Cu-rich film, S2, has a second peak at 48 degrees which is not present in

the other measurements, despite S4 and S4-PA having a higher peak intensity at 28 degrees. This can be due to S2 being less textured and having more random orientations, rather than one single orientation. Similar to the gradient films, other phases such as Cu, CuS, CuS<sub>2</sub>, CuO, Cu<sub>2</sub>O or Ga<sub>2</sub>S<sub>3</sub> were not observed. The post annealing of S4 did not significantly improve the crystallinity in terms of observed intensity. There is a slight shift in the peak of 0.1 degrees to the right, likely due to the incorporation of the smaller O ion in the lattice. Previous work has shown a CuO phase developing after post annealing CuGaS<sub>2</sub> thin films for 2 hours at 400 °C [33]. We do not find such a phase present in our sample.

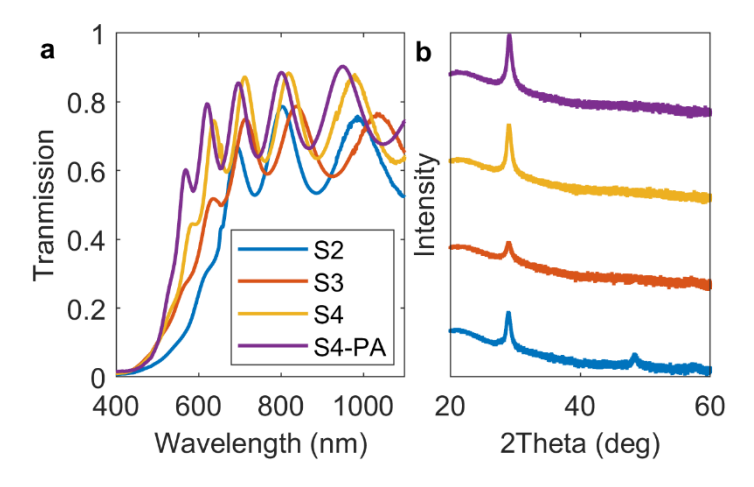


Fig. 5.10. Transmission (a) and XRD (b) measurements of S2, S3, S4 and S4 – PA.

Emission ( $\lambda_{\rm exc}$  = 375 nm) of the four samples is shown in **Fig. 5.11**. We can see that luminescence intensity is increased substantially from S2 to S4 – PA. Between S2 and S4 the intensity is improved by roughly 25 times. We do not observe this significant increase in intensity within the gradient film (between Y = 17 and 25 mm). After post annealing S4, the intensity is further increased by a factor of 15. These results show that Yb<sup>3+</sup> luminescence is strongly affected by the Cu:Ga ratio and the incorporation of O. A shift of the peak intensity of Yb<sup>3+</sup> between S3 and S4 of about 1.5 nm is observed, indicating that the site at which Yb<sup>3+</sup> is located is affected by the Cu:Ga ratio.

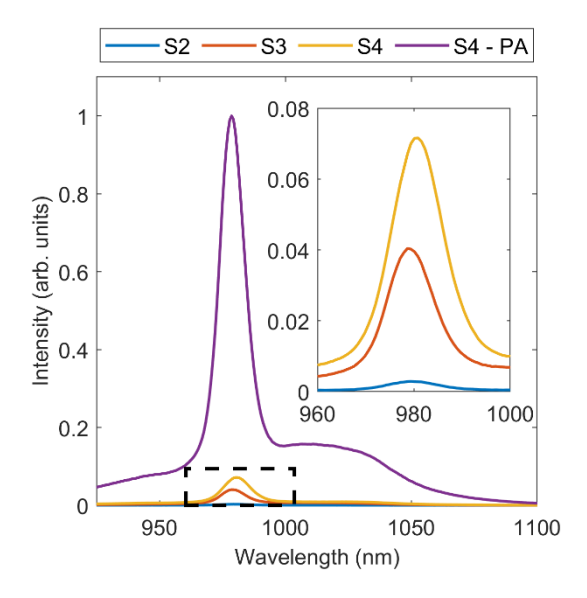
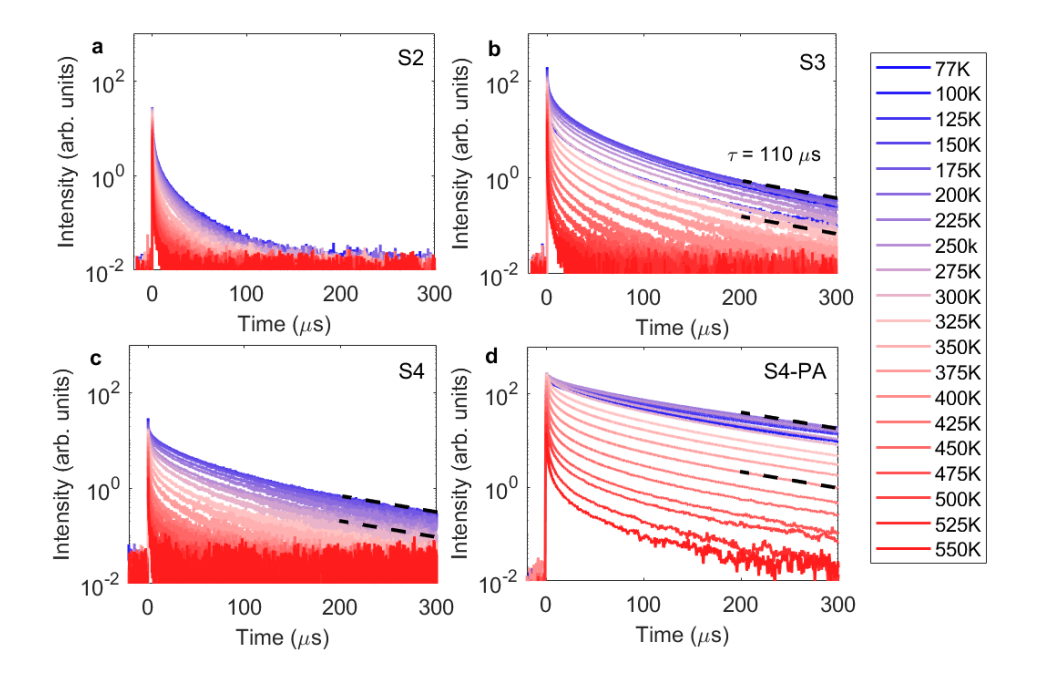


Fig. 5.11. Emission intensity of Yb<sup>3+</sup> ( $\lambda_{exc}$  = 375) of S2, S3, S4 and S4 – PA at room temperature

Temperature dependent lifetime measurements at  $(\lambda_{exc} = 375, \lambda_{exm} = 980 \text{ nm})$  are shown in Fig. 5.12a-d. The same intensity- and time scale are chosen on the axis to be able to compare the shape of the decay curves between the samples. The same number of laser pulses were used at each temperature and the decay curves are plotted as measured and not normalized to unity. The intensity differences at t=0 between samples is caused mainly by alignment differences between laser, sample and detector. That is why S2 shows a relatively poor intensity. For comparing intensities between samples Fig. 5.11 should be used. The tail of the emission for S3, S4 and S4-PA can reasonably well be approximated with a single exponential with a decay time of 110 µs, as shown by the dashed black lines, that does not change with temperature. Yb3+ lifetime in sulfides ranges between 1.2 ns up to 400 µs in MoS<sub>2</sub>:Yb<sup>3+</sup> and PbIn<sub>2</sub>S<sub>4</sub>:Yb<sup>3+</sup> respectively [34, 35]. While in CdSe:Yb<sup>3+</sup> quantum dots exhibit a Yb<sup>3+</sup> lifetime up to 160 µs [10]. The observed lifetime of 110 µs in our CuGaS2:Yb3+ thin film fits within this range, though relatively short. No literature data is found on Yb<sup>3+</sup> lifetime in materials with a chalcopyrite structure. The variation in Yb<sup>3+</sup> lifetime in chalcogenides is influenced by composition, crystallinity and structure and therefore a comparison of Yb3+ lifetime is difficult to do between compounds. The lowering of the integrated intensity towards higher temperature is due to an increasingly larger contribution of a fast nonexponential component. Although our samples show complex non-exponential behavior, it is possible to derive a number of conclusions from a qualitative analysis. For this we discriminate between two different situations: the first is a classical situation in which the decay curves become steeper toward higher temperature due to a

temperature dependent quenching of excited Yb³+ ions. In such a situation decay curves have a constant intensity at t=0. In a second situation, excited Yb³+ ions have no temperature-dependent quenching but rather a temperature dependent host-to-Yb³+ energy transfer. In that case decay curves have a constant slope but the intensity at t=0 decreases towards higher temperature. In both cases an energy barrier  $\Delta E$  controls the temperature dependence. The constant slope of the decay tails of all our samples suggests the second situation is predominantly active. As indicated by the two parallel dashed lines in each graph for S3, S4 and S4-PA, the slope of the tail of the decay curves does not change significantly with temperature and remains about 110  $\mu$ s for the three samples. This decay time is therefore interpreted as the intrinsic decay time of Yb³+ in this sulfide host without any defects.



**Fig. 5.12.** Temperature dependent (77 to 550 K) time resolved Yb<sup>3+</sup> emission ( $\lambda_{exc} = 375$ ,  $\lambda_{exm} = 980$  nm) of S2, S3, S4 and S4-PA shown in (a), (b), (c) and (d) respectively. The arrow in (a) is shown to indicate increasing temperature and has been omitted in (b), (c), and (d) for clarity. The tail of the emission is fitted with a single exponential in (b), (c) and (d) indicated by the black dashed line.

No exciton emission from the host is observed at 77 K, unlike other reports in CuGaS<sub>2</sub> crystals [36]. The lack of exciton emission suggests that there is an efficient and fast non-radiative recombination of the hole and electron after excitation. A low lifetime of electron-hole pairs would be detrimental to the energy transfer mechanism. We also

note the presence of slower decaying Yb<sup>3+</sup> ions present in the S4-PA sample. Temperatures below room temperature show a clear slow decaying component with a lifetime of approximately 1.4 ms, indicated again by a dashed black line shown in **Fig. 5.13**. This decay time is similar to Yb<sup>3+</sup> ions found in oxide materials [37]. The significantly longer lasting decay component does not explain the higher emission intensity of S4-PA as the intensity has already dropped by two orders of magnitude by the time the slow component becomes visible, thereby not contributing significantly towards the overall emission intensity. Rather the annealing is likely to improve energy transfer efficiency by reducing defects in the host material and with that increase the emission intensity.

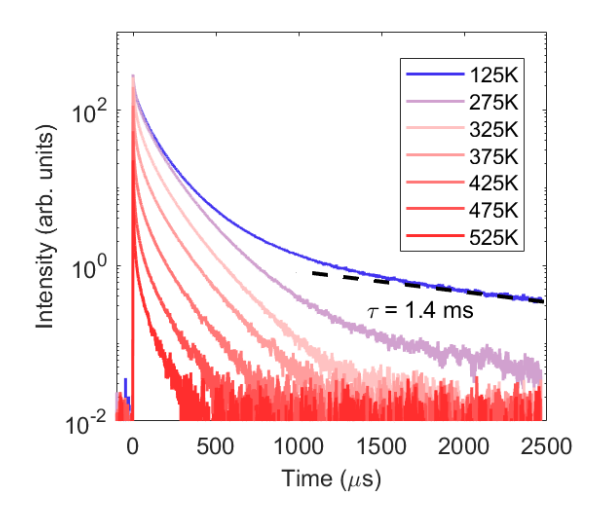


**Fig. 5.13.** Temperature dependent time resolved intensity of Yb<sup>3+</sup> ( $\lambda_{exc} = 375$ ,  $\lambda_{exm} = 980$  nm) in S4-PA. The tail of the emission at 125 K is fitted with a single exponential indicated by the black dashed line.

The temperature dependent intensity of Yb<sup>3+</sup> for S2, S3, S4 and S4-PA is found by integrating the time-resolved emission intensity in **Fig. 5.12**. To find an activation energy related to the observed thermal quenching, an Arrhenius plot is made. The Arrhenius equation is defined as follows:

$$I_{(T)} = \frac{I_0}{1 + A * e^{-\frac{\Delta E}{kT}}}$$
 (5.5)

where A is a pre-exponential factor,  $\Delta E$  is the activation energy, k the Boltzmann constant, T the temperature and  $I_0$  the intensity at T=77 K. Based on this equation one can plot  $\ln(I_0/I_T-1)$  vs 1/kT and obtain a linear relationship where the slope is equal to the activation energy. Two such plots, with linear fits, for S2 and S4-PA are shown in **Fig. 5.14**, the others are omitted for clarity. The activation energies for S2,

S3, S4 and S4-PA are found to be 0.15, 0.22, 0.20 and 0.28 eV respectively. As mentioned before, the temperature quenching appears to be due to a reduction in the number of Yb<sup>3+</sup> ions that get excited after transfer from the host lattice. In the proposed energy transfer mechanism, reviewed in the introduction, the first step to excite Yb<sup>3+</sup> is by trapping the electron in the Yb<sup>2+</sup> ground state. The de-trapping of the electron is thermally activated and would result in less excited Yb<sup>3+</sup> ions and thereby a lower intensity. The activation energy found using the Arrhenius plot therefore represents the energy difference between the Yb<sup>2+</sup> ground state and the bottom of the conduction band better known as the electron trap depth. A more detailed analysis of the fast component is beyond the scope of this work because the intensity at t = 0 is prone to experimental error due to the limited temporal resolution (bin size) of 1 ns of our measurements which determines the intensity at t = 0.

The Yb<sup>2+</sup> ground state generally resides at -3.5 eV on the vacuum referred binding energy scale which suggests that the conduction band lies around -3.3 eV which is very similar to previously measured values based on electrochemical techniques studies [38, 39]. For LSC application considerations, a larger trap depth would avoid significant thermal quenching at room temperature. This could be the case for CuAlS<sub>2</sub> that is known to have a higher energy CB. In our most efficient sample, S4-PA, we find that at room temperature the intensity is lower by a factor of 0.56 compared to at 77K.

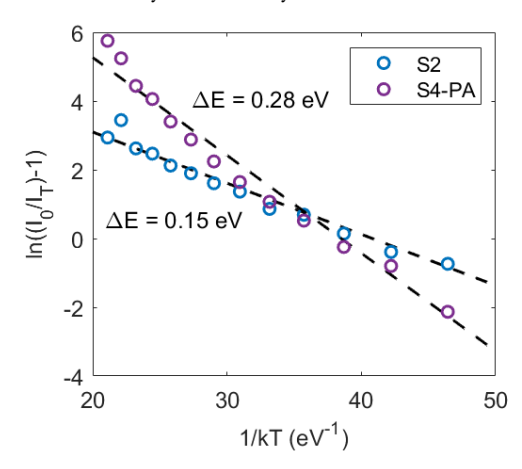


**Fig. 5.14.** Arrhenius plot showing the emission intensity plotted against 1/kT for S2, S3, S4 and S4-PA. The black dashed line is a fit using the Arrhenius equation (**5.5**).

Lastly, we present the transmission, excitation and emission spectra of our most optimal sample, S4 – PA, in a single plot (**Fig. 5.15**). It is expected that the excitation spectra consist of two main features. First is the excitation through the proposed mechanism which involves the creation of an electron-hole pair in the host (band-gap excitation) and the other would be a direct excitation of Yb<sup>3+</sup> through a charge transfer transition. The excitation spectrum we present has numerous features which makes it

difficult to interpret. We note a peak (split in two) around 483 nm, or 2.57 eV. This peak corresponds to the start of the absorption edge shown by the transmission spectra indicating that this is the band-gap. 2.57 eV is a slightly higher energy than the reported band-gap of 2.43 eV for  $CuGaS_2$  [40] and could be a result due to the incorporated O. However a larger band-gap is expected for S4-PA as it is deficient in Cu and post annealed in air. Using the 0.28 eV electron trap depth found earlier, we can estimate that the charge transfer energy (i.e. the distance between the valence band edge and Yb<sup>2+</sup> ground state) is 2.57 – 0.28 = 2.29 eV, or 541 nm. Again, due to the numerous broad peaks present in the measurement it is unclear if we truly observe the charge transfer transition. The quantum efficiency (QE) of S4 – PA was found to be of the order of 0.01% when excited by a 375 nm LED with a full width at half maxima of 25 nm. It was not feasible to measure the QE of the other samples as they were simply too dim.

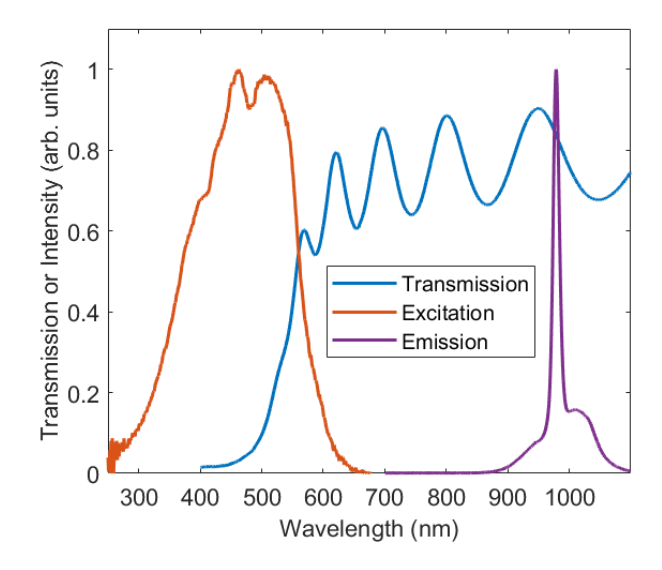


**Fig. 5.15.** Excitation and emission spectra ( $\lambda_{\text{exc}} = 375$ ,  $\lambda_{\text{exm}} = 980$  nm) of S4 – PA at 77K. Transmission measurement taken at room temperature.

Taking the activation energy,  $\Delta E$ , found from the Arrhenius plot along with the suggested band-gap,  $E_{gap}$ , found from the excitation and transmission measurements we can construct a VRBE scheme as shown in **Fig. 5.16**. The route of the hole is depicted once again to show the energy transfer mechanism as discussed in the introduction.

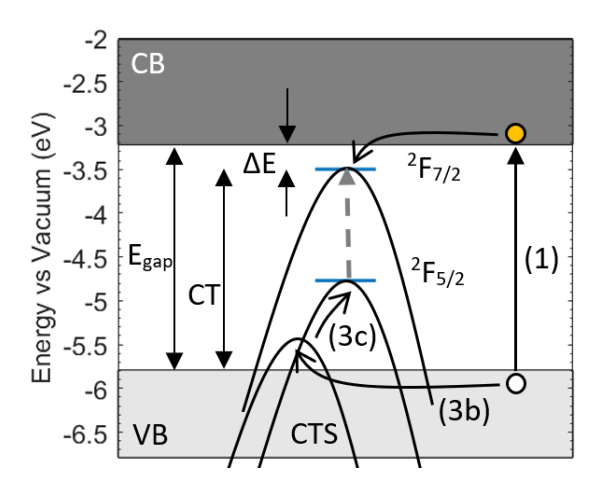


**Fig. 5.16.** Proposed VRBE diagram of CuGaS<sub>2</sub>:Yb<sup>3+</sup> (S4-PA) using the values for the activation energy ( $\Delta E$ ) for luminescence quenching and the band-gap ( $E_{gap}$ ) found experimentally. Parabolas are placed in the context of the 'hole picture' discussed in the introduction.

#### 5.5 Conclusion

It has been shown, using a gradient sputtering method, that the widening of the band-gap of CuGaS<sub>2</sub> towards a larger Cu-deficiency, increases the Yb<sup>3+</sup> emission intensity by 25 fold. This was explained by an more efficient hole transport (to Yb<sup>2+</sup>), a well-known effect in CuInGaSe<sub>2</sub> solar cells [30]. Post-annealing in air did not increase the crystallinity but resulted in a 15 times higher intensity most likely related to incorporation of 15% O ions.

The role played by oxygen needs to be investigated further. Temperature dependent decay curves of Yb<sup>3+</sup> emission indicate a single energy barrier varying between 0.15 to 0.28 eV depending on composition, that is interpreted as the energy of the Yb<sup>2+</sup> ground state below the conduction band. The thermal release of trapped electrons causes the intensity at room temperature to be 0.56 times lower than without thermal quenching at 77K. The unexpectedly low QE of 0.01% must however be explained by a more severe quenching process involving many non-radiative decay pathways of the generated electron-hole pairs due to the non-stoichiometric defective amorphous nature of the films. Just 1 in 10.000 electrons are trapped by Yb<sup>3+</sup>. It is concluded that the energy transfer is due to electron trapping, followed by hole-trapping. After hole trapping, excited Yb<sup>3+</sup> ions show no further quenching evidenced by a temperature independent decay tail of 110 μs. Although the strong and UV-VIS absorber characteristics of CuGaS<sub>2</sub> are favourable for LSC application, the poor energy transfer to Yb<sup>3+</sup> is obviously not. The temperature dependent quenching at room temperature can be mitigated by for example replacing Ga with Al, lifting the CB [41]. It remains to

be seen whether increasing the quality of the films can lower the electron-hole non-radiative recombination sufficiently. Overall, it can be concluded that the tune-ability of Cu(Al,Ga,In)(S,Se,Te)<sub>2</sub> along with the gradient thin film approach allows for fascinating research into the nature of the energy transfer mechanisms from the host to lanthanide or transition metal ions.

#### 5.6 References

- [1] L. L. Kazmerski, F. R. White, and G. K. Morgan, "Thin-film CuInSe2/CdS heterojunction solar cells," *Applied Physics Letters*, vol. 29, no. 4, pp. 268-270, 1976, doi: 10.1063/1.89041.
- [2] J. Gifford. (2015) Solar Frontier hits 22.3% on CIGS cell. pv magazine. Available: https://www.pv-magazine.com/2015/12/08/solar-frontier-hits-22-3-on-cigs-cell 100022342/
- [3] T. D. Lee and A. U. Ebong, "A review of thin film solar cell technologies and challenges," Renewable and Sustainable Energy Reviews, vol. 70, pp. 1286-1297, 2017, doi: 10.1016/j.rser.2016.12.028.
- [4] W. H. Weber and J. Lambe, "Luminescent greenhouse collector for solar radiation," Appl. Opt., vol. 15, no. 10, pp. 2299-2300, 1976/10/01 1976, doi: 10.1364/AO.15.002299.
- [5] M. Rafiee, S. Chandra, H. Ahmed, and S. J. McCormack, "An overview of various configurations of Luminescent Solar Concentrators for photovoltaic applications," *Optical Materials*, vol. 91, pp. 212-227, 2019, doi: 10.1016/j.optmat.2019.01.007.
- [6] B. C. Rowan, L. R. Wilson, and B. S. Richards, "Advanced Material Concepts for Luminescent Solar Concentrators," *IEEE Journal of Selected Topics in Quantum Electronics*, vol. 14, no. 5, pp. 1312-1322, 2008, doi: 10.1109/jstqe.2008.920282.
- [7] H. Li *et al.*, "Engineering CIGS grains qualities to achieve high efficiency in ultrathin Cu(InxGa1-x)Se2 solar cells with a single-gradient band gap profile," *Results in Physics*, vol. 12, pp. 704-711, 2019, doi: 10.1016/j.rinp.2018.12.043.
- [8] D. A. Chengelis, A. M. Yingling, P. D. Badger, C. M. Shade, and S. Petoud, "Incorporating Lanthanide Cations with Cadmium Selenide Nanocrystals: A Strategy to Sensitize and Protect Tb(III)," Journal of the American Chemical Society, vol. 127, no. 48, pp. 16752-16753, 2005/12/01 2005, doi: 10.1021/ja0511725.
- [9] W. Luo, R. Li, and X. Chen, "Host-Sensitized Luminescence of Nd3+ and Sm3+ Ions Incorporated in Anatase Titania Nanocrystals," *The Journal of Physical Chemistry C*, vol. 113, no. 20, pp. 8772-8777, 2009/05/21 2009, doi: 10.1021/jp901862k.
- [10] R. Martin-Rodriguez, R. Geitenbeek, and A. Meijerink, "Incorporation and luminescence of Yb3+ in CdSe nanocrystals," J Am Chem Soc, vol. 135, no. 37, pp. 13668-71, Sep 18 2013, doi: 10.1021/ja4077414.
- [11] T. Förster, "Zwischenmolekulare Energiewanderung und Fluoreszenz," *Annalen der Physik*, vol. 437, no. 1-2, pp. 55-75, 1948, doi: 10.1002/andp.19484370105.
- [12] D. L. Dexter, "A Theory of Sensitized Luminescence in Solids," *The Journal of Chemical Physics*, vol. 21, no. 5, pp. 836-850, 1953, doi: 10.1063/1.1699044.
- [13] P. Mukherjee, C. M. Shade, A. M. Yingling, D. N. Lamont, D. H. Waldeck, and S. Petoud, "Lanthanide sensitization in II-VI semiconductor materials: a case study with terbium(III) and europium(III) in zinc sulfide nanoparticles," *J Phys Chem A*, vol. 115, no. 16, pp. 4031-41, Apr 28 2011, doi: 10.1021/jp109786w.
- [14] G. H. Debnath, S. Rudra, A. Bhattacharyya, N. Guchhait, and P. Mukherjee, "Host sensitized lanthanide photoluminescence from post-synthetically modified semiconductor nanoparticles depends on reactant identity," *J Colloid Interface Sci*, vol. 540, pp. 448-465, Mar 22 2019, doi: 10.1016/j.jcis.2019.01.034.
- [15] G. H. Debnath, P. Mukherjee, and D. H. Waldeck, "Optimizing the Key Variables to Generate Host Sensitized Lanthanide Doped Semiconductor Nanoparticle Luminophores," *The Journal of Physical Chemistry C*, vol. 124, no. 49, pp. 26495-26517, 2020, doi: 10.1021/acs.jpcc.0c07548.
- [16] P. Dorenbos, "Systematic behaviour in trivalent lanthanide charge transfer energies," *Journal of Physics: Condensed Matter*, vol. 15, no. 49, p. 8417, 2003.
- [17] P. Dorenbos, "Locating lanthanide impurity levels in the forbidden band of host crystals," *Journal of Luminescence*, vol. 108, no. 1-4, pp. 301-305, 2004.
- [18] P. Dorenbos, "The Eu3+ charge transfer energy and the relation with the band gap of compounds," *Journal of Luminescence*, vol. 111, no. 1, pp. 89-104, 2005/01/01/ 2005, doi: https://doi.org/10.1016/j.jlumin.2004.07.003.

- [19] P. Dorenbos and E. van der Kolk, "Location of lanthanide impurity levels in the III-V semiconductor GaN," *Applied Physics Letters*, vol. 89, no. 6, 2006, doi: 10.1063/1.2336716.
- [20] P. Dorenbos and E. van der Kolk, "Location of lanthanide impurity energy levels in the III–V semiconductor AlxGa1−xN (0≤x≤1)," *Optical Materials*, vol. 30, no. 7, pp. 1052-1057, 2008/03/01/2008, doi: https://doi.org/10.1016/j.optmat.2007.05.019.
- [21] P. Dorenbos, "Lanthanide charge transfer energies and related luminescence, charge carrier trapping, and redox phenomena," *Journal of Alloys and Compounds*, vol. 488, no. 2, pp. 568-573, 2009/12/04/2009, doi: https://doi.org/10.1016/j.jallcom.2008.09.059.
- [22] P. Dorenbos, "The hole picture as alternative for the common electron picture to describe hole trapping and luminescence quenching," *Journal of Luminescence*, vol. 197, pp. 62-65, 2018, doi: 10.1016/j.jlumin.2018.01.013.
- [23] R. Heitz et al., "Excited states of Fe 3+ in GaN," Physical Review B, vol. 55, no. 7, p. 4382, 1997.
- [24] C. Guillén and J. Herrero, "CuInS2 and CuGaS2 thin films grown by modulated flux deposition with various Cu contents," physica status solidi (a), vol. 203, no. 10, pp. 2438-2443, 2006, doi: 10.1002/pssa.200622132.
- [25] S. M. Kong, R. Fan, S. H. Jung, and C. W. Chung, "Characterization of Cu(In,Ga)Se2 thin films prepared by RF magnetron sputtering using a single target without selenization," *Journal of Industrial and Engineering Chemistry*, vol. 19, no. 4, pp. 1320-1324, 2013/07/25/ 2013, doi: https://doi.org/10.1016/j.jiec.2012.12.035.
- [26] W.-J. Jeong and G.-C. Park, "Structural and electrical properties of CuGaS2 thin films by electron beam evaporation," *Solar Energy Materials and Solar Cells*, vol. 75, no. 1, pp. 93-100, 2003/01/01/ 2003, doi: https://doi.org/10.1016/S0927-0248(02)00110-1.
- [27] E. P. J. Merkx and E. van der Kolk, "Method for the Detailed Characterization of Cosputtered Inorganic Luminescent Material Libraries," ACS Combinatorial Science, vol. 20, no. 11, pp. 595-601, 2018/11/12 2018, doi: 10.1021/acscombsci.8b00068.
- [28] R. Swanepoel, "Determination of the thickness and optical constants of amorphous silicon," *Journal of Physics E: Scientific Instruments*, vol. 16, no. 12, p. 1214, 1983/12/01 1983, doi: 10.1088/0022-3735/16/12/023.
- [29] J. Tauc, "Optical properties and electronic structure of amorphous Ge and Si," *Materials research bulletin*, vol. 3, no. 1, pp. 37-46, 1968.
- [30] T. Nishimura, K. Nakada, and A. Yamada, "Examination of a Cu-Deficient Layer on Cu(In, Ga)Se2 Films Fabricated by a Three-Stage Process for Highly Efficient Solar Cells," ACS Applied Energy Materials, vol. 2, no. 7, pp. 5103-5108, 2019/07/22 2019, doi: 10.1021/acsaem.9b00774.
- [31] T. Maeda, W. Gong, and T. Wada, "Crystallographic and optical properties and band structures of CuInSe 2, CuIn 3 Se 5, and CuIn 5 Se 8 phases in Cu-poor Cu 2 Se–In 2 Se 3 pseudo-binary system," *Japanese Journal of Applied Physics*, vol. 55, p. 04ES15, 04/01 2016, doi: 10.7567/JJAP.55.04ES15.
- [32] P. Dorenbos, "Thermal quenching of lanthanide luminescence via charge transfer states in inorganic materials," *Journal of Materials Chemistry C*, 2023.
- [33] F. Smaïli and M. Kanzari, "Effect of oxygen on the surface morphology of CuGaS2 thin films," *Materials Science and Engineering: C,* vol. 29, no. 6, pp. 1969-1973, 2009/08/01/ 2009, doi: https://doi.org/10.1016/j.msec.2009.03.013.
- [34] S. E. Creutz, R. Fainblat, Y. Kim, M. C. De Siena, and D. R. Gamelin, "A selective cation exchange strategy for the synthesis of colloidal Yb3+-doped chalcogenide nanocrystals with strong broadband visible absorption and long-lived near-infrared emission," *Journal of the American Chemical Society*, vol. 139, no. 34, pp. 11814-11824, 2017.
- [35] C. Maddi et al., "Structural, Spectroscopic, and Excitonic Dynamic Characterization in Atomically Thin Yb3+-Doped MoS2, Fabricated by Femtosecond Pulsed Laser Deposition," Advanced Optical Materials, vol. 7, no. 21, p. 1900753, 2019.
- [36] S. Shirakata, K. Saiki, and S. Isomura, "Excitonic photoluminescence in CuGaS2 crystals," *Journal of Applied Physics*, vol. 68, no. 1, pp. 291-297, 1990, doi: 10.1063/1.347131.

- [37] Q. H. Yang, J. Ding, H. W. Zhang, and J. Xu, "Investigation of the spectroscopic properties of Yb3+-doped yttrium lanthanum oxide transparent ceramic," *Optics Communications*, vol. 273, no. 1, pp. 238-241, 2007/05/01/ 2007, doi: https://doi.org/10.1016/j.optcom.2006.12.035.
- [38] C. Li, J. He, Y. Xiao, Y. Li, and J.-J. Delaunay, "Earth-abundant Cu-based metal oxide photocathodes for photoelectrochemical water splitting," *Energy & Environmental Science*, vol. 13, no. 10, pp. 3269-3306, 2020.
- [39] P. Dorenbos, "[INVITED] Improved parameters for the lanthanide 4f and 4f-5d curves in HRBE and VRBE schemes that takes the nephelauxetic effect into account," *Journal of Luminescence*, vol. 222, p. 117164, 2020/06/01/ 2020, doi: https://doi.org/10.1016/j.jlumin.2020.117164.
- [40] J. Shay, P. Bridenbaugh, and H. Kasper, "Luminescent properties of CuGaS2 doped with Cd or Zn," Journal of Applied Physics, vol. 45, no. 10, pp. 4491-4494, 1974.
- [41] M. Caglar, S. Ilican, and Y. Caglar, "Structural, morphological and optical properties of CuAlS2 films deposited by spray pyrolysis method," *Optics Communications*, vol. 281, no. 6, pp. 1615-1624, 2008.

# 6 Summary, Concluding Remarks and Recommendations

The goal of the past four years was to make a thin film luminescent solar concentrator using the industry compatible technique of sputtering. The challenge was to acquire adequate absorption, around 50 % in the UV to VIS region of the solar spectrum, in a thin film under a micron thick. A research question was defined as follows:

Fabricate strong and broad absorbing thin films made via (reactive) magnetron sputtering and study their optical and luminescent properties for LSC considerations.

The method of research was to fabricate thin films with compositional gradients in order to establish trends in luminescence efficiency and is described in detail in Chapter 2. Three approaches were undertaken to achieve the goal of increased absorption in trivalent lanthanide based luminescent thin films. The first of these approaches, described in Chapter 3, was an attempt to reduce trivalent samarium to divalent samarium and subsequently increase divalent samarium content in silicate based glasses through co-doping of boron. The second attempt, Chapter 4, involved high concentration of a strong absorbing sensitizer ion, trivalent chromium, to activate trivalent neodymium in a Al<sub>2</sub>O<sub>3</sub>-Y<sub>2</sub>O<sub>3</sub> host. Lastly, the third attempt, Chapter 5, explored sensitization of trivalent ytterbium through the host material CuGaS<sub>2</sub>. This chapter, Chapter 6, concludes this work by summarizing key insights, offering closing thoughts, and suggesting future research directions related to the XY-method introduced in Chapter 2. It also discusses the findings from the studies on Sm, Cr, Nd, and Yb-based thin film LSCs, explored in Chapters 3, 4, and 5, respectively. In addition a comparison is made between the three films studied as potential LSC candidates. Subsequently a new type of material, not covered in this thesis, that could potentially fulfil the criteria for a thin film based LSC is suggested. Lastly, some final thoughts on the electricity generating window are given in the context of this thesis.

#### 6.1 The XY Method

#### **Reactive Magnetron Sputtering**

Chapter 2 provided a detailed description of all methodologies used in this thesis. It can also serve as a manual for future scientists to be able to efficiently and quickly conduct similar type research presented in this thesis. It has been shown that the fabrication of quality thin films, with correct stoichiometry and crystallinity, is anything but trivial. The numerous amount of parameters that can be tweaked during the sputtering process makes it a powerful yet complicated synthesis technique. In my first week as a PhD candidate a colleague told me that sputtering is half science and half art, which I have come to agree with. In order to succeed in studying luminescent thin films it is imperative to master the art of sputtering. First, a firm grasp should be obtained on the effect that the various parameters (working pressure, target power, discharge voltage, deposition temperature etc.) have on the sputtering process. Simple experiments such as the hysteresis experiment can aid in understanding the behaviour of sputter targets. A design of experiments where a number of sputter parameters are varied in a systematic way can be a useful tool in acquiring the desired film. There is one feature of the AJA Orion-5 sputter coater that I personally miss. It is the ability to modify reactive gas flow during a deposition as a response to a changing voltage discharge, i.e. a feedback loop. As has been said in Chapter 2, the voltage discharge of a target gives vital information on the oxidation state of the target during reactive sputtering. It could be of great use if one can reduce or increase oxygen flow during a process if the voltage discharge of the target is moving in an undesired direction, or in other words, if the target becomes too oxidized or metallic. Unfortunately, as it stands today, AJA's software to control the sputter coater does not allow the user to change anything during a pre-defined sputter 'recipe'. It is unreasonable to monitor the voltage discharge manually during the entirety of the deposition. Another interesting feature to implement would be to have spectroscopic information on the plasma discharge. Argon plasma typically is purple, yet sputtering metallic Chromium yields a more blue looking plasma. Similarly to the discharge voltage, the plasma emission could provide useful insight in target condition. Finally, having an ellipsometry set-up to do in-situ measurements during deposition could provide invaluable information on the growth of the thin films.

#### Thin Film Characterization

Once the challenges of sputtering quality thin films have been overcome, then comes the characterization of the thin films through the XY-method. **Chapter 4**, regarding Cr and Nd in the Al<sub>2</sub>O<sub>3</sub>-Y<sub>2</sub>O<sub>3</sub> system, nicely demonstrates the validity of XY method

where luminescent behaviour as a function of Al:Y ratio of both Cr and Nd was consistent with literature reported behaviour. Sputtered thin films with little to no reported literature, such as the CuGaS<sub>2</sub>:Yb in **Chapter 5**, can be rapidly optimized for luminescence intensity with the XY method. The ability to investigate luminescent behaviour as a function of composition has proven to be a powerful tool for thin film research. One drawback of the XY method is the inability to determine position dependent quantum yields inside an integrating sphere. What's more is that the presence of multiple phases of a gradient film, such as the monoclinic Y<sub>4</sub>Al<sub>2</sub>O<sub>9</sub> and garnet Y<sub>3</sub>Al<sub>5</sub>O<sub>12</sub> phases in **Chapter 4**, can be undesirable and lead to defects and significant quenching of luminescence. Despite these drawbacks, the true value in this method lies in quickly establishing trends within the film as a function of composition rather than to study specific compositions.

Overall, the large quantity of data that can be generated with the XY method make it an invaluable tool for analysis of a wide range of thin films with varying compositions. It can be challenging to navigate the vast quantity of data for trends within gradient thin films, however **Chapter 2** should aid those who aim to continue conducting this type of research. Expanding the XY set-up to include reflection measurements and automated power dependent emission measurements are a couple of ideas that would be fascinating to implement in the set-up. I hope that this thesis has served guidance to utilizing the XY method and provided an idea to its possibilities.

# 6.2 Findings on the Thin Films of this Thesis

In the following section the motivation and findings of each thin film studied in this thesis are briefly summarized. Then a side-by-side comparison is made between the samples using quantum efficiency measurements to determine which material has the most potential to be used as a thin film LSC.

# Sm<sup>2+</sup> in Glass (Chapter 3)

Divalent samarium, with its strong and broad 4f<sup>6</sup>-4f<sup>5</sup>5d<sup>1</sup> absorption and subsequent 4f<sup>6</sup>-4f<sup>6</sup> emission, has the potential to be a luminescent centre in LSCs. However, Sm is easily oxidized to its undesired trivalent state, especially in a silica glass. It has been shown in **Chapter 3** that B, similarly to Al, can promote the reduction of Sm<sup>3+</sup> when co-doped into the silica host. The most intense Sm<sup>2+</sup> emission was found, using the gradient method, at a Sm content of just 0.01 %. At these low Sm concentrations there is no worthy absorption in transmission spectra in a one micrometre thin film. The strontium borate host was considered as it provides a dedicated divalent cation site (Sr) for Sm<sup>2+</sup>.

However, sputtering stoichiometric and crystalline strontium borate was unsuccessful. The Sm<sup>2+</sup> excitation and emission spectra in the strontium borate host yielded similar results as the amorphous silicon borate hosts, suggesting that Sm<sup>2+</sup> occupies a similar site in the two materials.

## Cr3+ and Nd3+ in the Al2O3-Y2O3 System (Chapter 4)

The strong and broad absorption properties of Cr3+ combined with the narrow nearinfrared emission properties of Nd3+ makes this pair of ions an interesting candidate for LSC applications. It has been shown that to achieve the desired absorption of roughly 50% across the visible spectrum in a thin film of under a micron thick requires a fully concentrated system of Cr<sup>3+</sup> (i.e. Cr<sub>2</sub>O<sub>3</sub>). A photo of a sputtered Cr<sub>2</sub>O<sub>3</sub> film is shown in Fig. 6.2b. It is known that Cr3+ emission is quenched at Cr3+ content above 1 % in aluminium oxide due to a combination of efficient energy migration between Cr ions and the formation of Cr-Cr pairs at which the energy can relax non-radiatively [1]. The main idea explored in this chapter is to investigate whether this energy migration amongst Cr ions can facilitate energy transfer to Nd3+. For this reason a study is performed using the gradient method to investigate the energy transfer behaviour between highly concentrated Cr3+ systems and Nd3+. First the luminescent behaviour of the individual Cr3+ and Nd3+ ions at low concentration (1%) is investigated in the Al<sub>2</sub>O<sub>3</sub>-Y<sub>2</sub>O<sub>3</sub> system via the gradient method. On a single thin film the Y:Al ratio varies between 0.5 and 3.5, encapsulating the garnet (Y:Al = 0.6:1), perovskite (Y:Al = 1) and monoclinic (Y:Al = 2) stoichiometry's of yttrium aluminate. X-ray diffraction measurements did not show any perovskite phase present in the film, however it did show the garnet and monoclinic phases. The emission and lifetime properties of both Nd3+ and Cr3+ when scanning across the sample (i.e. going from the garnet to the monoclinic phase) are consistent with literature values, demonstrating the power of the gradient method. Co-doping the Cr3+ and Nd3+ ions in the Al2O3-Y2O3 system showed that the garnet phase was most promising for energy transfer between two ions. As the Cr<sup>3+</sup> content in the garnet (Y<sub>3</sub>Al<sub>5-x</sub>Cr<sub>x</sub>O<sub>12</sub>, 0.05<x<2) increases, the radiative lifetime of Nd<sup>3+</sup> decreases significantly from 0.24 ms to below 0.05 ms. This suggests that after the sensitization of Nd3+, energy back-transfer from Nd3+ to Cr3+ occurs. Back-transfer to Cr can be due to Cr<sup>4+</sup> ions present in the sample, or due to Cr<sup>3+</sup> ions situated at low ligand field strength sites. The high Cr3+ content did not yield the desired effect of utilizing the Cr energy migration amongst Cr<sup>3+</sup> ions to sensitize Nd<sup>3+</sup>. The combination of efficient non-radiative relaxation by Cr-Cr pairs and back-transfer from Nd3+ to Cr3+ inhibits the use of high Cr<sup>3+</sup> content in thin film LSC applications.

## CuGaS<sub>2</sub>:Yb<sup>3+</sup> (Chapter 5)

The final material studied in this thesis was CuGaS<sub>2</sub> doped with Yb<sup>3+</sup>. Cu(Al, Ga, In)(S, Se, Te)<sub>2</sub> are materials with a chalcopyrite structure and are already used for thin film solar cell technology due to their tuneable bandgap and their desirable strong and broad absorption properties. There is no reported literature on utilizing this host material with trivalent lanthanides for thin film LSC applications. In Chapter 5 it is shown that it is possible to sensitize Yb3+ through the CuGaS2 host. An energy transfer mechanism responsible for the sensitization of Yb<sup>3+</sup> is proposed involving the trapping of electrons by the Yb<sup>2+</sup> ground state with subsequent recombination of a hole resulting in Yb<sup>3+</sup> emission. It is found that Cu-deficient regions of a compositional gradient CuGaS2 film yield more intense emission than stoichiometric CuGaS<sub>2</sub> part of the film. This is attributed to a widening of the band-gap which results in a more efficient hole transport to Yb2+ [2]. The radiative lifetime of Yb3+ in CuGaS2 is measured to be 110 µs and temperature-independent, indicating the absence of thermal quenching of the Yb3+ excited state. However, the intensity of Yb3+ emission exhibits strong temperature dependence, demonstrating that energy transfer efficiency is affected by temperature. Temperature-dependent, time-resolved intensity measurements reveal a thermal activation energy between 0.15 and 0.28 eV depending on composition, which is interpreted as the Yb<sup>2+</sup> electron trap depth in CuGaS<sub>2</sub>. Annealing the sample in oxygen increased the Yb3+ intensity by a factor of 15, indicating that oxygen plays a vital role that should be investigated further. This work provides a neat framework to investigate this energy transfer mechanism in other chalcopyrite type materials.

# Comparison of the Thin Films in this Thesis

The optical efficiency, defined in Chapter 1 as:

$$\eta_{opt} = (1 - R)\eta_{abs}\eta_{IQY}\eta_{trap}\eta_{SA}\eta_{WG}$$
 (6.1)

where R represents the reflected light,  $\eta_{abs}$ ,  $\eta_{IQY}$ ,  $\eta_{trap}$ ,  $\eta_{SA}$  and  $\eta_{WG}$  are the absorption, internal quantum yield, trapping efficiency, self-absorption and wave-guiding efficiency respectively, is the best indicator of the potential of an LSC. The execution of measurements quantifying them, are not trivial. It involves using a light source that imitates the light coming from the sun and isolating the emission of the LSC originating from the edge of the glass. Alternatively, we can simplify the set-up by measuring the quantum efficiency in a narrower wavelength range using a single LED and collect the emission from the entire LSC using an integrating sphere, not just the edges. Though this simplified experiment does not provide a final answer for the optical efficiency, it does give information on the internal quantum yield of our material. In **Fig. 6.1** we see

two such quantum efficiency measurements for CuGaS<sub>2</sub>:Yb<sup>3+</sup> (a) and SiAlBO:Sm<sup>2+</sup> (b). In the main figure in (a) and (b) we can see the absorption properties of the samples. In (a) a 375 nm LED is used whereas a 470 nm LED is used for (b). The difference of the recorded LED intensity between a substrate without coating and with coating is a measure for the absorption. For CuGaS<sub>2</sub>:Yb<sup>3+</sup> (a), the absorption is found to be roughly 92%, whereas for SiAlBO:Sm<sup>2+</sup> (b) the absorption is just 5%. We can also see this in a photograph of the samples presented in **Figure 6.2**, where CuGaS<sub>2</sub>:Yb<sup>3+</sup> has an orange color (strong absorption) and SiAlBO:Sm appears transparent (weak absorption). In the inset of **Fig. 6.1** we see the emission related to Yb<sup>3+</sup> (a) and Sm<sup>2+</sup> (b). The Yb<sup>3+</sup> emission is very weak, roughly 20 counts at peak intensity, despite absorbing strongly. The Sm<sup>2+</sup> peak emission is 50 times more intense despite absorbing much less. Dividing the integrated emission by the integrated absorption yields the quantum yield, which is found to be roughly 0.01 % for CuGaS<sub>2</sub>:Yb<sup>3+</sup> and 6% for SiAlBO:Sm<sup>2+</sup>. Though CuGaS<sub>2</sub>:Yb<sup>3+</sup> absorbs roughly 20 times more than SiAlBO:Sm<sup>2+</sup> it is outweighed by the 600 times higher efficiency of SiAlBO:Sm<sup>2+</sup>.

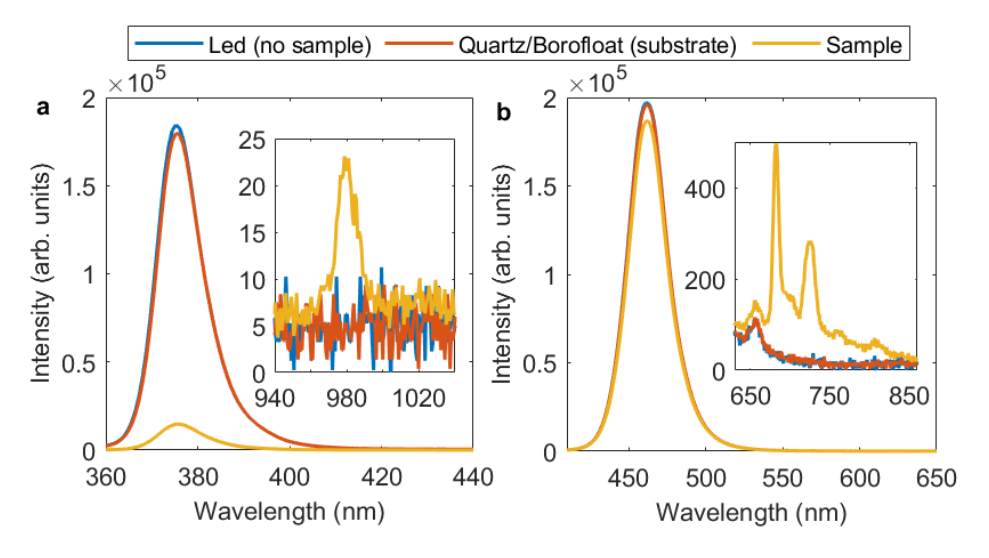


Fig. 6.1. Absorption and emission (inset) of CuGaS<sub>2</sub>:Yb<sup>3+</sup> (a) and SiAlBO:Sm<sup>2+</sup> (b)

If we assume that all the emission originated from the edge (i.e  $\eta_{trap} = \eta_{WG} = 1$ ), no light is reflected (R = 0) and absorption is 5 % then our optical efficiency for SiAlBO:Sm<sup>2+</sup> for the wavelength range 350< $\lambda$ <550 is simply 0.05\*0.06 = 0.003 or 0.3 %. Note that the absorption of 5 % (0.05) is taken from the integrating sphere measurement which involves many absorption events. Under normal conditions the

light from the sun will hit our LSC just once, leading to significant lower absorption. Transmission measurements of SiAlBO:Sm<sup>2+</sup> presented in Chapter 3 showed no clear absorption of Sm<sup>2+</sup> in transmission spectra. This means that the optical efficiency of 0.3 % is generous given the assumption that all emission originated from the edge and the overestimation of the absorption.

Unfortunately, it was not possible to determine the quantum efficiency of Nd in the Al<sub>2</sub>O<sub>3</sub>-Y<sub>2</sub>O<sub>3</sub> system co-doped with Cr and Nd (Chapter 4). A series of 9 samples were fabricated with a YAG stoichiometry (Al:Y = 5:3) with varying Nd and Cr content. Doping concentrations of 1, 5 and 10 % were used for Nd and for Cr 1, 10 and 20%. The strongest emitting Nd sample was found to have 10 % Cr doping and 5 % Nd doping. A picture of the sample is shown in **Fig. 6.2**a. Similar to SiAlBO:Sm, the sample appears transparent (i.e low absorption efficiency), but it is slightly hazy compared to SiAlBO:Sm. We can deduce, as no emission was observed in the integrating sphere, that the quantum efficiency of the Y<sub>2.85</sub>Al<sub>4.5</sub>Cr<sub>0.5</sub>Nd<sub>0.15</sub>O<sub>12</sub> sample is much lower than the 6% of SiAlBO:Sm. A combination of both low quantum and low absorption efficiency yields an overall low optical efficiency.

A side by side photo of the most emitting samples studied in this thesis is shown in Fig. 6.2a. In Fig. 6.2b a photo of a Cr<sub>2</sub>O<sub>3</sub>:Nd film is shown as an example of what a highly concentrated Cr film would look like. If we imagine that the four samples in Fig. 6.2 are extremely efficient in both luminescent properties and wave-guiding properties then there remains a clear problem with commercial application purposes: color, or lack thereof for the two in the center. The transparent SiAlBO:Sm and Y<sub>3</sub>Al<sub>5</sub>O<sub>12</sub>:Cr, Nd films immediately indicate that absorption in the visible part of the spectrum is very low (<10%). This already puts an upper limit of our optical efficiency at 10% which does not suffice for commercial applications. Meanwhile the CuGaS<sub>2</sub>:Yb and Cr<sub>2</sub>O<sub>3</sub>:Nd film have an undesirable color. Luckily this color can be offset by including a subsequent thin film with complimentary absorption properties to offset the color and create a neutral grey. Unfortunately, as has been shown, the luminescent efficiencies of these samples were so low that they too are not suitable for commercial applications. In the next section some thoughts are provided on future research directions for these materials.

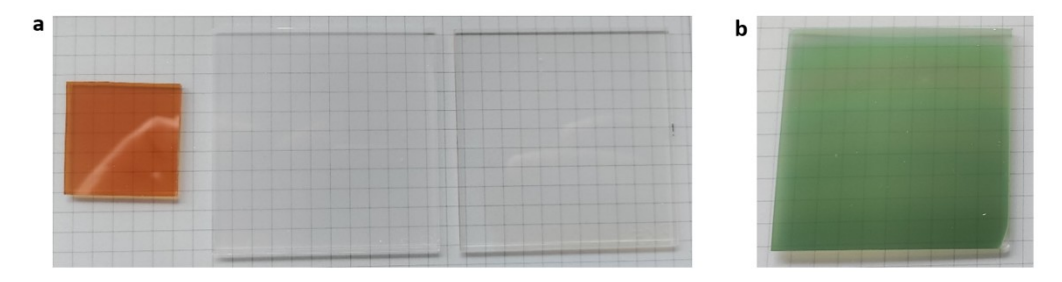


**Fig. 6.2.** Photo of the strongest emitting samples of each chapter side by side. From left to right:  $CuGaS_2:Yb^{3+}$ ,  $Y_3Al_5O_{12}:Cr^{3+}$ ,  $Nd^{3+}$  and  $SiAlBO:Sm^{2+}$ . **b)** An image of a  $Cr_2O_3:Nd^{3+}$  film to demonstrate what a highly concentrated  $Cr^{3+}$  would look like.

#### 6.3 Future Research Directions

#### Sm<sup>2+</sup> in Glass

The key obstacle for the development of electricity-generating windows using Sm<sup>2+</sup>based thin film LSCs was the challenge of achieving sufficiently high Sm<sup>2+</sup> content. Increasing the Sm<sup>2+</sup> content in SiAlO:Sm through co-doping of boron was unsuccessful. Providing a dedicated site to Sm<sup>2+</sup> by sputtering SrBO yielded similar results as with the amorphous SiAlO films. Another, more dedicated, attempt to sputter high quality, single phase SrB<sub>4</sub>O<sub>7</sub> or SrB<sub>6</sub>O<sub>10</sub> doped with both Eu and Sm, as has been done in other work with solid state synthesis, would be of interest [3]. It should be noted that at a typical 5 – 10 %, doping of Sm<sup>2+</sup> in SrB<sub>4</sub>O<sub>7</sub> will likely still lack sufficient concentration of Sm<sup>2+</sup> ions to achieve the desired absorption in a thin film of less than a micron. The thin films might lack the desired strong absorption, however sputtering SrB<sub>4</sub>O<sub>7</sub> or SrB<sub>6</sub>O<sub>10</sub> has not been reported before and is therefore an achievement on its own. Furthermore, the reported high quantum yield of this material offsets, to some degree, the low absorption. Though thick films (> 1 micron) are unwanted due to long sputter deposition times, if such a material shows promise it can be worthwhile to explore such thicker films nevertheless. Another option is to move away from sputtering and use other synthesis techniques such as the sol-gel method along with spray coating, though this deposition technique comes with its own challenges. Though the co-doping strategy was unsuccessful in increasing Sm<sup>2+</sup> content, another study using a multi-layer approach was successful [4]. It has been shown that roughly 50 % absorption from Sm<sup>2+</sup> is possible in multi-layered SiAlO:Sm thin films. The Sm content in this work is 2.5% and the total thickness 1.2 microns. Unfortunately the quantum efficiency severely drops to a mere 0.2 % which is more likely than not due to concentration quenching of Sm<sup>2+</sup>. To mitigate concentration effects would require to decrease the Sm concentration which would in turn decrease the absorption. Again, it might be worth exploring alternative synthesis methods to fabricate thicker multilayered thin films with lower Sm content.

# Cr3+ and Nd3+ in the Al2O3-Y2O3 System

Strong absorption related to Cr<sup>3+</sup> was observed in films with a high Cr content as exemplified in **Fig. 6.2**b. However, although one might expect that increased Cr content leads to a higher energy transfer efficiency to Nd<sup>3+</sup>, due to energy migration among Cr ions, a decrease in energy transfer to Nd is found instead. The lower energy transfer efficiency is likely due to an efficient quenching route through formation of Cr pairs and clusters. Though this limits the uses of this particular Cr-Nd pair of ions for LSC applications, it can be worth investigating other pairs of ions that do not have the

tendency to form pairs like Cr<sup>3+</sup>. The concept of improving energy transfer rates by increasing sensitizer content has been successful in certain scintillation compounds like the fully concentrated Yb<sup>2+</sup> (sensitizer) system YbCl<sub>2</sub> doped with Sm<sup>2+</sup> (activator) [5]. An in-depth literature search is required to find the next sensitizer and activator pair that would be of interest to study for LSC applications.

#### CuGaS2:Yb3+

The observed energy transfer between the CuGaS<sub>2</sub> host and Yb<sup>3+</sup>, though inefficient, shows promise for host sensitized Yb<sup>3+</sup> emission. The tune-ability of chalcopyrite structure type hosts (I-III-VI<sub>2</sub>, Cu(Al,Ga,In)(S, Se, Te)<sub>2</sub>) via playing with the composition offers an opportunity to thoroughly investigate the energy transfer mechanism between this type of host and dopant. In **Fig. 6.3** a series of samples that were prepared in this work are shown with varying Cu:Ga ratio and S:Se ratio. Their compositions are shown in **Table 6.1**. As can be seen on the photo, the color of the sample changes to darker colors going from left to right. This is due to the narrowing of the bandgap when going from a Cu:Ga ratio of 0.26:1 to 1:1 and replacing S by Se.

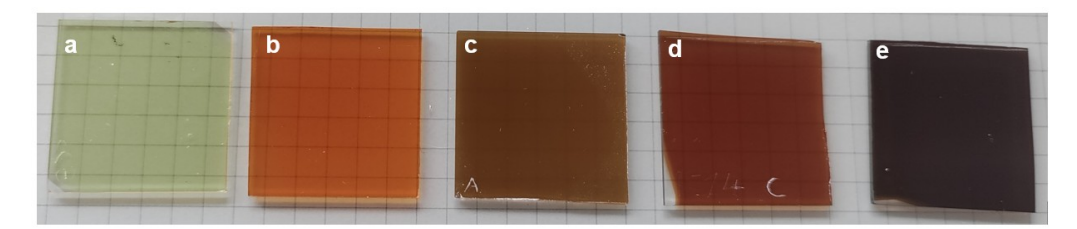


Fig. 6.3. Photograph of sputtered CuGaSSe samples with varying Cu:Ga ratios and S:Se ratios shown in Table 6.1

Table 6.1. Cu: Ga and S:Se atomic ratios of sputtered samples shown in Fig. 6.3.

Sample	a	b	c	d	e
Cu:Ga	0.26:1	0.74:1	0.92:1	1.12:1	0.93:1
S:Se	1:0	1:0	1:0	1:0.78	0:1

A similar investigation as performed in **Chapter 5** (transmission, composition, emission and temperature dependent lifetime measurements) can be used on a range of materials in the chalcopyrite family. Datasets on multiple materials can provide valuable

insights into the achievable efficiencies with the energy transfer mechanism proposed in **Chapter 5**. A start had been made to conduct this research, as evident by the fabrication of the various samples shown in **Fig. 6.3**, however due to the time-restricted nature of a PhD this has not been finished. One might expect that the energy transfer efficiency will decrease as the band-gap narrows due to more non-radiative recombination's of the generated e-h pairs. Whereas a larger electron trap depth (i.e. raising of the conduction band) could improve the energy transfer efficiency. Taken together there are numerous interesting research directions for this class of materials. It is worth noting that a new project, LumiCoat, has been successfully funded to investigate these materials further for LSC application.

#### Novel materials

It goes without saying that there are other types of materials not listed in this thesis that can satisfy the properties of a thin films based LSC. One of such material that was briefly considered during the making of this thesis was tetravalent lanthanide oxide hosts (CeO<sub>2</sub>, TbO<sub>2</sub> and PrO<sub>2</sub>) doped with ytterbium. In particular TbO<sub>2</sub>:Yb<sup>3+</sup> was considered. A photo of the sample is shown in **Fig. 6.4**. The orange colour is due to the charge transfer transition between Tb<sup>4+</sup> and O<sup>2-</sup> ions in the host. Subsequent energy transfer to an emitting centre such as Yb<sup>3+</sup> would yield the desired properties of an LSC. TbO<sub>2</sub>:Yb<sup>3+</sup> films had been studied, and it was found through XRD studies that approximately 75% of the sample appeared to be Tb<sub>2</sub>O<sub>3</sub> and 25 % TbO<sub>2</sub>. No Yb<sup>3+</sup> luminescence was observed, however an extensive study has not been done. More information on this project can be found in the bachelor thesis of Pepijn Kluytmans [6]. Sensitization through a charge transfer transition like the one of TbO<sub>2</sub> is indeed another mechanism that can be worthwhile exploring in the future for strong absorbing thin film LSC research.

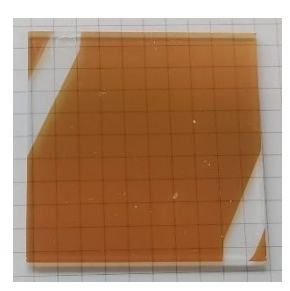


Fig. 6.4. Picture of a sputtered TbO<sub>2</sub>:Yb thin film.

# 6.4 Final Thoughts on the Electricity Generating Window

To realize the electricity generating window requires overcoming two main challenges: efficiency and costs. The low efficiency of today's LSCs simply do not make it worthwhile for mass production. However, improving efficiency with the use of exotic (expensive) materials that involve complicated synthesis techniques (also expensive) will move the goalpost to higher efficiencies to make production economically worthwhile. The environmental impact of the materials used are also a concern of the LSC community. For this reason, cadmium and lead based quantum dots, though promising, are not considered for LSC applications. The use of organic dyes is significantly cheaper, however, issues like unwanted colorization, self-absorption and photo-degradation must first be overcome. The thin film based LSC is a cost-effective alternative that is less explored in the LSC community. Sputter deposition, an industry standard, of luminescent thin films can be a viable way to bring the electricity generating window to the market. Therefore, sputtered thin films already eliminate the cost challenge and leave a single main challenge: improving efficiency. In this thesis efficiency is attempted to be improved by increasing absorption in thin films. Further research is required that focusses on strongly absorbing thin films to realize an acceptable efficiency for LSCs. Regardless of which direction one chooses to take when researching materials for LSCs there are challenges ahead. The road to putting an electricity generating window on the market is uphill. The perfect thin film LSC material is waiting to be discovered and when it is, the commercial implications are enormous.

#### 6.5 References

- [1] G. Imbusch, "Energy transfer in heavily-doped ruby," *Journal of luminescence*, vol. 53, no. 1-6, pp. 465-467, 1992.
- [2] T. Nishimura, K. Nakada, and A. Yamada, "Examination of a Cu-Deficient Layer on Cu(In, Ga)Se2 Films Fabricated by a Three-Stage Process for Highly Efficient Solar Cells," ACS Applied Energy Materials, vol. 2, no. 7, pp. 5103-5108, 2019/07/22 2019, doi: 10.1021/acsaem.9b00774.
- [3] L. Erasmus *et al.*, "Making Eu<sup>2+</sup>-and Sm<sup>2+</sup>-Doped Borates Fit for Solar Energy Applications," *ACS Photonics*, vol. 10, no. 3, pp. 609-622, 2023.
- [4] G. B. F. Bosco *et al.*, "Metal-insulator multilayer precursors for enhanced Sm<sup>2+</sup> absorption and Tm<sup>2+</sup> luminescence in SiAlO thin films prepared by magnetron sputtering," *Journal of Luminescence*, vol. 241, p. 118421, 2022/01/01/ 2022, doi: https://doi.org/10.1016/j.jlumin.2021.118421.
- [5] C. van Aarle, K. W. Krämer, and P. Dorenbos, "Characterisation of Sm<sup>2+</sup>-doped CsYbBr3, CsYbI3 and YbCl2 for near-infrared scintillator application," *Journal of Luminescence*, vol. 251, p. 119209, 2022.
- [6] P. Kluytmans, "Towards Yb3+-doped TbO2 thin films for luminescent solar concentrators," Bachelor, Radiation Science & Technology, Delft University of Technology, 2021.

# **Summary**

The topic of this thesis pertains to researching novel materials for luminescent solar concentrator (LSC) applications. An LSC, as the name suggests, concentrates solar radiation incident on a large surface area to a smaller surface area. First conceptualized in the 1970's, LSCs can be used in conjunction with solar cells to create a so-called 'electricity generating window'. Fast-forward 50+ years and the electricity generating window is yet to be commercialised. In **Chapter 1** the motivation behind developing LSCs and their operating principles is introduced along with obstacles that must be overcome in order to mass adopt this technology. For example, from basic calculations, it can be shown that in order for an electricity generating window to obtain a commercially interesting power output of >100 W/m<sup>2</sup> it is necessary to absorb at least 50% of both the ultraviolet (UV) and visible (VIS) part of the solar spectrum. Absorbing only a part of the VIS spectrum does not only lower output but will also lead to unwanted colorization of the window. Another obstacle that is often overlooked is complying with glass-industry practises which limits synthesis methods to create LSCs. Reactive magnetron sputtering is a technique for synthesizing thin films that is upscalable and already a standard practise in the glass industry. Sputtering is therefore the synthesis method of choice in all the work presented. The key challenge addressed in this thesis is in obtaining thin films with a thickness of a micron or less that meet the absorption and luminescence requirements for efficient LSCs.

Thin films have many properties that can be characterized such as the composition, crystallinity, density, porosity, thickness, optical/mechanical/thermal properties and more. Including luminescent ions in a thin films expands the list of properties like emission- and excitation spectra, radiative lifetime, quantum yields and more. To characterize each property of luminescent thin films and analyse their influence on the overall behaviour of an LSC would be a long, strenuous and, in my opinion, a somewhat boring endeavour. Therefore, Chapter 2 dives into a systematic procedure to investigate luminescent thin films via the 'XY-Scanning Methodology'. This methodology involves the creation of thin films with a gradient in composition and then performing position dependent luminescent and composition measurements to map luminescent properties to local composition. My predecessor, Evert Merkx, has developed a custom-built set-up to use this methodology with which we can now rapidly characterise a range of materials on a single substrate. Working alongside my master's student, Bauke Kooger, we enhanced the user experience of this setup, ensuring that both myself and future users can continue to utilize this unique method with ease and efficiency. Chapter 2 aims to provide a practical guide on conducting thin film research within the luminescence materials group at the TU Delft.

This thesis describes 3 different attempts to tackle the aforementioned key challenge of increasing absorption in luminescent thin films. Before I started there was one main contender as a LSC in the research group which was silicon aluminate glass doped with divalent samarium (SiAlO:Sm<sup>2+</sup>). Divalent samarium (Sm<sup>2+</sup>) has favourable absorption properties that range from the UV up to about 600 nm and sharp emission around 700 nm without self-absorption. However the concentration of Sm2+ is limited to less than 1% (atomic, at.%) as higher Sm content leads to an increase in the formation of undesired Sm<sup>3+</sup>. The 1 at.% of Sm<sup>2+</sup> in a mere 1 micron film is unable to absorb adequately for LSC applications. My first attempt aimed to increase the solubility of Sm<sup>2+</sup> inside the SiAlO (or similar) host by co-doping Sm<sup>2+</sup> with Boron (i.e. SiAlBO:Sm<sup>2+</sup>). Chapter 3 dives into this attempt which involves the sputtering and studying of a number of different hosts with Sm<sup>2+</sup> and co-dopants such as borates, aluminates and silicates. Results have hinted at no sufficient improvement of the obtainable Sm<sup>2+</sup> content through co-doping. To guarantee a suitable site and therefor a high solubility for Sm2+ the strontium tetra borate (SrB4O7) host was attempted, however the sputtering of crystalline SrB<sub>4</sub>O<sub>7</sub> was not successful. Despite the challenges faced in synthesizing SrB<sub>4</sub>O<sub>7</sub> (and borates in general), this initial attempt provided the essential foundation that enabled me to carry out research throughout my PhD.

The second attempt involved not one luminescent ion but two. A sensitizing ion that absorbs UV and VIS radiation and transfers its energy to an activator ion which then emits. The sensitizing ion must be present in high concentrations or even fully concentrated to absorb the desired amount of radiation. In **Chapter 4** the results regarding the yttrium aluminate (Y<sub>2</sub>O<sub>3</sub>-Al<sub>2</sub>O<sub>3</sub>) system doped with varying concentration of trivalent chromium (Cr<sup>3+</sup>, the sensitizer) and trivalent neodymium (Nd<sup>3+</sup>, the activator) is presented. The xy method, presented in Chapter 2, proved to be a valuable technique in researching the luminescent behaviour of Cr<sup>3+</sup> and Nd<sup>3+</sup> when singly and doubly doped in the Y<sub>2</sub>O<sub>3</sub>-Al<sub>2</sub>O<sub>3</sub> system. The absorption requirement for LSCs is met with a 100% doping of Cr<sup>3+</sup>, i.e. a chromium oxide (Cr<sub>2</sub>O<sub>3</sub>) thin film, however no luminescence is observed when doped with Nd<sup>3+</sup>. The energy transfer efficiency between Cr<sup>3+</sup> and Nd<sup>3+</sup> appeared to reduce with increasing Cr<sup>3+</sup>, likely due to the formation of Cr pairs and clusters. Increasing the Cr<sup>3+</sup> content also led to more back transfer from Nd<sup>3+</sup> to Cr<sup>3+</sup> as shown by a decrease in radiative lifetime values.

The final attempt does not rely on a ion to sensitize an activator, but rather relies on the host material itself to act as the sensitizer. Copper indium gallium selenide (CuGaInSe<sub>2</sub>, CIGS) is a material already used by the thin film solar cell community due to its high absorption coefficient. The narrow band-gap of the material results in the desired broad absorption across the UV and VIS. Absorption across the band-gap promotes an electron from the valence band to the conduction band, leaving behind a hole in the valence band. The question asked is whether this electron-hole pair, also

known as an exciton, can transfer its energy to a nearby activator such as trivalent ytterbium (Yb³+). The mechanism of this energy transfer process is discussed in detail in **Chapter 5**. CIGS has a tuneable bandgap simply by tweaking the indium gallium ratio or by replacing selenium with sulphur or tellurium. This tune-ability of the bandgap allows to investigate the energy transfer mechanism between the exciton and Yb³+ as a function of bandgap, or more specifically the absolute energy with respect to the vacuum level of the VB and the CB. Copper gallium sulphide (CuGaS₂) doped with Yb³+ was studied in detail to understand the energy transfer mechanism between the host and the dopant. A low energy transfer efficiency of at most 0.01% was found, which is too low for LSC applications. Repeating the study from Chapter 5 on materials synthesized following alternative sputtering routes and additional materials within the chalcopyrite family could offer valuable insights, leading to further understanding of the energy transfer mechanism and revealing potential limitations.

The final chapter, **Chapter 6**, provides closing remarks on the three different attempts to improve absorption in luminescent thin films. A side-by-side comparison of the samples are made to provide concluding remarks on their potential as LSCs. Quantum efficiency measurements reveal that Sm<sup>2+</sup> in SiAlBO has the highest efficiency, around 6%, though its absorption remains limited. In contrast, the CuGaS2:Yb<sup>3+</sup> thin films exhibit strong absorption but with a much lower quantum efficiency of just 0.01%. New research directions for the materials explored in this thesis are proposed, along with an additional thin-film LSC candidate not covered in the current work. Lastly, some final remarks are offered on the luminescent solar concentrator

# Samenvatting

#### Gebruik van luminescente zonneconcentratoren (LSCs)

Dit proefschrift heeft betrekking op het onderzoeken van alternatieve materialen voor het gebruik van luminescente zonneconcentratoren (Engels: luminescent solar concentrators (LSC)). Een LSC kan worden gebruikt om een zg. 'electriciteitwekkend raam' (EWR) te maken. Feitelijk is een LSC een luminescerend raam dat invallend zonlicht absorbeert en dan uitstraalt binnen een vensterglas. Het licht wordt vervolgens naar de zijkanten van het raam gestuurd waar met behulp van zonnepanelen elektriciteit wordt opgewekt. In **Hoofdstuk 1** is het belang voor toepassing van LSCs aangegeven met daarbij de problemen die opgelost moeten worden bij de productie van de EWR's. Hier komt ook de elementenreeks lanthaniden (ook wel zeldzame aardmetalen genoemd, Engels: rare earth's) aan de orde die verantwoordelijk zijn voor de luminescentie eigenschappen van het raam.

#### Doel proefschrift

Doel bij dit proefschrift is om de absorptie-eigenschappen van lanthaniden en de LSC te verhogen waardoor de werking van de LSCs verbetert en het rendement van EWRs zal toenemen. Er wordt bij dit onderzoek en bij de productie van dunne films gebruik gemaakt van binnen de glasindustrie bestaande actief magnetron-sputter-technologie. Met gebruikmaking van deze techniek zullen LSCs kunnen worden gemaakt.

## Bepalen eigenschappen dunne films

In **Hoofdstuk 2** is een onderzoeksprocedure opgenomen voor het bepalen van eigenschappen van dunne films. Eerst wordt omschreven hoe reactief magnetron-sputteren kan worden gebruikt om een dunne film op een glasplaatje aan te brengen. Vervolgens wordt aangegeven hoe o.m. de samenstelling, kristalstructuur, transmissie en luminescentie-eigenschappen van de dunne film kan worden bepaald. Hierbij is de XY-scanning techniek van belang. Deze techniek wordt gebruikt om het verband tussen de samenstelling van de dunne film en luminescentie-eigenschappen vast te stellen. De onderzoeksprocedure in dit hoofdstuk kan dienen als praktische handleiding voor het dunne filmonderzoek dat binnen de groep luminescentiematerialen aan de TU Delft wordt uitgevoerd.

# Verhoging absorptie dunne films

In **Hoofdstuk 3, 4 en 5** worden drie onderzoeken beschreven om de absorptie van luminescerende dunne films te verhogen. Elk hoofdstuk behandelt een onderzoek. Bij het 1e onderzoek wordt vanwege de gunstige eigenschappen de lanthanide samarium (Sm) gebruikt in dunne films van aluminiumborosilicaat-type glas (SiAlBO). Het SiAlBO is de gastrooster waarin Sm atomen zich in bevinden. Gebleken is dat dunne films met een lage Sm concentratie zich vanwege de gunstige absorptie- en emissie-eigenschappen kunnen gedragen als LSC. De absorptie is bij een lage Sm concentratie echter onvoldoende voor een goede werking van het EWR. Andersom leidt een hoge concentratie van Sm tot het doven van de emissie. De Sm-

concentratie is hierbij dus het aandachtspunt. Met het 1<sup>e</sup> onderzoek (**Hoofdstuk 3**) wordt de invloed bepaald van de samenstelling van het glas (de verhouding van Si:Al:B) op de absorptieen emissie-eigenschappen van Sm in verschillende concentraties.

Bij het 2° onderzoek (**Hoofdstuk 4**) werd de gebruikscombinatie van een absorberend element (in dit geval Cr) en een emitterend element onderzocht in dunne films van yttrium-aluminium-oxides (Y<sub>2</sub>O<sub>3</sub>-Al<sub>2</sub>O<sub>3</sub>). Als emitterend element werd vanwege de geschikte eigenschappen de lanthanide neodymium (Nd) gebruikt. Er moet voldoende energieoverdracht plaatsvinden opdat Cr de geabsorbeerde lichtenergie kan overdragen naar Nd om het vervolgens te kunnen uitstralen.

Het 3° onderzoek (**Hoofdstuk 5**) richtte zich op de energieoverdracht van een sterk absorberend gastrooster naar een lanthanide. Hiervoor werden dunne films van koper gallium sulfide (CuGaS<sub>2</sub>) met de lanthanide Ytterbium (Yb) onderzocht.

#### Ondervindingen en bevindingen

**Hoofdstuk 6** geeft afsluitend een samenvatting van de ondervindingen bij de drie onderzoeken. Om te kunnen vaststellen welk materiaal voor LSC-toepassingen het meest geschikt is wordt een onderlinge vergelijking gemaakt tussen de materialen die bij de 3 onderzoeken zijn bestudeerd. Er worden hier ook suggesties gedaan voor het verbeteren van de XY-scanning methodologie om zo mogelijk verbeterde LSCs te kunnen maken.

# Acknowledgements

"You can call me anything you want, but don't you ever, ever call me: a self-made man" – Arnold Schwarzenegger.

I'd like to take this opportunity to express my sincere gratitude to everyone who supported me in completing this thesis, and to those who made my time at TU Delft all the more enjoyable.

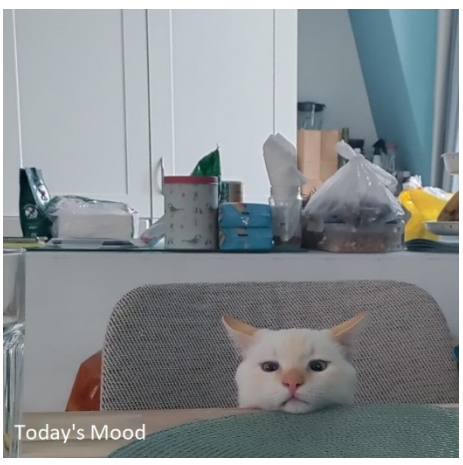
First of all is the man who acquired funding for my project, took me on and supported me from day one: Erik. From the stories I hear of other PhD candidates I can safely say that I lucked out with having you as a supervisor. I felt I could come to you about anything, whether work related or personal, no matter how small. Your office door was always open and you always made time for me. I never felt any stress or pressure from you (though perhaps a little pressure would have done me good). I believe we shared a lot in common, from our backgrounds in astronomy to a love for travel and a shared enthusiasm for taking on renovation projects. I wish you all the best with your future PhD's and your continued research in luminescent thin films.

Then I would like to thank the living luminescence legend himself, Pieter Dorenbos. Despite your countless publications and impactful work, you remain humble and thoughtful to young aspiring scientists. Your presentations always left me feeling that even my simple mind could grasp complex ideas. Enjoy that well deserved retirement!

Behind every great experimentalist, is an even better technician. For the luminescent materials group at TU Delft that man is Johan de Haas. I like to refer to Johan as my work dad. Whenever something broke or I couldn't figure something out he would come in and fix it or show me. The dad similarities don't end there though, as he also helped me in picking gifts for my girlfriend (now fiancé) and plotting a route in the tulip fields to propose to her. He supported me in the RID table tennis final which I proudly won for our group. My cat Apollo is also grateful for the help Johan has given me in building an automatic feeder, despite the fact that Johan has wished harm on him.

Now to the person I have spent most of my time with during my PhD, my desk neighbor Casper. To be honest, I initially thought we wouldn't get along. I could sense a potential Maarten-Evert situation brewing, one that might lead to lingering resentment between us. To my relief this couldn't be further from the truth. You were open to my endless distractions of movie references, meme-stock updates and games of Go. You've educated me in Dutch pop culture references that I missed out on during my upbringing. More importantly, I owe pretty much everything I know about luminescence to you. You truly made my trepidation evaporate and allowed my confidence to grow. One day I'll look down from the moon and I'll still think of you.

Changing the C to a J gives us Jasper. Fun-fact, their birthdays also differ by one day. To quote a former student: "Jasper is also a person". It's true, he is. Maybe one of the most thoughtful persons I have met. One day, at show-and-tell, I brought in my treasured vintage Pokémon card collection and came to the realization that my Electrode card was in Dutch instead of English. Jasper remembered this and officially completed my base set Pokemon cards by gifting me the English Electrode. What's more is that he contributed to organizing some much needed social events at the RID. Lastly, the memes you made of Apollo are simply the best. Below the first ever and my favorite.



Keeping the J and changing 'asper' to 'ustin' brings us to Chun-Ting. A fellow investor who regularly visited my side of the hallway just for a gezellige chat. Thanks for bringing some serenity to the office by incorporating after lunch tea sessions. I truly appreciate your generosity with bringing back snacks from where-ever you went. I also feel reassured knowing that the experimental set-ups are protected by Taiwanese snacks. You brought a sense of calm to the lab, and I hope you find that same calm within yourself. Good luck with finishing your own PhD thesis, I know you will succeed.

Finishing off the J's we have Jeffrey. Starting off as my intern from Utrecht and quickly becoming a force to be reckoned with. I hope to one day have the same level of passion for my work as you do with science. Although your enthusiasm for science can be overwhelming, it is something left to be desired by many PhD candidates. You stayed at my apartment and looked after Apollo, and for that I will forever be grateful.

One final office buddy I would like to thank is Francesco. Your infectious positive attitude brought nothing but joy to the office.

I would like to take a moment to express my gratitude to a somewhat hidden figure: Trudy. I never understood anything administration related and you somehow miraculously managed to make sure I could order all the necessary things I needed to conduct my experiments. Thank you immensely for making that part easier.

During my time I have also seen people leave. Starting with the Russian post-doc who started on the same day as I: Vasya. Even though I spent less than half my time at the TU Delft with you, it feels like I have heard your voice the most. This is partly due to our common commute between Schiedam and Delft, but also because of your high density of words spoken. You taught me a lot about the academic world and helped me integrate, thank you.

Then we have Evert, the golden child. Thanks for leaving your unfillable shoes behind in the lab. PhD with cum-laude? How am I supposed to follow that? Regardless of your over performance, you remained humble and showed me the ropes of doing thin film research. I had a great, albeit, short time in Boston with you in my first week starting at TU Delft. Your programming skills not only made my life easier to do research, it also inspired me to start playing with electronics, one of my favorite hobbies today.

Next up: Giacomo. You have the honor to be a co-author on my first paper, or should I perhaps say that I have that honor. You are one of the kindest persons I know, something the world could use a little more of sometimes. Thank you for taking Apollo into your home for multiple weeks, especially when he was at his peak of being a mischievous teenage cat. I feel like I can message you anytime and I hope you feel the same. All the best with being a dad!

One final person who has left from the group during my time is Maarten. Even though he deliberately left me out of his acknowledgements and mentioned it was a pleasure to share the office specifically with Jasper and Casper, I'd still like to thank Maarten for that one time he gave me a protein bar when I forgot my lunch.

Then we have colleagues outside the group. First off David. Het spijt me dat we altijd Engels met jou spraken, terwijl je juist Nederlands probeert te leren. Bedankt voor alle chocola die je me aanbood, het was ieder keer een aangename verassing! Jack, though our Max-Jack time was limited, I still cherish our disagreements on meme-stocks and NFTs. Don't forget to sell SMCI if you haven't already (NFA). And Marc, you seem like a chill dude, hope you get yourself a cat one day!

A couple more technicians that I would like to mention are Robert and Astrid. Thank you for showing me all things XRD and EDS.

Another group of people that deserve praise are the security at TU Delft. Thank you for letting in various friends so that they can come to the bar in the basement. I love the fact that some of the security guards refer to me as Mario after I, one time, dressed up as the videogame character.

I'd also like to give a shout-out to the PhD council of the RID. I'll always remember the council for embodying the wonderfully awkward charm of scientists.

The last group of colleagues that need no introduction is the bar committee. Specifically, Henk, Koos, Tom, Robin and Rogier. Thank you for always opening the doors on Friday's. I tried my best to get as many people in week in week out. Friday drinks at T' Koepeltje were what I looked forward to on a weekly basis. I hope to give it a proper send off on the day of my defense.

Now come the master and bachelor students. The students doing their final project with us in the group had an enormous impact on the overall vibe. I have been extremely lucky with the students I got the pleasure to supervise. They were all a joy to work together with. I would like to first and foremost shine the spotlight on my first master student, Bauke. Without whom Chapter 2 of this thesis would not be possible. Thank you for making my life easier with your savvy programming skills. I also really enjoyed the times we played squash together, a shame your table tennis skills weren't as good. Second, Timo, congrats to us for publishing a paper! Speaking of publishing papers, Olivia and Sem, thanks for your contribution to our paper together. Lastly, Pepijn, you were my first and I'll never forget that. Then there are the students I interacted with, but didn't supervise. Thank you Mink for providing a much needed comic relief. The Spengler marketing team would be proud of us. Benjamin, thank you for being a worthy challenger on the table tennis table. Your ability to return my smashes triggered an unmatched surge of endorphins as I unleashed smash after smash in rapid succession. In order to not accidentally forget writing someone's name, I will just say thank you to all other remaining students.

That's it for the colleagues and students. Queue in the friends and family. First, I would like to thank my hockey teammates in Trim 5 at Hockey Club Wateringse Veld (HCWV). Hockey has been a great way for me to take my mind off of research. Second, I would like to thank all the friends I have made, wherever I was living at the time. Like my friend Nima, who I went to high school with whilst living in the US. Or Mark, Dimitri, Abe and Andy who I know from my time at the European school in Bergen. Or Oliver, my flatmate from my university studies in Glasgow. Camille, who I met during an exchange year in Miami. Fleur, who I met while travelling in New Zealand. Friends from my hometown in Den Helder like IJbe & Ilse, or Lotte. Although we don't speak every day, these friends shaped me into who I am today. And even though they are spread all over the world, I cherish the memories I have with them. All my friends, at one point or another, have shown interest in my research and have asked how progress on my thesis is going. Thank you all.

Of course, it goes without saying that I am eternally grateful for my parents, Maria & Peter. Thank you for supporting me throughout the years both financially and emotionally. To my brothers, Frank, Bas and Joris, y'all definitely put a number on me during childhood, but I couldn't imagine growing up any other way. Special shout-out to Bas for helping with my thesis cover. Thanks to your better halves, Lilla, Renske and Eline for also showing an interest in my progress during the PhD. A big thank you goes to my aunt Liesbeth, she handcrafted the leather bag I brought to work every day along with my amazing custom shoes. To my newest housemate, Uncle Frank, thank you for welcoming myself, Dimitra and Apollo to your home. Even greater thanks for proof-reading my Dutch in the samenvatting section. I would also like to thank my cousin

Olaf for coming into work one day and selling me some of his Team Rocket Pokémon card collection, by the time this is published I will have completed the set.

A big thank you to my doctoral committee. Especially the third chapter of this thesis benefited immensely from the feedback I received. If the Path-of-Least-Resistant PhD candidates are the unnoticed gears in a machine, then you are the operators steering society to new prosperous heights. I deeply admire your unwavering commitment to science and sincerely hope you view this thesis as a meaningful contribution to the field.

The final two acknowledgements I would like to give are to the two I share an apartment with every day. Apollo, you came into my life roughly 2 years ago and it hasn't been the same ever since. It could be said that without your constant distractions this thesis could have been completed sooner. Nevertheless you are the best cat a man can ask for. And finally, to my fiancé, Dimitra. Your unwavering support throughout my thesis journey is nothing short of amazing. Thank you for standing by me through challenges and celebrating the achievements. I can't wait to marry you in 2025 on Zakynthos.

# **About the Author**

Max Derksen was born on April 29, 1994, in Den Helder, the youngest of four brothers. His mother, Maria Derksen, is a primary school teacher, and his father, Peter Derksen, served as a naval officer. Throughout his childhood, Max's family relocated to the United States twice—first from 1996 to 2000 and again from 2005 to 2009. These moves led him to attend several different schools during his formative years.

In 2009, he earned his General Certificate of Secondary Education (GCSE) from the British School of Washington D.C., and in 2011, he completed his European Baccalaureate (EB) at the European School of Bergen, The Netherlands. Before starting university, Max spent three months traveling and volunteering in Central America, funding his journey with savings from a local cinema job in Den Helder.

In 2017, Max graduated from the University of Glasgow with an integrated master's degree (MSci) in Physics with Astrophysics. Between 2017 and 2020, he worked a variety of jobs to support his travels across Europe and New Zealand. These roles included bartender, factory worker on a food production line, university tutor, software tester, and traffic controller on a ferry.

By the end of 2019, Max felt a growing desire to return to science, leading him to pursue a PhD with the Luminescent Materials Group in the Radiation Science and Technology Department at TU Delft. The past four, nearly five, years of his academic journey are detailed in this thesis.

# 'List' of Publications

As the wise saying goes: quality over quantity.

- Derksen, M., Bosco, G., Muller, T. and van der Kolk, E., 2024. Photoluminescence of combinatorically sputtered Al<sub>2</sub>O<sub>3</sub>–Y<sub>2</sub>O<sub>3</sub> thin films with a Cr<sup>3+</sup> and Nd<sup>3+</sup> co-doping concentration gradient. *Journal of Luminescence*, 269, p.120503.
- 2. **Derksen, M.**, Bergkamp, S., Kohnstamm, O. and van der Kolk, E., 2024. Time, temperature and concentration resolved Yb<sup>3+</sup> luminescence study in cosputtered Cu<sub>2-x</sub>Ga<sub>x</sub>S<sub>2</sub> (0.1< x< 1.6) thin films with a Cu-Ga composition gradient. *Optical Materials*, p.116220.

